Challenge Journal of STRUCTURAL MECHANICS

Vol.2 No.3 (2016)

ISSN 2149-8024

TULPAR ACADEMIC PUBLISHING

Challenge Journal of Structural Mechanics

E-mail: *cjsmec@challengejournal.com*

Web page: *cjsmec.challengejournal.com*

TULPAR Academic Publishing
www.tulparpublishing.com

Challenge Journal of Structural Mechanics

CONTENTS

TULPAR ACADEMIC PUBLISHING

Challenge Journal of Structural Mechanics

Assessment of bonding defects in FRP reinforced structures via ultrasonic technique

Emma La Malfa Ribolla, Mohsen Rezaee Hajidehi, Giuseppe Fileccia Scimemi, Antonino Spada, Giuseppe Giambanco *

Department of Civil, Environmental, Aerospace, Materials Engineering, University of Palermo, 90128 Palermo, Italy

ABSTRACT

Fiber reinforced polymer (FRP) composite systems are widely used for the rehabilitation of concrete structures such as building that need to resist to seismic loads, bridges that have to carry heavier traffic loads. The technique consists in bonding the composite plate to the concrete surface element in order to increase the flexural capacity. A proper attachment of the FRP plate to the concrete surface is necessary for the efficiency of the load transfer between the reinforcement and the substrate. In this work, the quality of composite bonding is characterized through ultrasonic testing. The proposed technique is relative to a time domain analysis of the ultrasonic signals and couples the Akaike Information Criterion (AIC), used as automatic onset signal detection, and the Equivalent Time-Length (ETL), used as an indicator of the quantity of energy propagating through the bonding. It has been tested both numerically and experimentally, in vitro, using samples with imposed well- known defects.

ARTICLE INFO

Article history:
Received 4 July 2016
Accepted 26 August 2016

Keywords:
FRP
Bonding
Nondestructive testing
Ultrasonic waves

1. Introduction

Over the past decades, fiber reinforced polymer (FRP) composite systems have been used for the retrofit of concrete structures. The most common FRP rehabilitation system consists of laminates of carbon- or glass- reinforced polymers (CFRP or GFRP), bonded to the surface of the concrete by means of epoxy adhesive. This technology offers exclusive advantages with respect to the traditional strengthening techniques, e.g. immunity to corrosion, low weight and excellent mechanical properties. The efficiency of a FRP rehabilitation system is highly influenced by its integrity. In particular, the quality of the FRP-concrete interfacial bonding is a critical parameter affecting the structural performance and life expectancy of retrofitted structures since it governs the stress transfer from the concrete to the FRP composite. During the installation of the composite system, improper cure can cause voids, inclusions, debonds and delaminations at the FRP-substrate level. The effects of the common defects are discussed by Kaiser and Karbhari (2003). In addition to this aspect, one of the main problem related to the use of FRP strengthening is the detachment phenomenon, which consists in the sudden and brittle decohesion of the FRP reinforcement from the quasi-brittle support element (Toti et al., 2013; Cottone and Giambanco, 2009).

To evaluate the FRP-substrate defects, non-destructive techniques (NDT) can be used. For this specific application, diversified NDT methods have been advanced and an extensive literature review was carried out by Dong and Ansari (2011) and Kaiser and Karbhari (2004a; 2004b). Infrared thermography has been used to monitor FRP strengthened reinforced concrete bridge columns (Jackson et al., 2000), bridge decks (Halabe et al., 2007), and reinforced concrete beams (Shih et al., 2003). Microwave testing has been used to identify artificially induced disbonds and delaminations within the FRP and at the FRP-to-concrete interface (Akuthota et el., 2004), and delaminations in concrete beams fabricated and strengthened with CFRP (Ekenel et al., 2004). Mirmiran et al. (1999) investigated the applicability of acoustic emission (AE) technology to inspect hybrid CFRP tubes filled with concrete and to correlate

* *Corresponding author*. Tel.: +39-091-23896742 ; Fax: +39-091-427121 ; E-mail address: giuseppe.giambanco@unipa.it (G. Giambanco)
ISSN: 2149-8024 / DOI: http://dx.doi.org/10.20528/cjsmec.2016.08.018

the acoustic emission parameters to the state of stress in concrete. Degala et al. (2009) describe an AE approach to monitor the failure mechanism in reinforced concrete slabs retrofitted with CFRP strips.

In accordance with the combined considerations of defect detectability and practicality of use advanced by Kaiser and Karbhari (2004b), ultrasonic tests are still classified as primary methods of choice due to the existing considerable background and wide range of instrumentation.

Many researchers performed experimental studies using ultrasonic waves for the damage detection on composite laminates (Su et al., 2006; Lestari and Qiao, 2005; Kessler et al., 2002; Alleyne and Cawley, 1992). All these studies are based on the propagation of guided ultrasonic waves (GUWs). Different types of guided waves exist depending upon the geometry of the waveguide, for instance in plate-like structures Lamb waves propagate. These waves can travel over a long distance even in materials with a high attenuation ratio. Unfortunately, however, Lamb wave testing is complicated by the existence of at least two dispersive modes at any given frequency.

Even though an extensive research exists in the framework of damage detection on composite laminates by means of GUWs propagation, less information exists about the wave propagation in FRP laminates bonded to roughly inhomogeneous materials, such as concrete. In this case, a high scattering attenuation occurs due to the presence of heterogeneities. The concrete behaves almost like a perfect absorber generating a considerable number of short-spaced echo peaks that make the defect echo not observable. Previous efforts in the ultrasonic evaluation of bonding defects at the FRP-concrete interface are represented by the work of Bastianini et al. (2001), which involves longitudinal waves propagation in CFRP and GFRP composite materials applied to different substrates (concrete, masonry, and polyurethane) and is based on the relative amplitude of the first echo peak. Kundu et al. (1999) used both Lamb wave scanning and longitudinal wave scanning, in particular pulse-echo and tone-burst C-scan. Mahmoud et al. (2010) studied the influence of aging condition of CFRP-concrete specimens on ultrasonic features, i.e. velocity, peak amplitude, average power, maximum power-frequency ratio and frequency at maximum ratio. Mirmiran and Wei (2001) used ultrasonic pulse velocity (UPV) testing to quantify the extent and progression of damage in concrete filled FRP-tubes.

In this paper, an experimental study with the aim of assessing the quality of the FRP-concrete bonding by means of ultrasonic testing is presented. The main novelty of the paper is the introduction of a statistical parameter called Equivalent Time-Length (ETL) to predict the quality of the bonding. The proposed procedure involves also the automatic determination of the onset of the signal which is performed by means of the Akaike Information Criterion (AIC) (Akaike, 1974). To interpret the experimental findings, Finite Element (FE) analysis were performed.

2. ETL for Defect Detection

In the case of perfect bonding between FRP and concrete, the acoustical impedance mismatch between the two media is small. In this case, the sound speed measured in the FRP and the substrate is of the same order of magnitude, therefore the energy of vibration is almost entirely transmitted to the concrete where it is largely absorbed by scattering. On the contrary, when the bond between FRP and concrete is compromised by the presence of a thin air gap, the acoustical mismatch is much bigger and the sound speed in the FRP is about 10 times bigger than the one in the air. In this condition, a higher amount of energy mostly propagates in the direction of the fibers (Fig. 1).

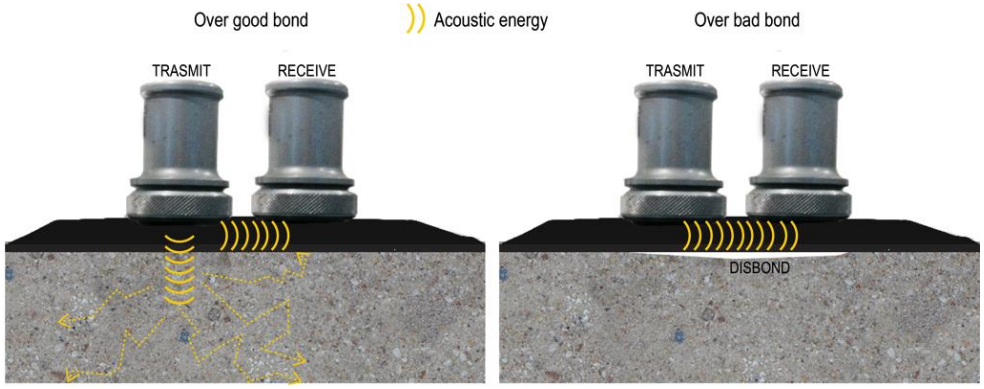

Fig. 1. Bond testing pitch-catch mode.

To quantify the aforementioned energetic phenomenon, the most common practices involve the use of the first echo amplitude (Bastianini et al., 2001), the peak-to-peak or the average amplitude of the signal in a given time window (Kundu et al., 1999). However, by applying a direct-contact technique, the ultrasonic response in terms of pulses amplitude is affected by two main factors, i.e. the thin film of couplant between the probe and the medium and the pressure of the transducers on the sample. Furthermore the presence of fibers strongly affects the ultrasonic response.

The proposed approach considers the onset time of the signal, which is calculated by applying the automatic onset determination algorithm advanced by Akaike

(1974) and used by other researchers (Maeda, 1985; Kurz et al., 2005). The algorithm allows the exact onset determination when signal and noise are in the same frequency range, which often occurs in presence of concrete as a travelling medium (Kurz et al., 2005). According to this approach, , a time series can be divided into locally stationary segments, each modeled as an autoregressive process. A signal including the onset and a first estimate of the onset time is needed. The intervals before and after the onset time are assumed to be two different stationary time series. For a fixed order autoregressive process, the point at which the AIC is minimized determines the separation point of the two time series (noise and signal) and therefore the onset point of the signal, t_{AIC}. The AIC function is obtained through the following expression:

$$AIC[k] = k\,log\left(var\big(A(k,1)\big)\right) + (N-k-1)\,log\left(var\big(A(1+k,N)\big)\right), \quad (1)$$

where the term $A(k,1)$ means that the variance function is only calculated from the current value of k, while $A(1 + k, N)$ means that all samples ranging from $1 + k$ to N are taken. By calculating the minimum of Eq. (1), the onset time t_{AIC} is obtained:

$$AIC(k_{min}) = min\,AIC[k], \quad (2)$$

$$t_{AIC} = k_{min}\Delta t, \quad (3)$$

being Δt the time interval between two sample points.

Successively, the following wave feature, named Equivalent Time Length (ETL) is calculated as:

$$ETL = \sqrt{\frac{\Sigma_{k=AIC+1}^{N} A(t_k)^2 (t_k - t_{AIC})^2}{\Sigma_{k=AIC+1}^{N} A(t_k)^2}} \quad k = [1,2,\dots,N], \quad (4)$$

where N is the number of point samples, $A(t_k)$ is the amplitude of the signal at the time t_k. It should be mentioned that a similar parameter is adopted in the framework of time-domain measurements of partial discharge pulse (Contin et al., 2002). The difference with respect to the present study is that in Eq. (4) t_{AIC} is named t_0 and is defined as the time-barycenter of the energy of the signal. In the framework of partial discharge pulses, the ETL, together with the equivalent bandwidth, provide an intuitive and compact representation of the detected signals. From Eq. (4), it is noted that the ETL returns the time associated to the sum of the products of the instantaneous energies and their respective square occurring time, with respect to the onset of the signal.

3. Ultrasonic Test

3.1. Numerical setup

A two dimensional FEM model was developed to simulate the ultrasonic wave propagation within a composite laminate partially or fully bonded to a concrete sample. The numerical setup follows the work of Ghose et al. (2011) where ultrasonic guided wave propagation is simulated in a multi-layered composite structure. The model is presented in Fig. 2(a) and consists of a 150×250 mm concrete sample cross-section covered with a layer of CFRP, 1.4 mm thick. The FRP-concrete interface was modeled according to four different conditions. The ND0 model corresponds to the fully bonded condition, where the nodes in pair on the same interface are rigidly linked together. In the ND1, ND2, ND3 models, the bonding defects are introduced demerging the interfacial nodes. 4517 triangular elements were used to mesh the domain of the CFRP and concrete (Fig. 2(b)). The material properties of the CFRP and concrete materials used in the model are mentioned in Table 1. The properties of the CFRP were defined considering the material as orthotropic with unidirectional fibers laid along the x-direction and the rule of mixtures (Voigt, 1889; Reuss, 1929).

Table 1. Material properties of FRP and concrete.

Parameters	Young's modulus [GPa]	Density [kgm^{-3}]	Poisson's ratio
CFRP	E_{11}=200 E_{22}= E_{33}=12	1065	ν_{12}= ν_{13}=0.31 ν_{23}=0.45
Concrete	E=25	2300	ν=0.33

The excitation signal was chosen by considering five cycles of sine function at 500 kHz generated by the pulser-receiver and transmitted/received by means of the ultrasonic probes placed in contact with each others. This expedient was chosen to better simulate the experimental excitation input given to the structure. The disturbance was applied to a 2.5 mm long line of the CFRP boundary to simulate the excitation transmitted by the probe on the sample with displacement along the z-direction. To model the two dimensional geometry the case of plain strain was considered. Time dependent analysis, Lagrange quadratic type of element were used for the solution. The duration of time span for the solution was chosen to be 160 μs in such a way that the complete signal was captured at the point of observation, which is the midspan of the output line in Fig. 2(a). The time step chosen in the model was 0.01 μs.

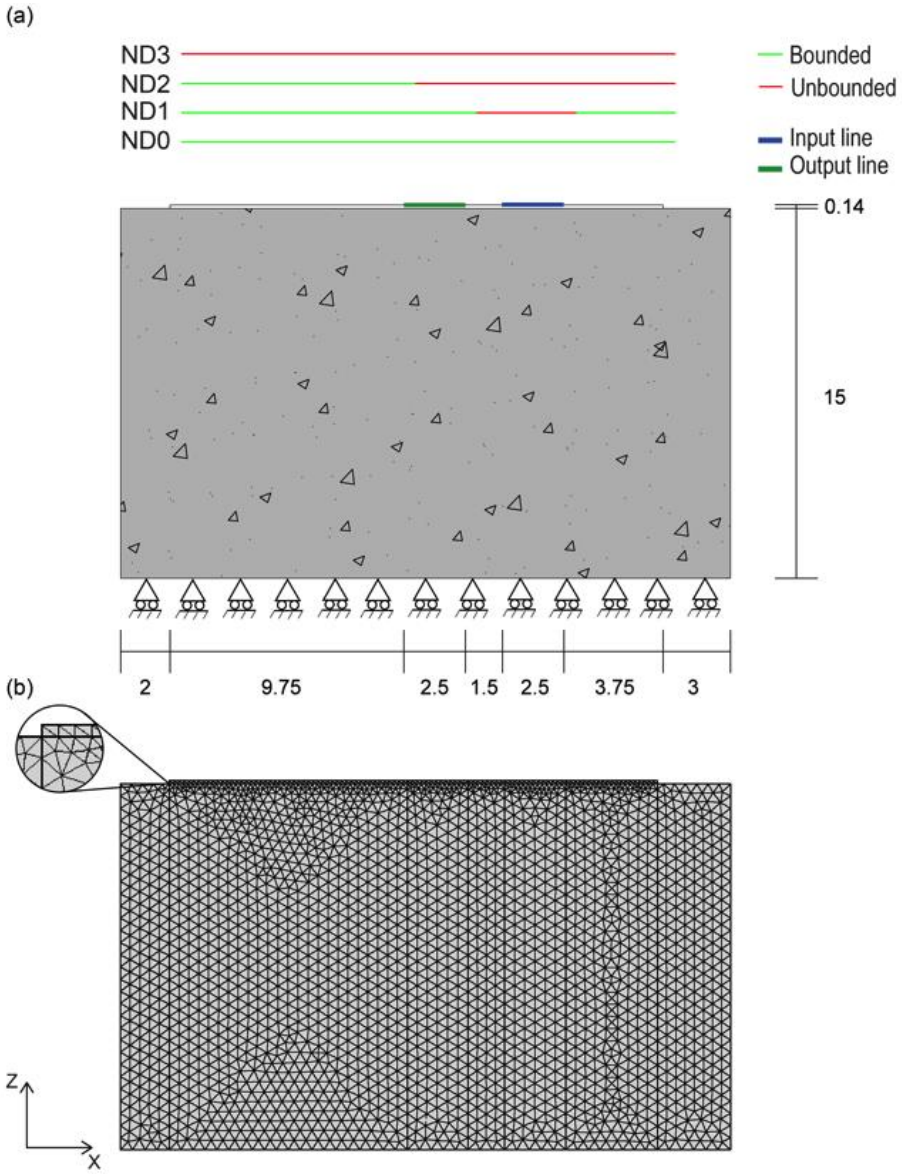

Fig. 2. Numerical simulation setup: (a) Scheme; (b) Mesh of the model.
(*Geometrical dimensions are expressed in centimeters.*)

3.2. FRP-concrete samples preparation

Four concrete prisms with dimensions of 180×250×150 mm were prepared using Type I Portland Cement, water, river sand and #67 limestone coarse aggregate as substrates. The average 28-days standard cubic strength was 30 MPa. The concrete was sandblasted to achieve a surface profile of #4, according to the International Concrete Repair Institute (Guideline 310.1R-2008, 2009). Bonding the FRP was executed in accordance with the manufacturer's application guideline using commercial epoxy resin. In order to simulate the lack of bonding of the FRP, three types of defects of known dimensions were imposed on three of the four samples using the interposition of different foils of Teflon between the concrete surface and the adhesive layer. The four samples were named from D0 (absence of defect, i.e. pristine state) to D3 (large defect), according to the size of the included Teflon foil. Fig. 3 shows the top view of the concrete samples at the time of the position of the defects. After mixing the two-component adhesive, this was applied using a paint brush. While the epoxy resin was still wet, dry uniaxial fabric was placed onto the substrate and pressed by means of hand pressure in the fiber direction. A second layer of epoxy was applied using a paint brush, rolling from the middle of the sheet to push out all air bubbles, ensuring that the fabric was completely saturated. The FRP was allowed to cure for 7 days at 23°C.

3.3. Experimental setup

The setup shown in Fig. 4 was employed for the ultrasonic testing in the FRP- concrete samples. A house-built pulser-receiver was used for generating and acquiring the ultrasonic waves. In this test, five cycles of sine wave with frequency 600 kHz, were generated and employed as incident wave. Two ultrasonic transducers with frequency of 1 and 0.5 MHz (P25 Piezo, IMG

Ultrasuoni s.r.l.) were used in a pitch-catch mode as a transmitter and receiver transducer, respectively. The diameter of the transducer's contact surface was 25 mm. The transducers were placed perpendicularly to the plane of the FRP reinforcement to produce a normal-type ultrasonic wave. As conducting medium, coupling gel was placed between the transducers and the specimen. The received signals were amplified and filtered by an ultrasonic preamplifier (Olympus NDT Inc., Waltham, MA, USA). The acquisition process was controlled by a house-built software Pulser 2.00. In order to obtain a more accurate time waveforms classical assumption of noise equal to zero is used, hence 50 waveforms were registered at each measurement and the mean-value of these acquisitions was used as a reference waveform.

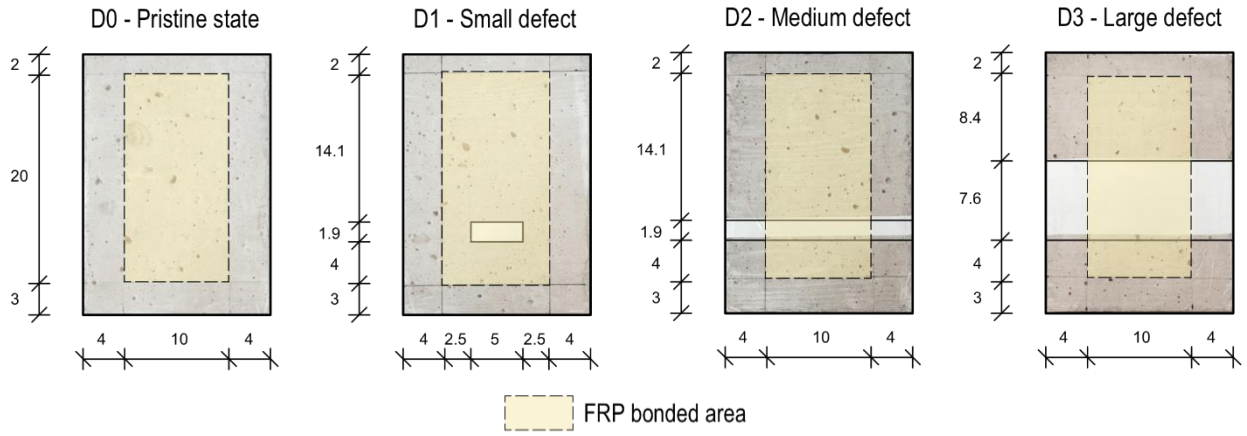

Fig. 3. Concrete samples with the Teflon foils at the time of the FRP reinforcement laying.
(*Geometrical dimensions are expressed in centimeters.*)

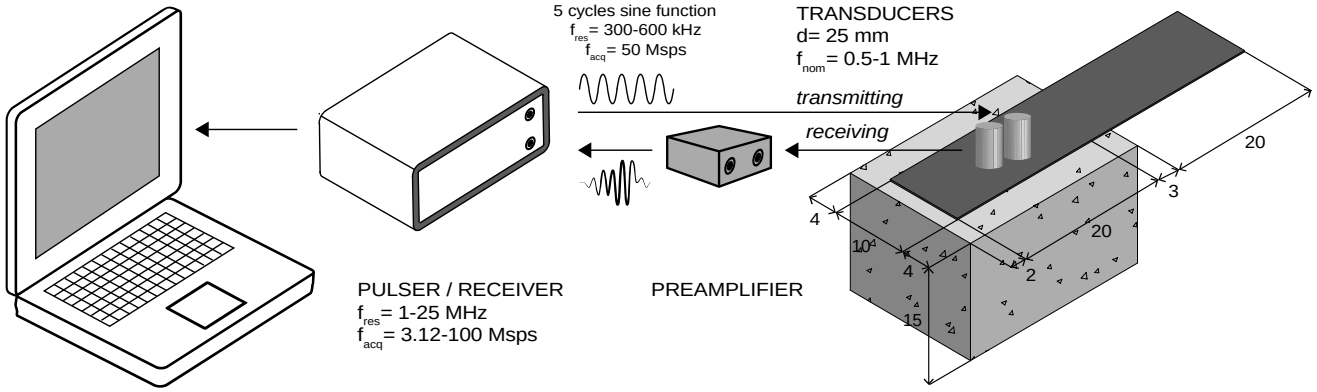

Fig. 4. Schematic configuration for the FRP-concrete ultrasonic test setup.
(*Geometrical dimensions are expressed in centimeters.*)

4. Results and Discussion

In this section, both the numerical and the experimental results are presented.

Fig. 5 shows the vertical displacement map at two different instant, equal to 6.68 μs and 15.04 μs. The two sub-figures are relative to ND0 model while the bottom two sub-figures are relative to the ND3 model. For the sake of shortness, only the two extreme cases are reported. The displacement maps perfectly replicate the physical phenomenon schematized in Fig. 1. In the case of perfect bonding, the waves propagates through the bulk material, conversely in the case of interfacial mismatch the waves propagates through the FRP thickness, being in this way assimilated to surface or guided waves. It should be noted that the media are numerically homogeneous, hence the scattering and the damping caused by the heterogeneities of concrete is not numerically quantifiable. In the real case, it would therefore be necessary to quantify the amount of acoustic energy which penetrate in the bulk material and the amount that is reflected at the FRP-concrete interface. Nevertheless, this requirement may be time-expensive and inconvenient.

To see how the whole energy reflection could be characterized, we present in Figs. 6(a) and (b) the waterfall chart containing the numerical and experimental waves profiles, respectively, measured at each different defect size and relative to the time interval 0 – 40 μs. The values were normalized with respect to the maximum value since the numerical pulse describes a displacement, while the experimental pulse refers to a voltage. The amplitude and the arrival of the signal change slightly, whereas the energy distribution is visibly shifted by the increase of the defect size. The variations observed were

quantified by extracting the ETL from the time series. Together with the ETL, the Root Mean Square Deviation (RMSD) and the maximum amplitude (A_{max}) were calculated. Their numerical and experimental trends are presented in Figs. 6(c) and 6(d). The values were normalized with respect to the case of worst bonding. The latter is represented by the ND3 model for the numerical case, while, for the experimental case, this is represented by a single laminate of FRP, considered free, i.e. unbounded to concrete.

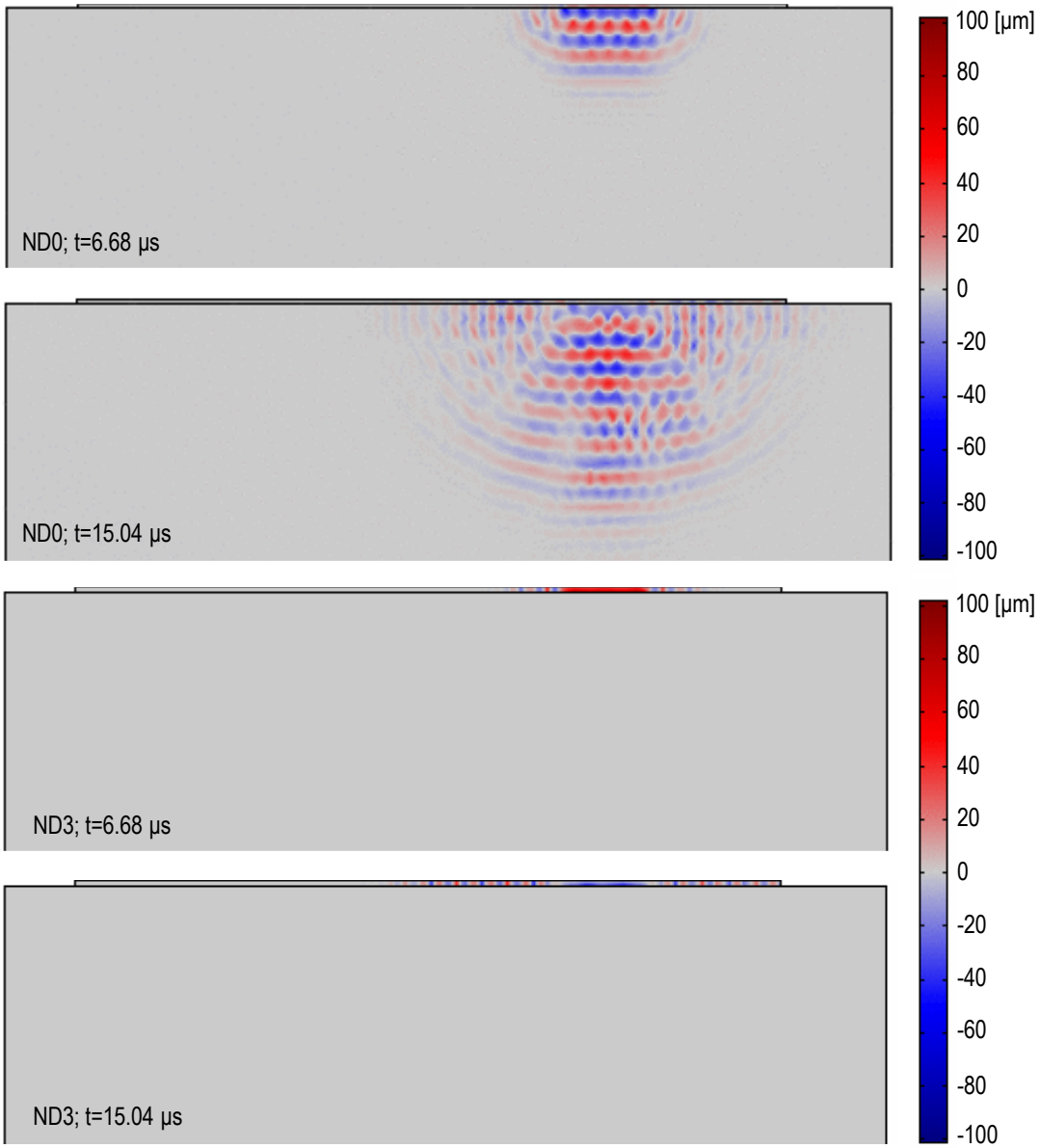

Fig. 5. Numerical results: displacement field, vertical component, relative to ND0 and ND3 model at the time 6.68 μs and 15.04 μs.

The results show that the statistical parameters ETL and RMSD behave monotonically. Both numerically and experimentally, the ETL is increasing with similar variation, suggesting the quantity of acoustic energy that passes through the bonding. A decreasing trend is instead observed for the RMSD, which depends on the choice of the baseline signal, that is the case of pristine state. Lastly, the maximum amplitude does not seem to have the same reliability to predict the quality of bonding. Specifically, in the case of direct active ND measurement the amplitude could be affected by external factors discussed in Section 2.

The theory of acoustic propagation in materials shows that the parameters of the backscattered ultrasonic signal depend on the ultrasonic signal frequency, reason why the ETL was in this paper calculated by considering actuation frequencies in the range 200-600 kHz (Fig. 7). It was found that frequencies lower than 400 kHz are not reliable for the application developed, as visible from the linear trends associated to the ETL with not justifiable attitudes. It is however well known that lower frequencies are associated to wider wavelengths, which can be over-size with respect to the defect dimensions.

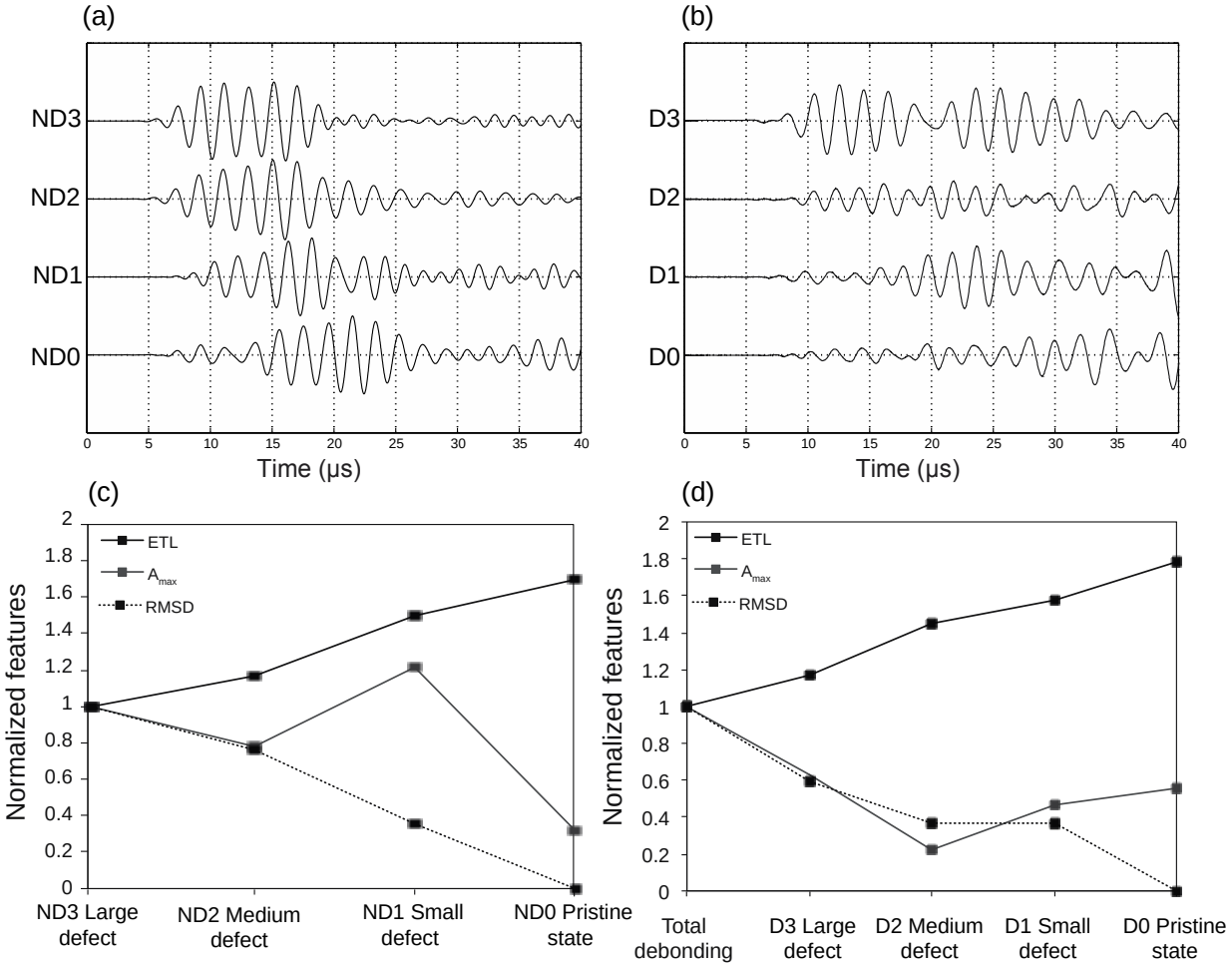

Fig. 6. FRP-concrete interface defect detection results:
(a) *z*-direction displacement profiles measured in the midspan of the output line of the numerical models;
(b) *A*-scan experimental waves profiles;
(c) ETL, Maximum amplitude, RMSD calculated for the numerical;
(d) Experimental waves profiles. The values presented were normalized to the worst case of bonding.

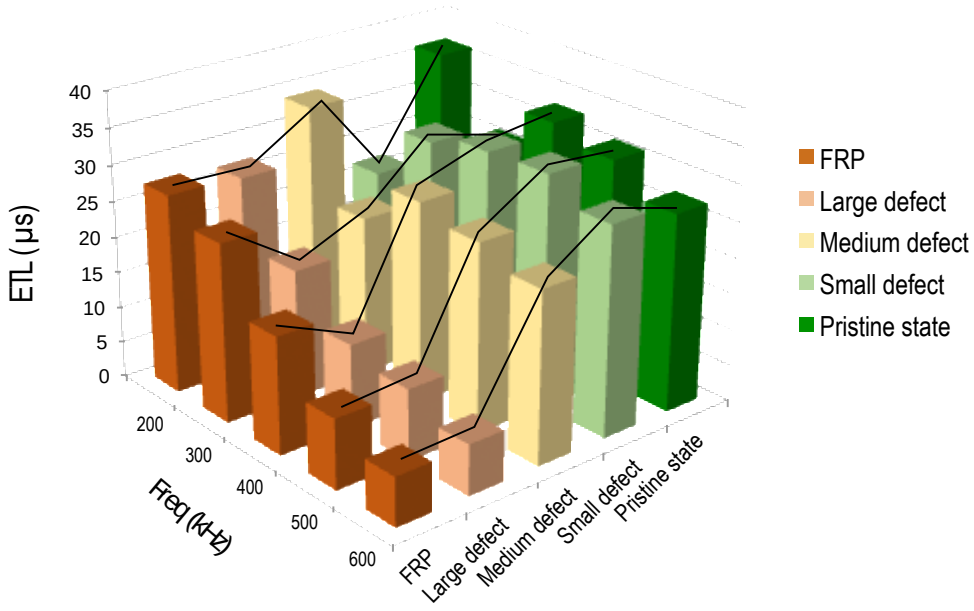

Fig. 7. FRP-concrete interface defect detection results:
ETL as a function of the quality of bonding considering different input frequencies.

5. Conclusions

The integrity and the reliability of bonds are critical to the quality of FRP reinforcement in concrete structures. In this paper a pitch-catch energetic method is used as inspector method of bonding condition. As a common pitch-catch investigation, the method employs two probes, one transmitting a burst of acoustic energy into the test part and another one catching the sound propagating across the test piece. The bond condition is usually determined by considering the difference in the amplitude and/or phase between good and bad bonds. In this paper we introduce the Equivalent Time Length (ETL) as an energy distribution indicator sensitive to the quality of bonding. The inspection should be done at a fixed frequency and considering a certain time-window. Generally we observed that a bonded condition correspond to higher values of ETL since the acoustic energy is transmitted through the concrete. A disbond condition, conversely, results in lower values of ETL since the waves travel between the transmitting and receiving transducer.

We conducted a numerical analysis and laboratory experiments aimed at validating the above research hypotheses. A 2D finite element model of a FRP laminate bonded to a concrete sample was created. Different bonding conditions were modeled by decoupling the FRP-concrete interfacial nodes. Experimentally, FRP laminate with a specific bonding defects were placed into four concrete samples. The results demonstrated that the ETL increase with increasing bonding quality. The experimental results were also interpreted by comparing them to the numerical ones. We found that most of the experimental and numerical results are in good agreement each other.

References

Akaike H (1974). Markovian representation of stochastic processes and its application to the analysis of autoregressive moving average processes. *Annals of the Institute of Statistical Mathematics*, 26(1), 363-387.

Akuthota B, Hughes D, Zoughi R, Myers J, Nanni A (2004). Near-field microwave detection of disbond in carbon fiber reinforced polymer composites used for strengthening cement-based structures and disbond repair verification. *Journal of Materials in Civil Engineering*, 16(6), 540-546.

Alleyne DN, Cawley P (1992). The interaction of Lamb waves with defects. *IEEE Transactions on Ultrasonics, Ferroelectrics and Frequency Control*, 39(3), 381-397.

Bastianini F, Di Tommaso A, Pascale G (2001). Ultrasonic non-destructive assessment of bonding defects in composite structural strengthenings. *Composite Structures*, 53(4), 463-467.

Contin A, Cavallini A, Montanari GC, Pasini G, Puletti F (2002). Digital detection and fuzzy classification of partial discharge signals. *IEEE Transaction on Dielectrics and Electrical Insulation*, 9(3), 335-348.

Cottone A, Giambanco G (2009). Minimum bond length and size effects in FRP-substrate bonded joints. *Engineering Fracture Mechanics*, 76, 1957-1976.

Degala S, Rizzo P, Ramanathan K, Harries KA (2009). Acoustic emission monitoring of CFRP reinforced concrete slabs. *Construction and Building Materials*, 23(5), 2016-2026.

Dong Y, Ansari F (2011). Non-destructive testing and evaluation (NDT/NDE) of civil structures rehabilitated using fiber reinforced polymer (FRP) composites. *Service Life Estimation and Extension of Civil Engineering Structures*, 193-222.

Ekenel M, Stephan V, Myers JJ, Zoughi R (2004). Microwave NDE of reinforced concrete beams strengthened with CFRP laminates containing surface defects and tested under cyclic loading. *16th World Conference on Nondestructive Testing*, Montreal, Canada, August-September, 2004.

Ghose B, Balasubramaniam K, Krishnamurthy CV, Rao AS (2011). Comsol based 2D FEM model for ultrasonic guided wave propagation in symmetrically delaminated unidirectional multi-layered composite structures. *Proceedings of the National Seminar & Exhibition on Non-Destructive Evaluation.* December 8-10, 2011.

Guideline 30.1R-2008 (2009). Guide for Surface Preparation for the Repair of Deteriorated Concrete Resulting from Reinforcing Steel Corrosion.

Halabe UB, Vasudevan A, Klinkhachorn P, GangaRao HV (2007). Detection of subsurface defects in fiber reinforced polymer composite bridge decks using digital infrared thermography. *Nondestructive Testing and Evaluation*, 22(2-3), 155-175.

Jackson D, Islam M, Alampalli S (2000). Feasibility of evaluating the performance of fiber reinforced plastic (FRP) wrapped reinforced concrete columns using ground penetrating RADAR (GPR) and infrared (IR) thermography techniques. *Structural Materials Technology IV-An NDT Conference*, 390-395.

Kaiser H, Karbhari VM (2003). Identification of potential defects in the rehabilitation of concrete structures with FRP composites. *International Journal of Materials and Product Technology*, 19(6), 498-520.

Kaiser H, Karbhari VM (2004a). Non-destructive testing techniques for FRP rehabilitated concrete. I: a critical review. *International Journal of Materials and Product Technology*, 21(5), 349-384.

Kaiser H, Karbhari VM (2004b). Non-destructive testing techniques for FRP rehabilitated concrete. I: an assessment. *International Journal of Materials and Product Technology*, 21(5), 385-401.

Kessler SS, Spearing SM, Soutis C (2002). Damage detection in composite materials using Lamb wave methods. *Smart Materials and Structures*, 11(2), 269.

Kundu T, Ehsani M, Maslov KI, Guo D (1999). C-scan and L-scan generated images of the concrete/GFRP composite interface. *NDT & E International*, 32(2), 61-69.

Kurz JH, Grosse CU, Reinhardt HW (2005). Strategies for reliable automatic onset time picking of acoustic emissions and ultrasound signals in concrete. *Ultrasonics*, 43(7), 538-546.

Lestari W, Qiao P (2005). Application of wave propagation analysis for damage identification in composite laminated beams. *Journal of Composite Materials*, 39(22), 1967-1984.

Maeda N (1985). A method for reading and checking phase times in auto-processing system of seismic wave data. *Zisin (=Jishin)*, 38(3), 365-379.

Mahmoud AM, Ammar HH, Mukdadi OM, Ray I, Imani FS, Chen A, Davalos JF (2010). Non-destructive ultrasonic evaluation of CFRP-concrete specimens subjected to accelerated aging condition. *NDT & E International*, 43(7), 635-641.

Mirmiran A, Shahawy M, Echary HE (1999). Acoustic emission monitoring of hybrid FRP-concrete columns. *Journal of Engineering Mechanics*, 125(8), 899-905.

Mirmiran A, Wei Y (2001). Damage assessment of FRP-encased concrete using ultrasonic pulse velocity. *Journal of Engineering Mechanics*, 127(2), 126-135.

Reuss A (1929). Berchnung der Fliegrenze von Mischkristallen auf Grund der Plastizittsbedingung fr Einkristalle. *Zeitschrift fr Angewandte Mathematik und Mechanik*, 9(1), 49-58 (in German).

Shih JKC, Tann DB, Hu CW, Delpak R, Andreou E (2003). Remote sensing of air blisters in concrete-FRP bond layer using IR thermography. *International Journal of Materials and Product Technology*, 19(1-2), 174-187.

Su Z, Ye L, Lu Y (2006). Guided Lamb waves for identification of damage in composite structures: A review. *Journal of Sound and Vibration*, 295(3), 753-780.

Toti J, Marfia S, Sacco E (2013). Coupled body-interface nonlocal damage model for FRP detachment. *Computer Methods in Applied Mechanics and Engineering*, 260, 1-23.

Voigt W (1889). Ueber die Beziehung zwischen den beiden Elasticittsconstanten isotroper Krper. *Annalen der Physik*, 274(12), 573-587 (in German).

Challenge Journal of Structural Mechanics

Energy & crack tip stress interactions in mixed mode I/III fracture of DX51 steel sheets

Claire De Marco Muscat-Fenech [a,*], Stephen Ciappara [b]

[a] *Department of Mechanical Engineering, University of Malta, Msida MSD2080, Malta*
[b] *London Offshore Consultants, Ibex House, 42-47 Minories, London EC3N 1DY, United Kingdom*

ABSTRACT

DX51D sheet is subjected to mixed mode I/III loading in a purposely designed fixture apparatus. The resulting stable crack-tip growth, direction, slant angle and typical factory-roof crack were observed and discussed as the loading mixity was varied. The total essential work of fracture or fracture toughness, for each mixity loading, was evaluated adopting energy methods during experimentation, whilst theory details how the total may be separated into its individual mode components. The fracture type and direction of crack path were based on the von Mises failure theory and the fracture criteria of maximum shear stress, maximum hoop stress and maximum normal stress along with the application of Hill's theory. The findings described clearly establish the link between the applications of the energy based equations governing crack initiation and propagation and the equations describing the stress field surrounding the crack tip in the mixed mode I/III field.

ARTICLE INFO

Article history:
Received 25 July 2016
Accepted 6 September 2016

Keywords:
Mixed mode
Failure criteria
Slant fracture
Fracture toughness
Stress intensity

1. Introduction

Structures constructed from ductile materials are often subjected to mixed mode loading conditions in tension (mode I), in-plane shear (mode II) and out-of-plane shear (mode III). Mixed mode I/III fracture in ductile thin sheets is quite involved resulting in a complex 3D stress and strain field around the crack tip.

Initial studies for mixed mode loading and the ensuing fracture failure criterion proposed by Erdogan and Sih (1963) suggested several criteria, the maximum hoop stress criterion (MHSC) - the crack propagates along the plane normal to the maximum hoop stress and that this maximum hoop critical stress is a material property and the maximum energy release rate (or Griffith theory) - the crack propagates in a direction perpendicular to the far field tensile load in a direction such that the crack maximizes its energy release rate and therefore independent of the load mode mixity. Investigators working with materials which fail in a brittle manner who compared such criteria are Suresh et al (1990), Macagno and Knott (1989), Royer (1988) and showed that the crack propagation direction and crack loads differ only slightly when applying the criteria to these brittle materials.

There has been much investigation undertaken on the individual mode and on mixed mode loading. The various criteria proposed by previous investigators are the maximum strain energy density, whereby the crack propagates along the plane with a minimum strain energy density criterion (Sih and Cha, 1974; Sih and Barthelemy, 1980; Chen et al., 1986); the maximum normal stress criterion MNSC, when the crack propagates along the plane normal to the maximum normal stress (Tian et al., 1928), (Yates and Miller, 1989); the maximun principal stress criterion - the crack propagates perpendicular to the maximun principal stress; the maximum strain energy release rate where the crack propagates along a direction which maximizes the energy release rate (Pook and Sharples, 1979; Pook, 1985; Chen et al.,1986; Yates and Miller, 1989). All these investigators note that the crack growth direction and the fracture loads differ only slightly no matter which criteria was applied.

* *Corresponding author*. Tel.: +356-2340-2106 ; Fax: +356-2134-3577 ; E-mail address: claire.demarco@um.edu.mt (C. De Marco Muscat-Fenech)
ISSN: 2149-8024 / DOI: http://dx.doi.org/10.20528/cjsmec.2016.09.019

Nomenclature

a	Crack length [m]
A	Surface area of the crack [m^2]
E	Young's modulus [N/m^2]
K	Stress Intensity Factor [Pa$\sqrt{m}$]
L	Crack length advance, leg length [m]
n	Work hardening exponent
R	Specific essential work of fracture [N/m]
r	Distance from crack tip [m]
t	Thickness [m]
u	Displacement [m]/Length [m]
U	Work done/Energy [J]
w	Width [m]
W	Work done [J]
W_f	Work of fracture [J]
W_b	Work of un/bending [J]
W_T	Work of twisting [J]
$x/y/z$	Coordinates
X	Load, force [N]
α	Direction of crack front [^{o}]
ε	Strain [/]
ϕ	Direction of relative motion [^{o}]
Λ	Elastic strain energy [J]
γ	Mode mixity loading angle for Mode I/III
τ	Shear stress [N/m^2]
θ	Direction of stress [^{o}]
Γ	Plastic strain energy [J]
ξ	Plastic level through sheet thickness [/]
ρ	Distance from crack tip through the thickness [m]
ρ	Radius of curvature [m]
σ	Stress [N/m^2]
σ_y	Yield stress [N/m^2]
σ_o	Strength coefficient [N/m^2]
I	Mode I component
III	Mode III component
I/III	Mixed-mode I/III component
b	Un/bending
c	Critical
t	Total
T	Twist
y	Yield
m/c	Machine
rel	Relative
CT	Compact tension
LEFM	Linear elastic fracture mechanics
MHSC	Maximum hoop stress criterion
MNSC	Maximum normal stress criterion
MSSC	Maximum shear stress criterion
SEN	Single edge notched

Various authors have also studied the mode I/III fracture in brittle materials and concluded that the tensile mode I dominated the Mode I/III loading and the resulting typical fracture surface is non-planar (Sommer, 1969; Knauss, 1970; Chai, 1988; Suresh and Tschegg, 1987; Suresh et al., 1990; Hsia et al., 1995, Chao and Liu, 1997). The fracture surface resulting from this mixed mode loading is quite irregular and the crack initiation angles are not easy to measure (Pook, 1985; Yates and Miller, 1989; and Lui et al., 2004). Crack propagation in ductile materials under mixed mode I/III loading results in a complex 3D stress and strain field, the resulting macroscopic fracture mechanism are highly dependent on the mixity ratio between mode I and mode III and the associated out-of-plane stress system. Work performed by Shah (1974), Williams and Ewing (1972), Feng et al. (1993), Hui and Zehinder (1993), Kamat and Hirth (1994), Kamat and Hirth (1996), Helm et al. (1997), Helm et al. (2001), Sutton et al. (2001) and Lan (2006) all show that the resulting fracture surface is heavily dependent on the material properties and mode mixity competition of mode I versus mode III. This is also to be shown in this investigation.

Transition fracture type in mixed mode I/III in ductile materials have been investigated by Erdogan and Sih (1963), Maccagno and Knott (1992), Chao and Liu (1997), Chao and Zhu (1999), Lui et al. (2004) using only linear elastic fracture mechanics (LEFM) to predict crack loading and crack path direction for both brittle and ductile materials using the material's strength ratio of shear stress to tensile stress, τ_c/σ_c, and that the material's failure is according to the classical Tresca and von Mises failure theories. This approach is also adopted in this investigation since complete solution for the elastic-elastoplastic-plastic case of mode I/III do not yet exist, although partial results have been provided by Pan and Shih (1992) which are at present not sufficient.

The specimen types for the out-of-plane mode I/III investigations have been varied. Sutton et al. (2001) and Lan (2006) use a single edge notch (SEN) plate for in-plane tension-torsion loading, whilst Wei et al (2005), Yan et al. (2007, 2009), Wei (2011), Li et al. (2011) use a CT SEN plate with a short initial starter crack length and analyse their results using FEA. A modification to the CT SEN is one with a longer starter crack, commonly called a two legged trouser tear specimen, which is to be used in this investigation. The longer legs SEN specimen geometry was initially used by Rivlin and Thomas (1953) and successive co-workers for the large deformation and non-linear elastic response of sheet rubber. Work on ductile thin sheet materials has been successful completed by Mai and Cotterell (1984) and Muscat-Fenech et al. (1992, 1992, 1994a, 1994b). The tests on the two leg specimens use the work energy method and determine the essential work of fracture.

The work described here is to combine the work/energy criterion of the essential work of fracture and the crack tip stress/stress intensity approach. Investigators tend to normally solve such mixed mode problems with either method independently. The primary scope of this work is to establish a link and show how, through successful experimental under takings, this connection can

be achieved, whilst introducing some novel approaches to the theoretical and experimental work. Mixed mode I/III testing in ductile sheet materials occur as a complicated affair, with many important fracture events taking place. The investigation is to break down the many aspects involved during this process and report the findings in a systematic approach. The governing equations of crack tip stresses together with traditional theories and fracture criterions predict the type, path direction and slant angle of the advancing crack. Ductile fracture theory, presented as a novel approach, will describe how the mode mixity loading conditions affect the resulting slant angle and fracture type. The work energy approach extends the application of the established two-legged trouser specimen to mixed mode loading and the determination of the essential work of fracture. In addition, a new method based on the geometrical and mode I/III loading conditions, can successfully partition the essential work of fracture into its pure mode values at each loading mixity angle. The testing regime presented here is the first of its kind.

2. Theory

2.1. Mode I/III analysis

The crack tip zone suffers the highest stress concentration for sheet material under mixed mode loading. Westergaard (1939), Irwin (1957), Sneddon (1946) and Williams (1957) were amongst the first to investigate and publish the solutions of the closed form expression for the crack tip stress, assuming anisotropic linear elastic material behaviour. The original Westergaard stress functions solved for limited crack problems and modification, Sih (1966), Eftis and Liebowitz (1972), Sanford (1979) to the theory gives greater applicability of the solutions. Mixed mode fracture problems are reported proposing the maximum hoop stress failure criterion, MHSC (Erdogan and Sih (1963) on brittle materials); the maximum shear stress criterion, MSSC (Maccagno and Knott (1992) on fracture of ductile materials); and the application of MHSC and MSSC to predict the fracture type transition (Chao and Liu, 1997; Chao and Zhu, 1999). Liu et al. (2004) and Chao and Zhu (1999) report that there is only a very small difference between the elastic and elastic-plastic crack tip solutions.

The current investigation describes and analyses the many aspects of this complex mode I/III fracture of thin sheet materials:

- the description of the initial crack tip stresses involved during the loading;
- the fracture type determined from the material's critical tensile and shear stress (applying the Tresca and von Mises failure theories for ductile materials) when compared to the mode I/III stress theoretical predictions, together with the fracture criterions of MSSC, MHSC and the maximum normal stress criterion, MNSC, when the crack propagates along the plane normal to the maximum normal stress;
- the path direction and slant angle of the propagating crack are also determined using the material stress intensity factors in the respective pure mode directions, K_I and K_{III};
- an energy criterion is applied to this analysis along with Hill's (1953) theory of ductile sheet materials;
- the mode I/III essential work of fracture for varying load mixity angle, γ is obtained through experiment;
- geometrical and energy considerations allow the total essential work of fracture, R to be separated into its individual (R_I and R_{III}) percentage contribution of each of the load mixity angle scenarios.

The approach considered here, linking the methods of traditional crack tip stresses and intensity factors to the essential work of fracture is an innovative approach for mode I/III testing.

2.2. Mode I/III crack tip stresses and fracture type determination

Following the same trend as other investigators, Erdogan and Sih (1963), Maccagno and Knott (1992), Chao and Liu (1997), Chao and Zhu (1999) and Liu et al. (2004) to the solution of problems involving mixed mode, the mixed mode I/II/III crack tip stress fields, using cylindrical (r, θ, z) coordinates are shown in Fig. 1.

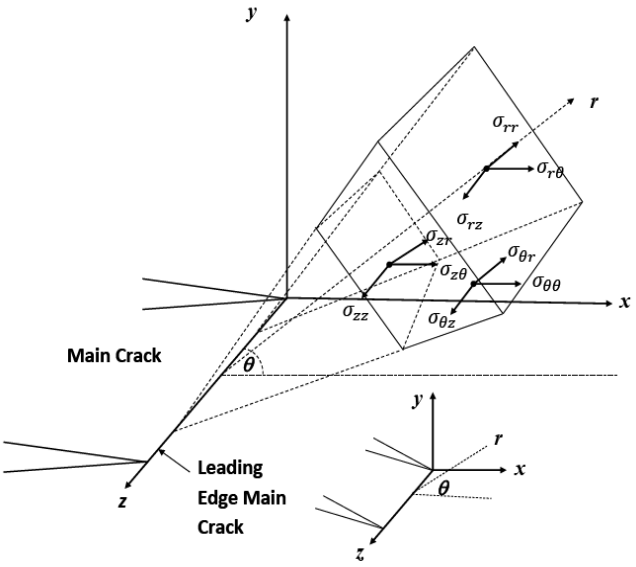

Fig. 1. Mixed mode I/II/III.

In thin ductile sheets, fracture is always a mixed mode affair, involving both the tensile effects (mode I) and out of plane shearing (mode III). To determine the fracture type, the maximum tensile, σ_{max} and shear stresses, τ_{max}, through the sheet thickness are required and compared to the material properties of critical tensile stress, σ_c and the critical stress in shear, τ_c. For tensile fracture; $\tau_{max}/\sigma_{max} < \tau_c/\sigma_c$ and for shear fracture: $\tau_{max}/\sigma_{max} > \tau_c/\sigma_c$ and applying the von Mises failure criteria for ductile materials in mixed mode loading, $\tau_c = 0.577\sigma_c$.

The tensile and shear stresses are obtained by a transformation through the thickness in the *yz*- plane is required. Such an element, through thickness plane, is shown in Fig. 2, the point is located at (ρ, α), where ρ is the distance of the element from the top face through the sheet thickness and α is the slant angle of the advancing crack plane. The slant angle is defined as the angle between propagating crack plane and the original flat crack plane. The slanting crack advance phenomena is observed and recorded in crack growth experiments in thin ductile materials, where the initially flat crack turns to a slant angle, α after a short flat-to-slant transition.

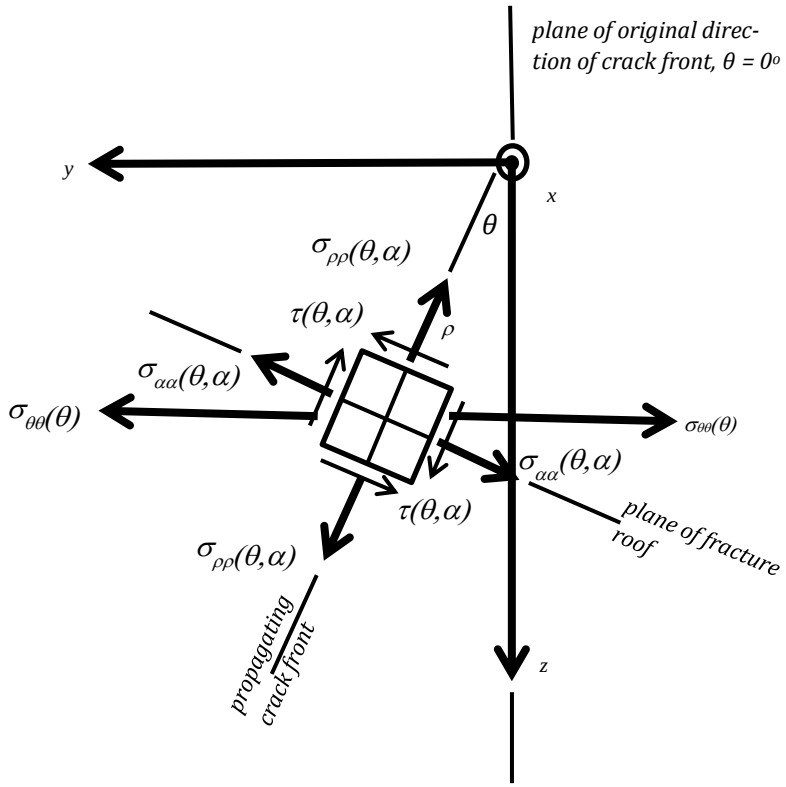

Fig. 2. Element at distance ρ in the *yz*- through thickness plane: Element (θ, α).

Chao and Zhu (1999) and Lui et al. (2004) give that for plane stress conditions, in the through thickness plane, under mode I/III, the crack tip tensile and shear stresses are:

$$\sigma(\theta,\alpha) = \frac{K_I}{\sqrt{2\pi r}} cos^3\frac{\theta}{2} cos^2\alpha - \frac{K_{III}}{\sqrt{2\pi r}} cos\frac{\theta}{2} sin\,2\alpha\,, \qquad (1)$$

$$\tau(\theta,\alpha) = \frac{K_I}{2\sqrt{2\pi r}} cos^3\frac{\theta}{2} sin\,2\alpha + \frac{K_{III}}{\sqrt{2\pi r}} cos\frac{\theta}{2} cos\,2\alpha\,. \qquad (2)$$

The above equations show that when a cracked body is loaded, it is possible that propagation is to occur either along a tensile fracture path at angle θ^* or along a shear facture path at an angle θ^{**} to the original direction of the crack front in the *xy*- plane. Whilst the plane of the crack front propagates inclined at an angle α ($\alpha^*$and α^{**}, tensile and shear respectively) in the through thickness *yz*- plane. In reality, the event is a combination of both individual fracture types, however the contribution of one mode over the other depends upon the mode mixity of loading. The contribution is discussed following the experimental investigation. From Lui et al. (2004) method for mode I/III, using the MNSC, MSSC and MNSC, the material (τ_c/σ_c) property and the stress intensity factors K_I and K_{III}:

$$\theta^* = 0^o \;\;,\;\; \alpha^* = \frac{1}{2} tan^{-1}\left[\frac{2}{-\frac{K_I}{K_{III}}}\right] \;\;,\;\; \frac{K_I}{K_{III}} = \frac{-2}{tan\,2\alpha}\,,$$

$$-\frac{\pi}{4} \le \alpha^* \le 0 \quad for \quad K_{III} \ge 0\,. \qquad (3)$$

In the plane of original direction of crack front, $\theta^* = 0^0$, Fig. 3 and slant angle, α^* the maximum tensile stress:

$$\sigma_{max} = \frac{K_I}{\sqrt{2\pi r}} cos^2\alpha^* - \frac{K_{III}}{\sqrt{2\pi r}} sin\,2\alpha^*\,. \qquad (4)$$

Introducing the critical stress intensity under mode I, $K_{IC} = \sigma_c\sqrt{2\pi r_c}$, where σ_c acts at critical distance from the crack tip r_c, the critical maximum tensile:

$$\frac{K_I}{K_{IC}} cos^2\alpha^* - \frac{K_{III}}{K_{IC}} sin\,2\alpha^* = 1\,. \qquad (5)$$

In Fig. 3, when $\alpha = \alpha^*$ the slant crack front is typically described as a factory roof appearance. $\sigma_{\alpha\alpha}$ is therefore parallel to the factory roof plane. In the case of $\sigma_{\alpha\alpha}(\theta^* = 0, \alpha^*)$, the fracture angle α^*, is also dependant on the loading/mixity angle γ This load mixity angle γ is to varied in this investigation between 0^o and 90^o, ($\gamma = 0^o$ - pure mode I; $\gamma = 90^o$ - pure mode III).

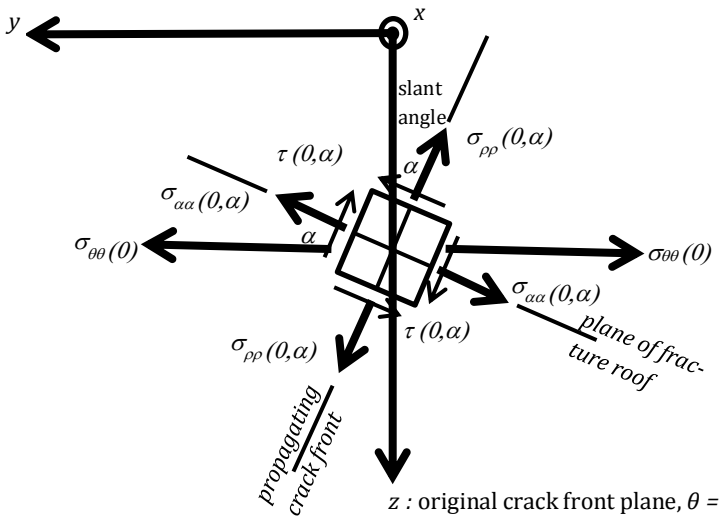

Fig. 3. Element at distance ρ in the *yz*- through thickness plane. Element $(\theta = 0^0, \alpha)$.

The maximum shear stress, along a plane at $\pi/4$ from that of the maximum normal stress, i.e. $\alpha^{**} - \alpha^{*} = \pi/4$, with α^{*} from Eq. (3) and $\theta^{**} = 0$, the slant angle and maximum shear stress are:

$$\alpha^{**} = \frac{1}{2} tan^{-1}\left[\frac{\frac{K_I}{K_{III}}}{2}\right], \tag{6}$$

$$\tau_{max} = \frac{K_I}{2\sqrt{2\pi r}} sin\, 2\alpha^{**} + \frac{K_{III}}{\sqrt{2\pi r}} cos\, 2\alpha^{**}\,. \tag{7}$$

In this condition, the crack roof is at an angle of $(\pi/2 + \alpha^{**})$ from the original crack plane, as shown in Fig. 3. If the maximum shear stress reaches the critical shear stress of the material, with $\tau_c = K_{IC}/\sigma_c\sqrt{2\pi r_c}$, then $(\sigma_c/\tau_c)\left((K_I/2K_{IC})\sin 2\alpha^{**} + (K_{III}/K_{IC})\cos 2\alpha^{**}\right) = 1$. Therefore, for the transition between the type of failure can be concluded according to the equations:

$$\frac{\tau}{\sigma} = \frac{\frac{1}{2}\left(\frac{K_I}{K_{III}}\right) sin\, 2\alpha^{**} + cos\, 2\alpha^{**}}{\left(\frac{K_I}{K_{III}}\right) cos^2\alpha^{*} - sin\, 2\alpha^{*}}, \tag{8}$$

$$\frac{K_I}{K_{III}} = \frac{cos\, 2\alpha^{**} + \frac{\tau}{\sigma}\, sin\, 2\alpha^{*}}{\frac{\tau}{\sigma}\, cos^2\, \alpha^{*} - \frac{1}{2} sin\, 2\alpha^{**}}. \tag{9}$$

2.3. Energy criterion

The work required to propagate a crack by unit area is defined by the essential work of fracture, also referred in literature as the fracture toughness, *R*. The essential work of fracture attains a critical value R_c when cracking initiates, whilst during quasi-static crack propagation, the material will crack at constant *R*.

For a material containing a starter crack of area *A*, the quasi-static incremental interchanges, as the body is loaded by an external force *X* and associated displacement *u*, produces a change in the elastic and plastic strain energy and the fracture work. The level of strain either surrounding the crack tip, or in the surrounding material dictate the strain energies involved.

The work equations are:

$$Xdu = d\Lambda + d\Gamma \quad \text{(before crack propagation) and} \tag{10}$$

$$Xdu = d\Lambda + d\Gamma + RdA$$
(during quasi-static crack propagation). (11)

The essential work of fracture, *R* is obtained from the experimental force-displacement *X*-*u* plots using the energy, *U*. From Eq. (11):

$$R = \left(\frac{\partial U}{\partial A}\right) x = -\left(\frac{\partial U}{\partial A}\right) u\,. \tag{12}$$

During mixed mode I/III loading, for each fixed loading mixity angle, the slant angle initially increases with crack extension, during the flat to slant transition. Eventually a steady state slant angle is achieved. The fracture surface is rough with the actual fracture area larger than the assumed planar surface. As a result of this increased surface, the material fracture process zone requires an increase of the work rate input to the system in the early stages. From the initial flat fracture surface, during the initial stages, the low toughness central region of the sheet material burrows through the material ahead of the surface. The burrowing produces the observed characteristic stretching on the outer surface. The surface is pulled along and propagation occurs under increasing load. The flat starter crack twists into the slant fracture. As a consequence the essential work of fracture also increases during this early transition stage producing the characteristic *R* – *A* crack growth resistance curves. For the thin sheet material tested here, the growth of the large crack tip zone is not completed before the crack starts to advance.

Results show that the *R* curve is characteristic of the material and independent of starting crack length, however dependent with rate, temperature and environment. In addition, it is found that the resistance to cracking, *R* and hence *K*, changes with thickness of the body.

The concept of K and hence R, changing with thickness with specimen thickness is all part of the same related process. Under plane stress conditions there is a low constraint to flow at the outside of the body due to the stress-free surfaces, however when plain strain conditions apply the interior material is not able to flow. Variations of essential work of fracture with material thickness are found in most materials.

2.4. Mode I/III specimen

Different specimens have been used for mixed mode I/III investigations. Sutton et al. (2001) and Lan (2006) use a single edge notch (SEN) plate for in-plane tension-torsion loading. Wei et al. (2005), Yan et al. (2007, 2009), Wei (2011), Li et al. (2011) use a CT SEN plate with a short initial starter crack for out-of-plane mode I/III testing. Zhu (2011) use an all fracture (AFM) rectangular bar SEN specimen.

The specimen chosen for this investigation is an SEN specimen with long initial starter crack length, also commonly called a two legged trouser tear specimen. The trouser tear test was initially used by Rivlin and Thomas (1953) and successive co-workers for the large deformation and non-linear elastic response of sheet rubber. This specimen has been adopted with success by many investigators for ductile sheet materials to determine the essential work of fracture R in pure mode III investigations (Mai and Cotterell, 1984; Muscat-Fenech et al., 1992; Muscat-Fenech and Atkins, 1994a, 1994b; Muscat-Fenech, 1992). Various material models have been used whilst, Muscat-Fenech (1992), Muscat-Fenech et al. (1992), Muscat-Fenech and Atkins (1994a) analyse the energy balance of tearing, mode III, in thin sheet materials made of elastoplastic material. This two legged trouser specimen has proved to provide valid and reliable test data. Muscat-Fenech (1992), Muscat-Fenech et al. (1992), Muscat-Fenech and Atkins (1994a, 1994b) have analysed the effect of the geometrical sizes of leg length, L, leg widths, w and material thickness, t on the ensuing crack path propagation. The leg length has to be sufficient to allow the material to bend and unbend freely as the crack path aligns itself for propagation. The legs widths must be equal, otherwise the crack path will diverge into the narrow leg with region, Muscat-Fenech and Atkins (1994a, 1994b).

For any material model characteristics, ranging from elastic to elastoplastic to rigid plastic, the work energy Eq. (11), as shown by the investigators who have successfully adopted this method as described above, always result in an equation of the form:

$$\frac{X}{t} = \frac{R}{2} + w \quad \{function\ of\ \sigma_y, \rho, E, t, \xi\}. \tag{13}$$

The variables in the { } brackets are geometrical and material properties. ρ is the radius of curvature of the leg width w, which is different in magnitude for each leg width, w of thickness, t and hence a function of the level of the plastic region ξ through the sheet thickness. The {function of $\sigma_y, \rho, E, t, \xi$} describes the strain energy per unit volume and encompasses and represents all the bending, unbending and twisting work interchanges experienced by the legs.

The above equation would at first glance indicate that a plot of force per unit thickness, (X/t) versus leg width, w gives a straight line with intercept $(R/2)$. However this is *not* the case. The straight line indicated in Eq. (13) is usually a best fit polynomial curve. The typical curve increases in value, maximises and then decreases as the leg width increases, (also present in this investigation). This occurrence is due to the competition and balance between the work of fracture W_f and the work of un/bending W_b and work of twisting W_T, Muscat-Fenech et al. (1992, 1994a). The work of un/bending and twisting are far from unimportant as often inferred by many investigators. In fact the specimens used by Wei et al. (2005), Yan et al. (2007, 2009), Wei (2011), Li et al. (2011) clearly shows the clamping region with sharp kinks at the edges of the clamps and the overall specimen deformation. The leg lengths are too short to allow the natural irreversible plastic deformation work to form completely and allow complete un/bending and un/twisting of the specimen. This surely had an effect on the crack tip stress and strain field, the angle of crack propagation and angle of the slant crack front.

2.5. Link between the energy and crack tip stress methods

The energy and crack tip stress (involving the stress intensity factors) methods both describe the same process. The essential work of fracture R, quantifies the net change in energy that accompanies an increment of crack extension; whilst the stress intensity factor K quantity characterizes the stresses, strains and displacements near the crack tip. The energy release rate describes global behaviour, whilst the stress intensity factor is a local parameter. As such K has nothing to do with fracture. However, for a specimen undergoing deformation the total strain energy stored per unit volume $= (1/2)\,\sigma\,\epsilon = (1/2)(\sigma^2/E)$ is obtained as the area under the force displacement, X-u plot. Griffith proposed that the elastic energy stored in the plate due to the presence of the crack to be: $U* = \sigma^2 \pi a^2\, t/E$ resulting that $\sigma = K/\left(Y\sqrt{\pi a}\right)$. In principle σ may be substituted in terms of K, such that $(1/2)(K^2/EY^2\pi a)$ and is integrated for the whole body. Therefore the R in quasi-static propagation must also be expressible in terms of K, hence the K of the propagating crack also serves to characterise a material's resistance to crack propagation and it may be an alternative parameter to R. The process zones contains the fracture events themselves and the K dominated characterisation of fracture can be successfully applied so long as the process zone is small around the crack tip. Atkins and Mai (1985), Anderson (2005), amongst many others, both report that from many experiments by other researchers, that test pieces using the same material give comparable constant K value during propagation as does R. Whilst many associate K to (σ, a) combinations at the start of cracking, this constant K that ensues with cracking is in fact like R. In fact, both the K and R values are often referred to as fracture toughness, explaining why in this work R is referred to as the essential work of fracture

and K as the stress intensity factor. The confusion between the two normally arises since the stress intensity factor $K = \sigma Y\sqrt{\pi a}$ is produced in a cracked body by the applied stress σ and the critical stress intensity factor K_c is of the material. When cracking occurs, the applied stress intensity factor reaches the critical value. K and R are related via Young's Modulus E, by the equation $K^2 = ER$. Equations involving the essential work of fracture R determine the loads and therefore the stress to cause fracture as does the above equation for $= \sigma Y\sqrt{\pi a}$, therefore a relation between the two must exist. Just as K refers to the mode of opening by the subscripts I, (II) and III, R is normally written as simple R without a subscript, here the notation to describe the mode of opening is to be extended and use the same notation of I, (II) and III to R.

2.6. Separation of the essential work of fracture mode I/III components

Hill (1953) originally suggested a yield criterion of ductile sheets in which the specimens form localised necks along the line which will develop into fracture. The mode I/III test specimens clearly show how the originally full thickness crack edge, not only turns and adjusts itself along the slant angle α, depending on the mode mixity γ, but also shows visible localised necking. The direction of slant angle α through the material thickness, is suggested here, to follow Hill's theory, such that: $\tan\alpha = (1/4)\cot\gamma$. The loading or mixity angle, γ is varied such that $\gamma = 0^0$ (mode I) and $\gamma = 90^0$ (mode III), to follow Hill's loading angle direction terminology. The relative motion as the crack proceeds with the mixity angle γ is illustrated in Fig. 4 and this approach allows the total essential work of fracture under mixed mode loading I/III to be split into its individual pure mode components.

The relationship of the direction of relative motion with ratio of strains is:

$$tan\,\alpha = \frac{u_{III}/u_{III_o}}{u_I/u_{I_o}} = \frac{\epsilon_{III}}{\epsilon_I}, \tag{14}$$

where u_I and u_{III} are the change in length, with respect to mode I and III, of the original gauge length u_{I_o} and u_{III_o} respectively, with the strains ϵ_I and ϵ_{III} parallel to the mode I and Mode III axes respectively as marked as gauge length points on the specimens..

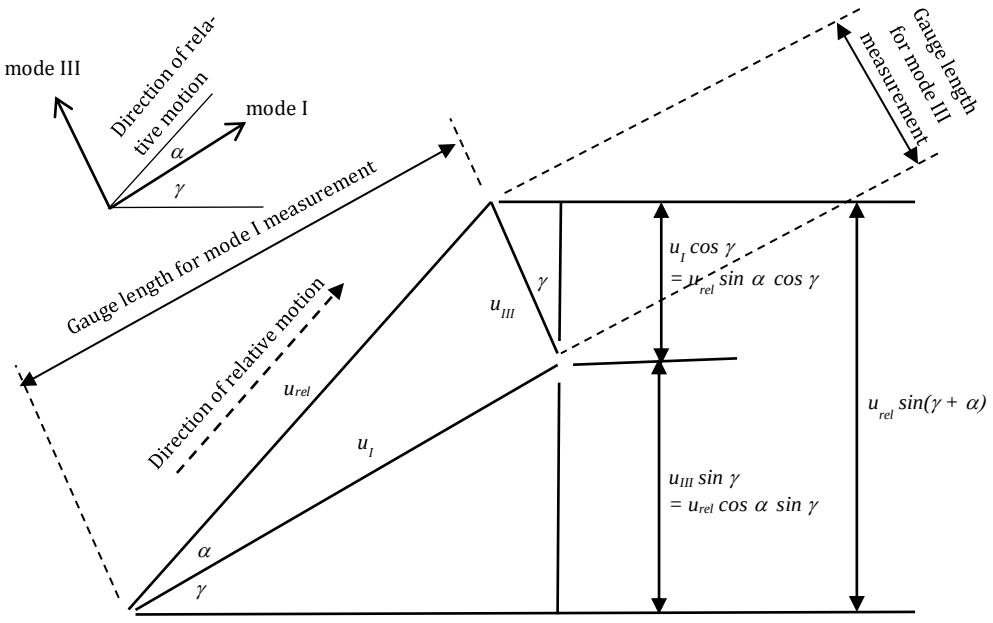

Fig. 4. Displacement components for mode I/III.

From the specimen geometry and displacements, the cross head, displacement $u_{m/c}$ can be defined as:

$$u_{m/c} = \epsilon_I u_{I_t} cos\,\gamma + \epsilon_{II} u_{IIIt}\, sin\,\gamma = u_{rel}\, sin\,\alpha\, cos\,\gamma + u_{rel}\, cos\,\alpha\ sin\,\gamma = u_{rel}\, sin(\gamma + \alpha)\,, \tag{15}$$

where u_{I_t} and u_{III_t} are instantaneous measured total length between the gauge indicators in the respective directions.

Moreover in a ductile body (such as steel), the deformation occurs in the direction at which the body is being loaded, therefore, considering the deformation into each mode, such that, $u_I = f(R_I)$ and $u_{III} = f(R_{III})$, then:

$$\frac{u_I}{u_{III}} = f(\,tan\,\gamma)\,, \tag{16}$$

$$\frac{u_{III}}{u_I} = g\left(\frac{R_{III}}{R_I}\right) = h(cot\,\gamma, tan\,\alpha)\,. \tag{17}$$

Since the total energy contribution during loading is:

$$U_T = \int_0^{u_{m/c}} X\ du = X u_{rel}\, sin(\gamma + \alpha)\,, \tag{18}$$

The total energy U_T is split into the two modes I and mode III, U_I and U_{III}, as follows:

$$U_I = \int_0^{u_I} X\ du = X u_{rel}\ sin\alpha\ cos\gamma\ ,$$

$$U_{III} = \int_0^{u_{III}} X\ du = X u_{rel}\ sin\gamma\ cos\alpha\ . \quad (19)$$

From Eq. (12), the total essential work of fracture, R and the components in the I and III direction are:

$$R = -\frac{\partial(U_t)_u}{\partial A} = \frac{X}{Lt} u_{rel}\ sin(\gamma+\alpha)\ , \quad (20)$$

$$R_I = -\frac{\partial(U_I)_u}{\partial A} = \frac{X}{Lt} u_{rel}\ sin\alpha\ cos\gamma\ ,$$

$$R_{III} = -\frac{\partial(U_{III})_u}{\partial A} = \frac{X}{Lt} u_{rel}\ cos\alpha\ sin\gamma\ . \quad (21)$$

The percentage contributions of each mode essential work of fracture, $\%R_I$ and $\%R_{III}$, to the total R with the varying loading mixity angle, 0^0(mode I) $< \gamma <$ 90^o(mode III), is expressed as:

$$\%R_I = \frac{R_I}{R} = \frac{sin\alpha\ cos\gamma}{sin(\gamma+\alpha)}\ ,$$

$$\%R_{III} = \frac{R_{III}}{R} = \frac{sin\gamma\ cos\alpha}{sin(\gamma+\alpha)}\ . \quad (22)$$

Hence, for quasi-static cracking in plane stress conditions, applying the standard relationship, $K^2 = ER$, together with Hill's yield criterion and ratio R_{III}/R_I gives:

$$\frac{R_{III}}{R_I} = \frac{\frac{X}{Lt}u_{rel}\ cos\alpha\ sin\gamma}{\frac{X}{Lt}u_{rel}\ sin\alpha\ cos\gamma} = \frac{cos\alpha\ sin\gamma}{sin\alpha\ cos\gamma} = \frac{tan\gamma}{tan\alpha} = 4\ tan^2\gamma =$$

$$\left(\frac{K_{III}}{K_I}\right)^2 R = -\frac{\partial(U_t)_u}{\partial A} = \frac{X}{Lt} u_{rel}\ sin(\gamma+\alpha)\ , \quad (23)$$

Substituting Eq. (24) into mode I/III Eq. (9) in terms of τ/σ , $\alpha^*$and α^{**}, then:

$$\frac{R_I}{R_{III}} = \left[\frac{cos\ 2\alpha^{**}+\frac{\tau}{\sigma}\ sin\ 2\alpha^*}{\frac{\tau}{\sigma}\ cos^2\alpha^*-\frac{1}{2}sin\ 2\alpha^{**}}\right]^2\ , \quad (24)$$

3. Experiments: Material, Specimen and Fixtures

The mixed mode I/III specimens are manufactured from galvanised low carbon steel, grade: DX51D. The mechanical properties of the material, in orientations of 0^0, 45^0 and 90^0 to the cold roll direction, are shown in Table 1, were determined in accordance with BS EN ISO 6892-1, 2009. (Instron 4206 tensile testing machine, crosshead machine speed of 1.8mm/min according to range 2.)

Table 1. Material Properties for DX51D.

Angle to rolling direction, ^{0}	0	45	90	Average
Young's Modulus, *E*, GPa	198	203	197	198
Ultimate Tensile Strength, MPa	355	354	357	355
Lower Yield Strength, MPa	313	305	297	305
Upper Yield Strength, MPa	321	324	303	318
Strain Hardening Exponent, *n*	0.279	0.323	0.291	0.304
Strength Coefficient σ_o, MPa	670	701	683	689

Mixed-mode I/III testing was performed on two legged specimens, Fig. 5. The material is of thickness, *t* of 0.6 mm and 1mm and leg widths, *w* of 12 mm, 24 mm, 36 mm and 48 mm, the total overall specimen length of 150 mm, allows a 12 mm clamping length, with starter crack lengths, *a* of 100 mm. The length of the leg or starter crack length *a*, was decided upon after several specimens were bent to ensure that the length of the leg is adequate for a natural curvature to form and prevent kinking in the clamped regions.

Specimens were clamped in the specially designed mixed-mode I/III jigs. The fixtures were designed to ensure no rotation of the fixture when coupled with the testing machine, such that in- and out-of-plane un/bending or twisting of the specimen is due to the test conditions. The specimens were loaded by the displacement controlled Instron 4206 tensile machine, with a crosshead machine speed of 8 mm/min. The load mixity angles chose are: $\gamma = 90^0$ (Pure Mode III), 67.5^0, 45^0 and 22.5^0. Pure mode I, $\gamma = 0^0$, testing conditions were not undertaken since proper pure mode I loading could not be established. However, the Mode I data $\gamma = 0^0$, was obtained from De Marco Muscat-Fenech and Ciappara (2013), since the same material was used in both investigations.

4. Experimental Results and Discussion

4.1. Essential work of fracture, R

Graphs of load-displacement were plotted for all the specimens obtained from data acquisition, with a sampling rate every 0.25s. Fig. 6, shows the force-displacement, *X-u* graphs, tests carried out at a loading mixity angle of $\gamma = 67.5^0$ and leg widths *w* = 12, 24, 36 and 48mm for specimens having a thickness of 1mm. The graphs illustrated in Fig. 6 being typical of the tests carried out in this investigation.

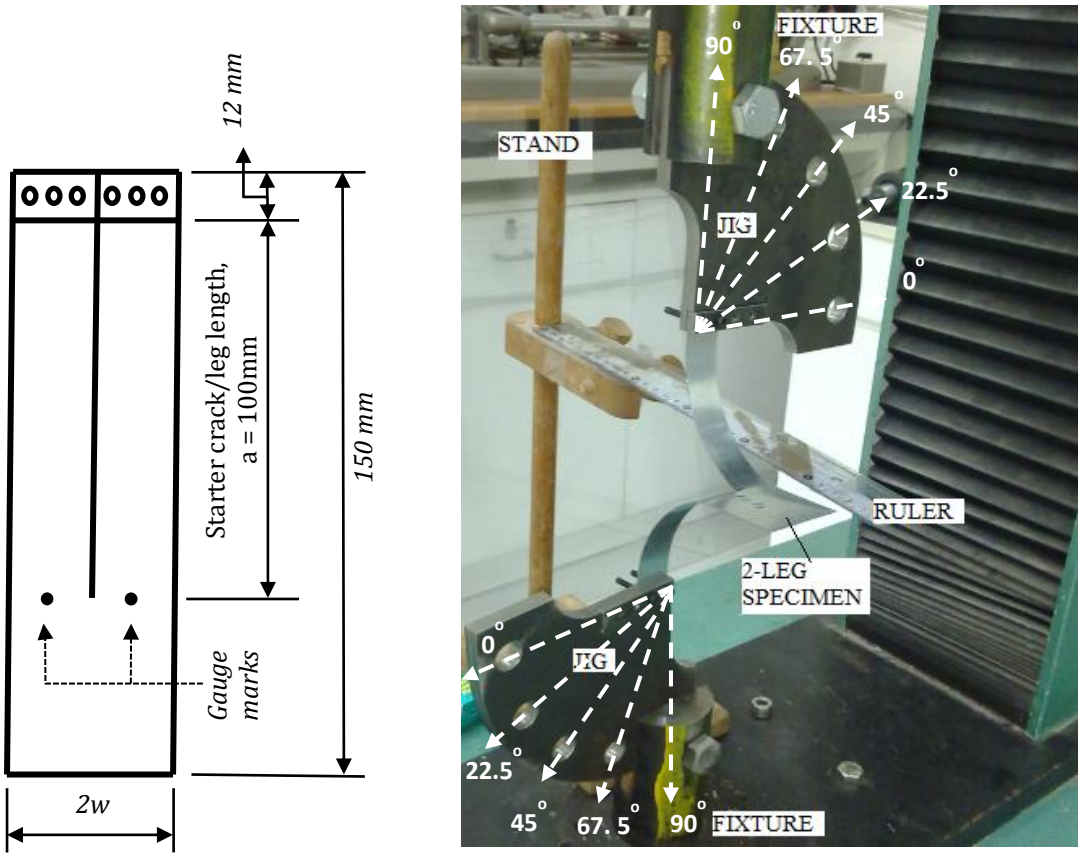

Fig. 5. Mode I/III specimen testing: (a) specimen; (b) testing $\gamma = 90^0$.

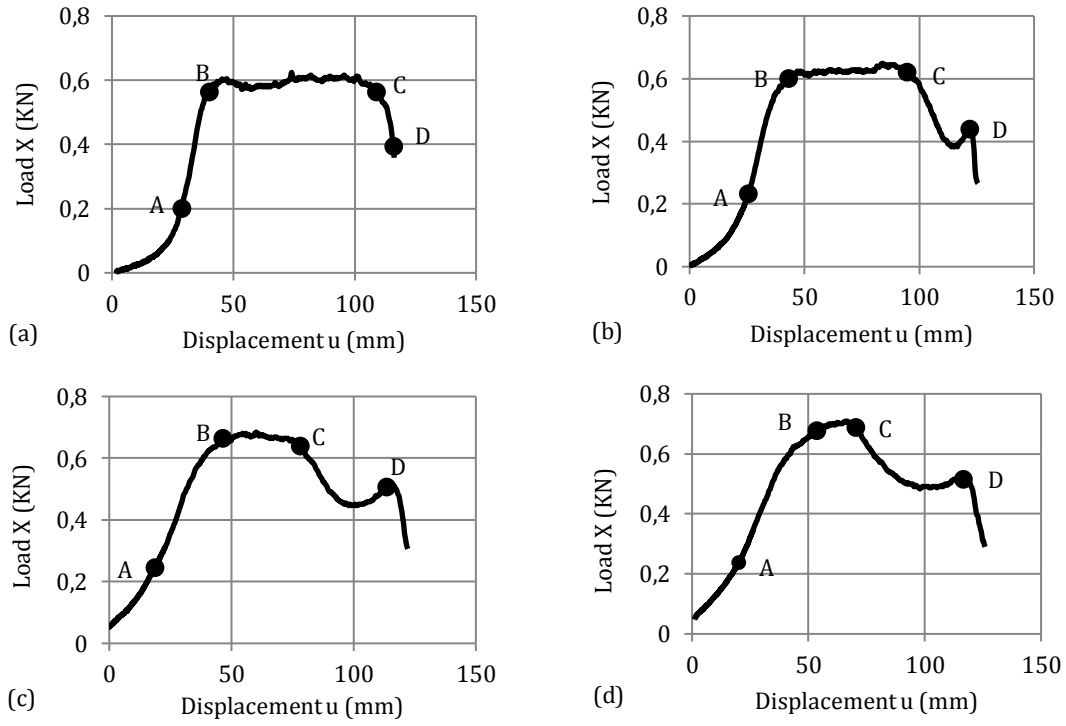

Fig. 6. Load-displacement graphs at loading angle $\eta = 67.5^0$, sheet thickness, t = 1mm, leg width: (a) w = 12mm; (b) w = 24mm; (c) w = 36mm; (d) w = 48mm.

A, B, C and *D*, are important points of interest for understanding the process during mixed-mode I/III testing, which will be used to extract useful information. From the origin *O* to point *A,* work is done to un/bend and twist the legs. Point *A* is the instant of visible tip deformation. Initially the magnification x50 of the camera was utilised to ascertain the onset of this deformation and a trained experimental eye for this instant was required. Point A marks the initial stage of the changes to occur ahead of the flat fracture surface. On the line between point A and B, the low toughness central region of the sheet material burrows through the material ahead of the surface, the crack tip is forming the characteristic triangular highly localised stretching region. During this time the crack tip front is orientating to establish its natural direction, the flat starter crack twists into the slant angle for the ensuing crack propagation. Growth of the large crack tip zone is not always complete before the crack starts to advance.

Point B marks the onset of crack propagation. Crack detection strain gauges placed as close as possible to the manufactured crack tip, but not in the triangular region detected the onset of the ensuing crack advance, in addition to visual observation of the onset of propagation. From point B up to C the crack propagates at constant load. This constant average force value is of particular interest in calculating the essential work of fracture, *R,* during stable crack propagation. Of noticeable interest is the fact that, as the leg width, *w* increases the constant force stable crack propagation magnitudes, first increases, maximises and subsequently starts to drop in value. This occurrence is very common and expected in two legged trouser tear tests. After point C, the load started to decrease, this results due to edge effects. The crack front is experiencing sizing and edge effects as in standard SIF test piece sizing problems. At point D, the load increased as the crack reached the edge of the specimen, when the specimen separated.

Applying Eqs. (12) or (13), the force per unit thickness, (X/t) for the varying widths, *w* for the different thickness, *t* and loading mixity angles γ, are plotted. First considering the values at the point, *A*, initiation of visible tip deformation; then for the constant crack propagation force values between the points *B* and *C* when stable and established crack propagation is occurring. The plots are shown in Figs. 7 and 8 respectively for both sheet thickness, *t* = 0.6 mm and 1.0 mm.

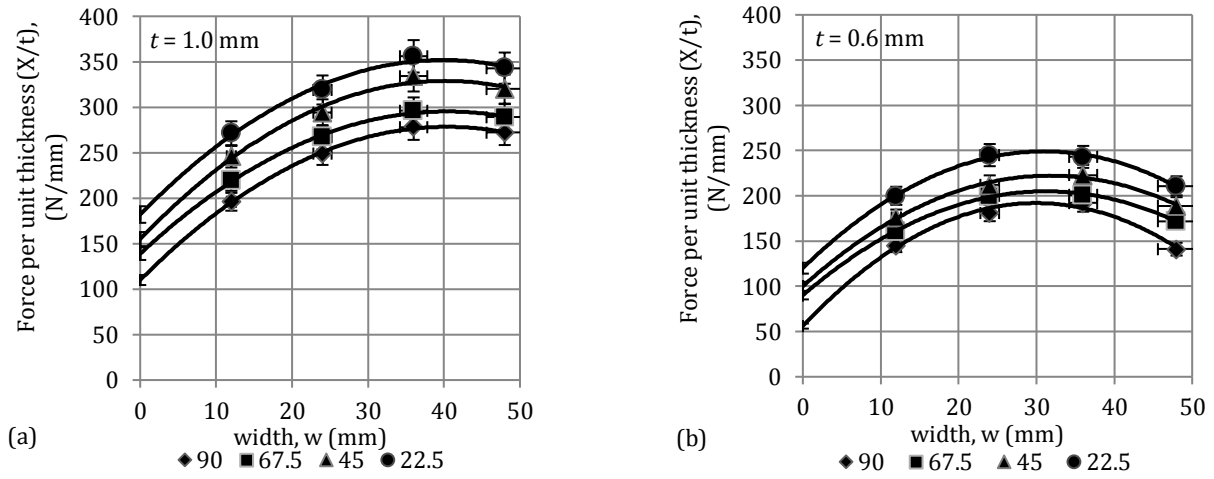

Fig. 7. Graphs of (load/thickness), (X/t), against width, *w*, at initiation point *A*, loading angles $\gamma = 90^0, 67.5^0, 45^0 and\ 22.5^0$. 5% error bars shown. Specimen sheet thickness: (a) *t* = 0.6 mm; (b) *t* = 1.0 mm.

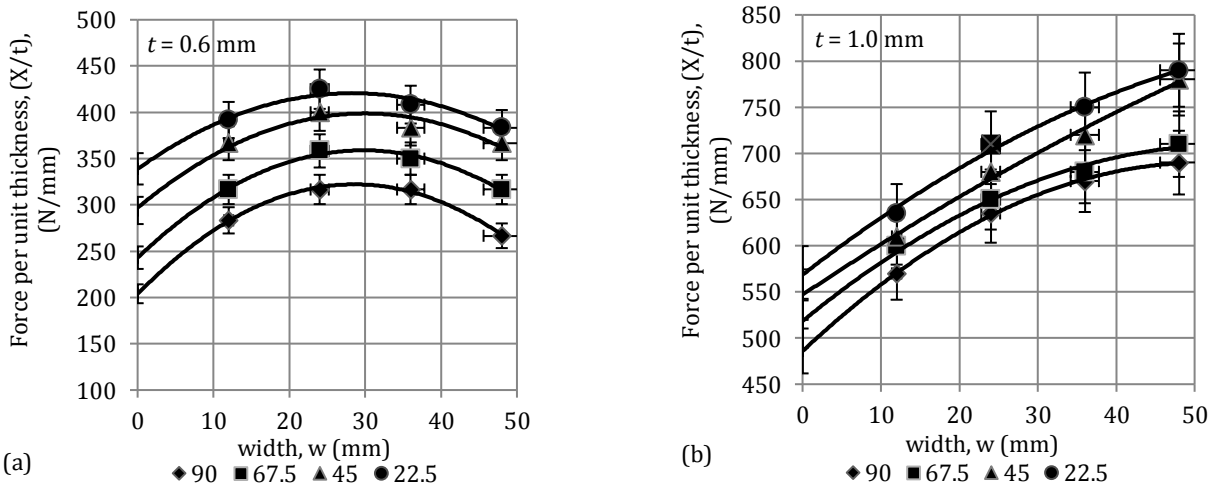

Fig. 8. Graphs of (load/thickness), (X/t), versus width, *w*, during crack propagation (*B* to *C*), loading angles γ = 90⁰, 67.5⁰, 45⁰ and 22.5⁰. 5% error bars shown. Specimen thickness: (a) *t* = 0.6 mm; (b) *t* = 1.0 mm.

From the plots of (X/t) versus w, as first observed by Muscat-Fenech (1992, 1994a) that such curves do not exhibit a linear behaviour as original intended by Mai and Cotterell (1984). Muscat-Fenech et al. (1992, 1994a) showed how the curvature of the leg ρ increases as the width w (and also the thickness, t) of the leg increases, the curvature is attributed to the varying amounts of the elastic and plastic work occurring during the process, i.e. the competition between the work of fracture W_f, the work of un/bending W_b and work of twisting W_T. In narrow leg widths of material of the same thickness, t, the work of fracture has the dominant effect of the system, whilst as the leg width increases, the work contributions to un/bending and twisting start to equal and then surpass the work of fracture. Consequently, also as the sheet thickness increases, the elastic work/energy plays a major role in the process which is readily noticeable when comparing the same material of various thicknesses, Figs. 7 and 8. The resulting curves are locus lines of the constant magnitudes of the essential work of fracture, R. The intercept on the (X/t) axis according to theory (Eq. (13) gives a value of $(R/2)$).

The values of essential work of fracture for crack initiation and propagation obtained from Figs. 7 and 8 are given for comparison in Table 2. As expected the variation of values of the essential work of fracture have occurred with the difference in material thickness. A common occurrence and is expected in ductile materials, as in the case that the stress intensity factor varies with thickness. R and K are closely related since the energy and crack tip methods both describe the same process.

4.2. Mixed mode components R_I and R_{III}

The procedure developed, taking into account the geometrical and testing conditions for the mode I/III investigated here, allows the total essential work of fracture under mixed mode loading I/III to be split into its individual pure mode components R_I and R_{III} for the various mixity angles, γ using Eqs. (22) and (23). The combined essential work of fracture and individual values at each mixity angle are given in Table 3 and plotted in Fig. 9.

Table 2. The essential work of fracture, R at initiation and crack initiation (Figs. 7 and 8 respectively, using Eq. (13)) for different loading angles and sheet thickness.

	$R_{\text{initiation}}$ (N/mm)		$R_{\text{crack propagation}}$ (N/mm)	
γ (deg)	t = 0.6 mm	t = 1 mm	t = 0.6 mm	t = 1 mm
90.0	112	220	408	972
67.5	180	278	486	1036
45.0	201	310	594	1094
22.5	242	364	678	1137

Table 3. Essential work of fracture $R_{I/III}$ and components R_I and R_{III}.

γ (deg)	90 (mode III)	67.5	45	22.5	0 (mode I)
			t = 0.6 mm		
$R_{I/III}$ (N/mm)	408	486	594	678	363
R_I (N/mm)	0	20	119	402	363
R_{III} (N/mm)	408	466	475	276	0
			t = 1 mm		
$R_{I/III}$ (N/mm)	972	1036	1094	1137	364
R_I (N/mm)	0	43	219	674	364
R_{III} (N/mm)	972	993	875	463	0

4.3. Validation of Hill's theory. Relation to the work/energy method and crack propagation direction

The findings below are to serve the following purposes. To investigate:
1. the validity of Hill's (1953) theory together with the relationship of the work/energy approach,
2. to compare the work/energy approach with the crack tip stress approach
3. the crack angles and direction

1. *Validity of Hill's theory and energy approach:* Using Hill's theory and the work energy method, the variation in the ratios R_I/R_{III} and therefore K_I/K_{III} can be investigated according to the loading/mixity angle γ, using Eq. (23), tabulated in Table 4 and plotted in Fig. 10.
2. *Crack tip stress approach:* Using the crack tip stress approach for values of the ratio and τ/σ, the K_I/K_{III} and R_I/R_{III} values can be plotted, applying Eqs. (9) and (24), Fig. 11.

Using the experimental values of the DX51D steel sheet tested under pure mode I and mode III, the average

ratio values of R_I/R_{III} and the corresponding values K_I/K_{III} are calculated. For the mode I/III theory based on the K_I/K_{III} value, the angles α^*, α^{**} and τ/σ can be evaluated, Table 5. For this low carbon steel material, DX51D, as investigated here, for the experimentally evaluated R_I/R_{III} ratio, the strength ratios predicted by the theory lie between $0.7 < \tau/\sigma < 0.77$; the τ/σ value range found is an acceptable for steel sheet.

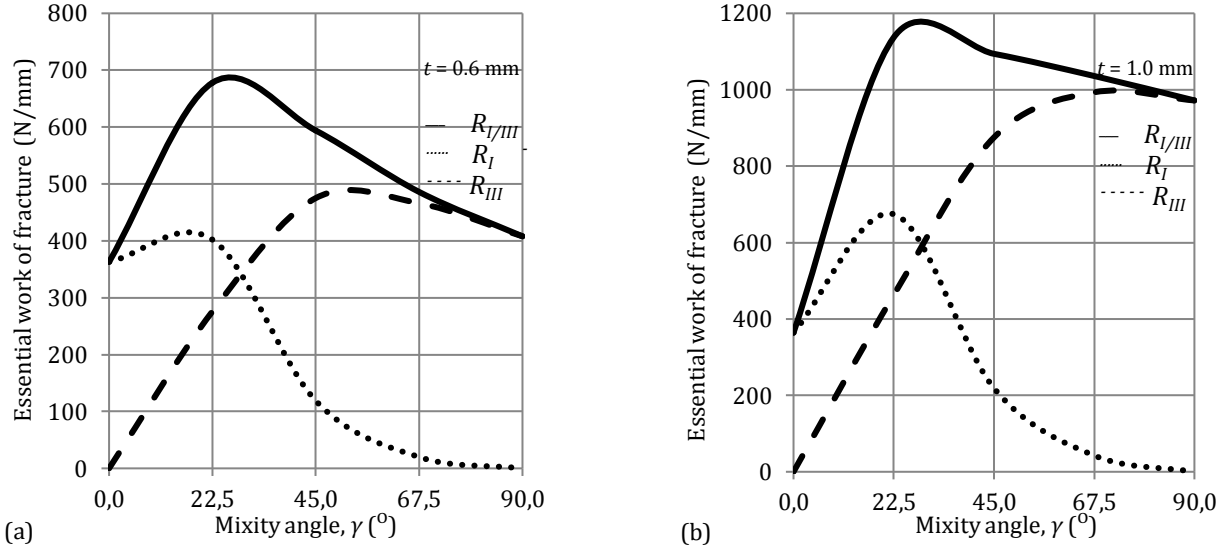

Fig. 9. Graphs of $R_{I/III}$, R_I and R_{III} versus the loading/mixity angle γ: (a) t = 0.6 mm; (b) t = 1.0 mm.

Table 4. R_I/R_{III} and K_I/K_{III} ratios for the variation in the loading/mixity angle γ.

γ (deg)	90 (mode III)	67.5	45	22.5	0 (mode I)
R_I/R_{III}	0	0.04	0.25	1.46	∞
K_I/K_{III}	0	0.2	0.5	1.2	∞

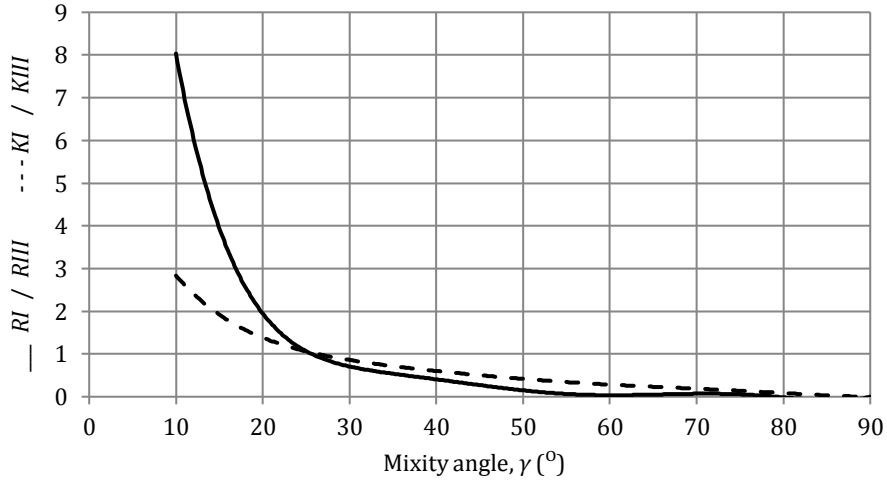

Fig. 10. Variation in ratios R_I/R_{III} and K_I/K_{III} with the loading/mixity angle γ.

3a. *Crack slant angles:* The crack tip stress theory predicts, applying Eqs. (3), (6) and (9), the angles α^* and α^{**} for the various τ/σ values. The relationship $K^2 = ER$, links the loading/mixity angle γ ((Eq. (23)) to the angles α^* and α^{**}. These theoretical relationships between all these variables and the experimental slant angle α (Table 6) are shown in Figs. 12 and 13, respectively. The experimental slant angle data clearly show very close proximity to the α^{**} shear failure curve. Fig. 14 shows the final link between the energy/work method to the crack tip stress approach, (applying together Hill's theory, the energy/work method and mode I/III theory presented here). Using the von-Mises, τ_c/σ_c=0.577 tensile to shear failure transition line, Fig. 14 shows that for the material tested the transition from tensile-to-shear failure occurs at: loading/mixity angle, $\gamma = 13.1^0$, $R_I/R_{III} = 4.62$, $K_I/K_{III} = 2.156$, $\alpha^* = -21.47$, $\alpha^{**} = 23.5^0$.

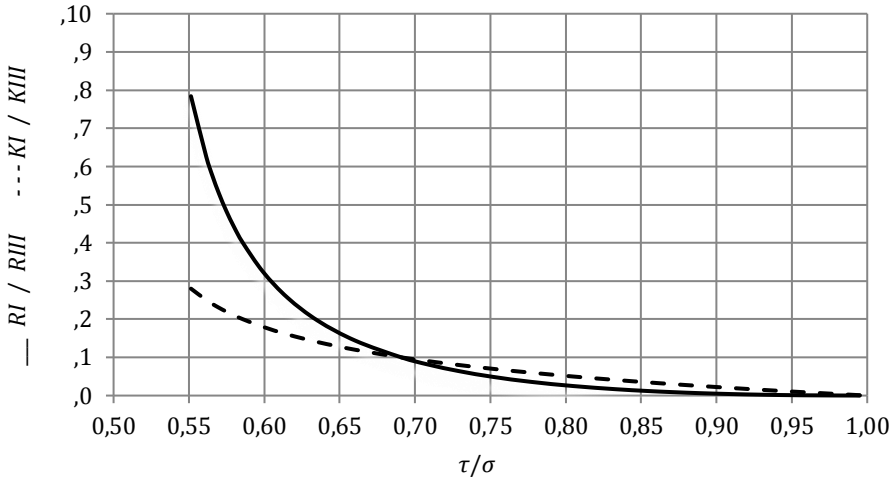

Fig. 11. Variation of τ/σ with K_I/K_{III} and R_I/R_{III} using the crack tip stress approach.

Table 5. DX51D sheet experimental/mode I/III theory evaluation.

Thickness t (mm)	0.6	1.0
R_I (N/mm)	363	364
R_{III} (N/mm)	408	972
R_I/R_{III}	0.89	0.37
K_I/K_{III}	0.94	0.61
α^* (deg)	32.4	36.5
α^{**} (deg)	12.6	8.4
τ/σ	0.70	0.77

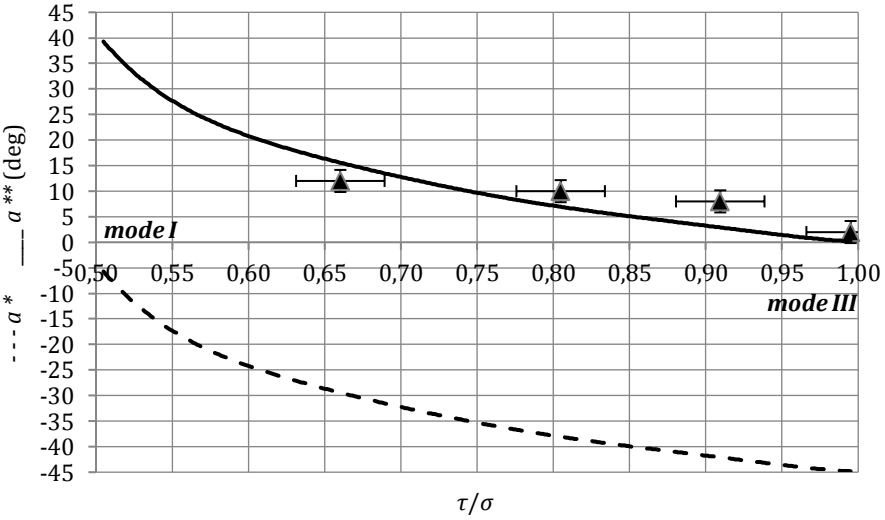

Fig. 12. Variation of α^* and α^{**} with τ/σ , ▲ experimental showing the standard error.

3b. *Crack path direction:* Every specimen, for each leg width w, thickness t and mixity angle γ, the value of the experimental direction angle of the crack path θ were obtained by measurement. The experimental direction angle of the crack path θ, for such tests is expected and also predicted by theory to be 0°. This crack path direction is also noted by Muscat-Fenech (1992), Muscat-Fenech and Atkins (1994a), who show that the direction of the crack path is simply a function of the relative widths of the leg widths w and any deviation is soley dependant on the relative leg widths. For equal widths the crack path is down the centre line. With slight variations of differences in the leg widths, the crack path diverges from the centre line kinking into the narrower width material section. During the experimental work the crack path deviation from the centre line was noted to be very minimal, only up to maximum angles of 3°, within experimental error.

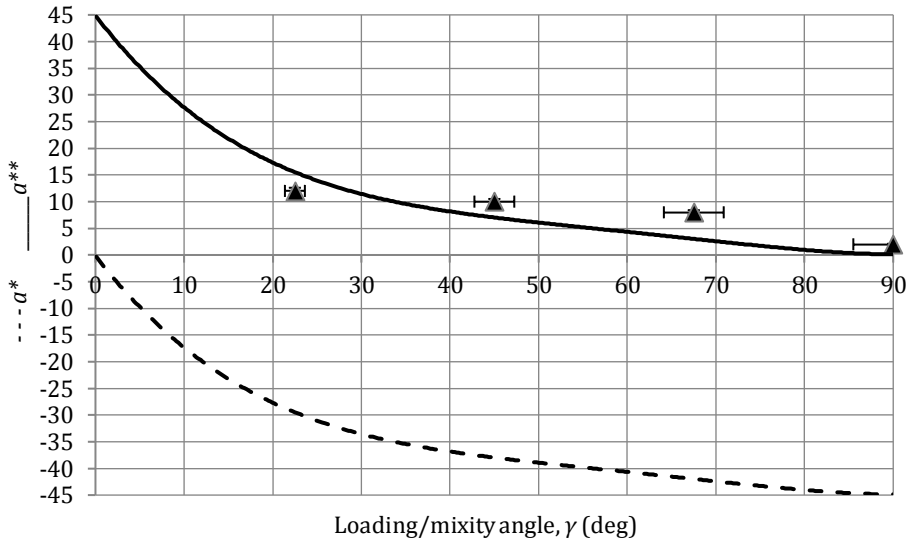

Fig. 13. α^* and α^{**} vs loading/mixity angle γ , ▲ experimental showing the standard error.

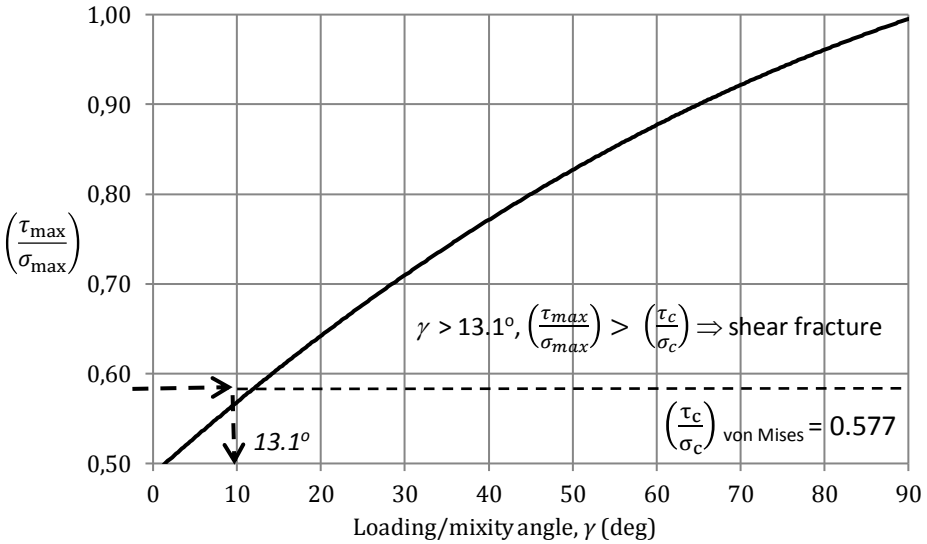

Fig. 14. $\tau_{\max}/\sigma_{\max}$ vs loading/mixity angle, γ.

For the test specimen, using this set-up of mode I/III fracture, for the experimental variation of γ, $22.5^0 < \gamma < 90^0$, theory predicts that failure is by shear. To check the validity of this statement for each mode mixity angle γ the average experimental α^{**} (for shear failure) are evaluated and compared with the experimentally measured angles as given in Table 6 (the values of α represent the average values of the varying leg widths and material thickness). The angles measured for both sheet thickness showed very similar results, the only slightly noticeable differences are that in some of the 1.0mm sheet, shear lips with a central slant were only slightly visible. The phenomena associated with ductile fracture surfaces when plane strain is characteristic of the interior material, where the adjacent material prevents lateral contraction and at the surface plane stress prevails.

Table 6. Crack plane slant angle, $\boldsymbol{\alpha}$ for the various loading mixity, $\boldsymbol{\gamma}$.

mode mixity γ (deg)	α exp (deg)	α^{**} theo (deg)	α^{*} theo (deg)
90 (mode III)	2	0.00	-45.00
67.5	8	2.95	-42.04
45	10	7.02	-37.98
22.5	12	15.56	-29.44
0 (mode I)	N/A	45.00	0.00

The results presented here have conclusively shown that Hill's theory is valid, the comparison and use of the work/energy approach with the crack tip stress approach can be combined and utilised and the fracture mechanism (tensile or shear) can be predicted together with the numerical values of the slant crack angle.

5. Conclusions

The investigation clearly shows a link between the application of the two well-known methods of crack tip stresses and the energy based equations governing crack initiation and propagation in the mixed mode I/III fields. The Maximum Hoop stress Criterion (MHSC) and the Maximum Normal Stress Criterion (MNSC), together with the Tresca and Von-Mises failure theories have successfully been applied to determine the fracture type when the specimens are subjected to a mode I/III field loading. The two leg trouser test specimen which is successful in pure mode III applications using the energy approach was further extended to determine the mixed mode I/III essential work of fracture by varying the mode mixity angle from 0^o (pure mode I) to 90^o (pure mode III). Together with Hill's criterion for ductile fracture the ratio of the essential work of fracture under both modes, consequentially the stress intensity factors and direction of relative motion was predicted according to the mode mixity angle. The energy approach using a locus of constant essential work of fracture for each mixity angle was found and the same expected trend of falling force per unit thickness as the leg width increased was shown. The total mode mixity essential work was successfully portioned to each % contribution to both modes, R_I and R_{III}, as the mixity angle was varied. The R_I/R_{III} and K_I/K_{III} using both the energy and the crack tip stress approaches showed good agreement. For the DX51D sheet material, $0.7 < \tau_c/\sigma_c < 0.8$ show that the crack tip stress theory predicts crack angles in good agreement with experiment. Using the Von-Mises failure criterion, the transition from tensile to shear fracture occurs when the mode mixity angle is small, 13.1^o and slant angle, i.e. the "rooftop" is 23.5^o with $K_I/K_{III} < 2.156$ for all results.

References

Anderson TL (2005). Fracture Mechanics*:* Fundamentals and Applications. 3rd ed., Taylor & Francis.

Atkins AG, Mai YW (1985). Elastic and Plastic Fracture: Metals, Polymers, Ceramics, Composites, Biological Materials. Ellis Horwood Limited.

BS EN ISO 6892-1 (2009). Metallic materials- Tensile testing. Part 1: Method of test at ambient temperature.

Chai H (1988). Shear fracture. *International Journal of Fracture*, 37, 137–159.

Chao YJ, Liu S (1997). On the failure of crack under mixed-mode loads. *International Journal of Fracture*, 87, 201–223.

Chao YJ, Zhu XK (1999). A simple theory for describing the transition between tensile and shear mechanisms in Mode I, II, III and mixed-mode fracture. *In Mixed-mode Crack Behaviour*, [ed.] McDowell D. L. Miller.

Chen X, Jiao G, Cui Z (1986). Application of combined-mode fracture criteria to surface crack problems. *Engineering Fracture Mechanics*, 24(1), 127–144.

De Marco Muscat-Fenech CM, Ciappara S (2013). Connecting the Essential Work of Fracture, Stress Intensity Factor, Hill's Criterion in Mixed Mode I/II Loading. *International Journal of Fracture*, 183, 187-202. DOI 10.1007/s10704-013-9886-4.

Eftis J, Liebowitz H (1972). On the modified Westergaard equations for certain plane crack problems. *International Journal of Fracture,* 8, 383.

Erdogan F, Sih GC (1963). On the crack extension in plates under plane loading and transverse shear. *ASME Journal of Basic Engineering*, 85D, 519–527.

Feng X, Kumar AM, Hirth JP (1993). Mixed mode I/III fracture toughness of 2034 aluminium alloys. *Acta Metallurgical Materials*, 41(9), 2755–2764.

Helm JD, Sutton MA, Boone ML (2001). Characterizing crack growth in thin aluminium panels under tension-torsion loading using three-dimensional digital image correlation. *American Society for Testing and Materials*, STP 1323, 3–14.

Helm JD, Sutton MA, Dawicke DS, Boone ML (1997). 3D computer vision applications for aircraft fuselage materials and structures. *1st joint DoD/FAA/NASA Conference on Aging Aircraft* in Ogden, Utah, 1327–1341.

Hill R (1953). A new method for determining the yield criterion and plastic potential of ductile metals. *Journal of the Mechanics and Physics of Solids*, 1, 271- 276.

Hsia KJ, Zhang TL, Socie DF (1995). Effect of crack surface morphology on the fracture behaviour under mixed mode loading. *Theoretical and Applied Mechanics Report*, No. 799, UILU-ENG-95-6021.

Hui CY, Zehinder AT (1993). A theory for the fracture of thin plates subjected to bending and twisting moments. *International Journal of Fracture*, 61, 211–229.

Irwin GR (1957). Analysis of stresses and strains near the end of a crack traversing a plate. *Journal of Applied Mechanics*, 24, 361–260.

K. L. West Conshohocken American Society for Testing and Materials (1999). ASTM STP 1359, Philadelphia, 41–57.

Karmat SV, Hirth JP (1994). A mixed mode fracture toughness correlation, *Scripta Metallurgica et Materialia*, 30, 145–148.

Karmat SV, Hirth JP (1996). Effect of aging on mixed-mode I/III fracture toughness of 2034 aluminium alloys. *Act Materialia*, 44 (3), 1047–1054.

Knauss W (1970). An observation of crack propagation in anti-plane shear. *International Journal of Fracture,* 6(2), 183–187.

Lan W, Deng X, Sutton MA, Cheng CS (2006). Study of slant fracture in ductile materials. *International Journal of Fracture*, 141, 469–496.

Li Y, Wierzbicki T, Sutton MA, Yan J, Deng X (2011). Mixed mode stable tearing of thin sheet Al 6061-T6 specimens: experimental measurements and finite element simulations using a modified Mohr-Coulomb fracture criterion. *International Journal of Fracture*, 168, 53–71.

Lui S, Chao YJ, Zhu X (2004). Tensile-shear Transition in mixed mode I/III fracture. *International Journal of Solids Structures,* 41, 6147–6172.

Macagno TM, Knott JF (1989). The fracture behaviour of PMMA in mixed modes I and II. *Engineering Fracture Mechanics*, 34, 65–86.

Macagno TM, Knott JF (1992). The mixed modes I/II fracture behaviour of lightly tempered HY130 steel at room temperature. *Engineering Fracture Mechanics*, 41, 805–820.

Mai YW, Cotterell B (1984). The Essential Work of Fracture of the Tearing of Ductile Sheet Materials. *International Journal of Fracture*, 24, 229–236.

Muscat-Fenech CM (1992). Tearing of Sheet Materials. Edition PhD. - Doctor of Philosphy in Engineering, Publisher Department of Engineering, University of Reading, U.K., BLDSC identification no.: DX 173965, University of Reading, reading, U.K.

Muscat-Fenech CM, Liu JH, Atkins AG (1992). The trousers tearing test with ductile metal sheets. *Journal of Materials Processing Technology*, 32(1–2), 301-315.

Muscat-Fenech CM, Atkins AG (1994a). Elastoplastic trouser tear testing of sheet materials. *International Journal of Fracture*, 67, 69–80.

Muscat-Fenech CM, Atkins AG (1994b). Elastoplastic convergent and divergent crack paths in tear testing of sheet materials. *Fatigue Fracture of Engineering Materials and Structures*, 17(2), 133–143.

Pan J, Shih CF (1992). Elastic – plastic analysis of combined I, II and III crack tip fields under small scale yielding conditions. *International Journal of Solids Structures,* 29 (22), 2795–2814.

Pook LP (1985). Comments on fatigue crack growth under mixed mode I and III and pure mode III loading. Multi-axial Fatigue. ASTM STP 853, in Miller, K.J., Brown, M.W., (Eds), *American Society for Testing and Materials*, Philadelphia, 259–263.

Pook LP, Sharples JK (1979). The mode III fracture crack growth threshold for mild steel, *International Journal of Fracture*, 15, R223–R226.

Rivlin RS, Thomas AG (1953). Rupture of rubber. I. Characteristic energy for tearing. *Journal of Polymer Science,* 10(3), 291–318

Royer J (1988). Study of pure mixed-mode fracture of a brittle material. *Experimental Mechanics*, 28, 382–387.

Sanford RJ (1979). A critical re-examination of the Westergaard method for solving opening mode crack problems. *Mechanics Research Communications*, 6, 289–294.

Shah RC (1974). Fracture under combined modes in 4340 steel. Fracture Analysis, *ASTM* STP 560, in*:* American society for testing and materials, 29–52.

Sih GC (1966). On Westergaard method of crack analysis. *International Journal of Fracture,* 2, 628 – 631.

Sih GC, Barthelemy BM (1980). Mixed mode fatigue crack growth predictions. *Engineering Fracture Mechanics*, 13, 439–451.

Sih GC, Cha BCK (1974). A fracture criterion for three-dimensional crack problems. *Engineering Fracture Mechanics*, 6, 699–723.

Sneddon N (1946). The distribution of stress in the neighbourhood of a crack in an elastic solid. *Proc. R. Soc. London. Ser. A* , A-187, 229–260.

Sommer E (1969). Formation of fracture 'lances' in glass. *Engineering Fracture Mechanics*, 1, 539–546.

Suresh S, Shih CF, Morrone A, O'Dowd NP (1990). Mixed-mode plane strain crack problems. *ASTM* STP 560, 187–210.

Suresh S, Tschegg EK (1987). Combined mode I – mode III fracture of fatigue – precracked alumina. *Journal of American Ceramic Society*, 70(10), 726–733.

Sutton MA, Helm JD, Boone ML (2001). Experimental study of crack growth in thin sheet 2024-T3 aluminium under tension-torsion loading. *International Journal of Fracture,* 109, 285–301.

Tian D, Lu D, Zhu J (1982). Crack propagation under combined stresses in three dimensional medium. *Engineering Fracture Mechanics*, 63, 5–17.

Wei Z, Deng X, Sutton MA, Yan JH, Cheng CS, Zavattieri P (2011). Modelling of mixed-mode crack growth in ductile thin sheets under combined in-plane and out-of plane loading. *Engineering Fracture Mechanics*, 78, 3082–3101.

Wei Z, Yan JH, Deng X, Sutton MA, Cheng CS (2005). Study of Mixed-Mode I/III Fracture in Ductile Materials. In Proceedings of the 2005 *SEM Annual conference and exposition on experimental and applied mechanics*, Portland, Oregon, June 7–9, 1651–1655.

Westergaard HM (1939). Bearing pressures and cracks. *Journal of Applied Mechanics,* 6, 49–53.

Williams JG, Ewing PD (1972). Fracture under complex stress–the angled crack problem. *International Journal of Fracture,* 8, 441–446.

Williams ML (1957). On the stress distribution at the base of a stationary crack. *Journal* of Applied *Mechanics,* 24, 109–114.

Yan JH, Sutton MA, Deng X, Cheng CS (2007). Mixed-mode fracture of ductile thin-sheet materials under combined in-plane and out-of-plane loading. *International Journal of Fracture,* 144, 297–321

Yan JH, Sutton MA, Deng X, Wei Z, Zavattieri P (2009). Mixed-mode crack growth in ductile thin sheet materials under combined in-plane and out-of-plane loading. *International Journal of Fracture,* 160, 169–188.

Yates JR, Miller KJ (1989). Mixed mode (I+III) fatigue thresholds in a forging steel. *Fatigue and Fracture Engineering Materials and Structures,* 12(3), 259–270.

Challenge Journal of Structural Mechanics

Transient resonance in limited power systems

Jerzy Michalczyk *, Grzegorz Cieplok

Department of Mechanics and Vibroacoustics, AGH University of Science and Technology, 30-059 Krakow, Poland

ABSTRACT

Difficulties in obtaining – by means of known methods - the proper estimation of maximum amplitudes in the transient resonance of technical systems, were indicated in the paper. It was proved that models of 1 degree of freedom cannot be used for such systems. The energy method of estimating maximum amplitudes in the transient resonance - useful also for systems of several degrees of freedom and multiple drives - was proposed. Taking into account interactions between the rotor and body motion of vibratory machines case the nomogram method for investigating resonance amplitude for coast-down phase was also presented.

ARTICLE INFO

Article history:
Received 26 July 2016
Accepted 13 September 2016

Keywords:
Transient resonance
Vibratory machines
Vibration
Nomogram method

1. Introduction

Phenomenon of a transient resonance occurs in vibratory systems subjected to quasi-harmonic excitations of a continuously variable frequency, containing the natural frequency range of the system. Technical systems, in which this effect occurs, are - among others - vibroinsulation systems of unbalanced rotor machines, unbalanced elastic rotors operating above critical frequencies, over-resonance vibratory machines such as screens, conveyers, foundry vibrating grids, vibrating tables for compacting and forming concrete elements, vibratory mills, etc.

The most often met technical systems, in which the transient resonance effect occurs during the start and coasting, can be generally reduced to the schemes shown in Fig. 1.

Due to the practical importance of the problem, it was the subject of several theoretical studies. The works were performed in various directions.

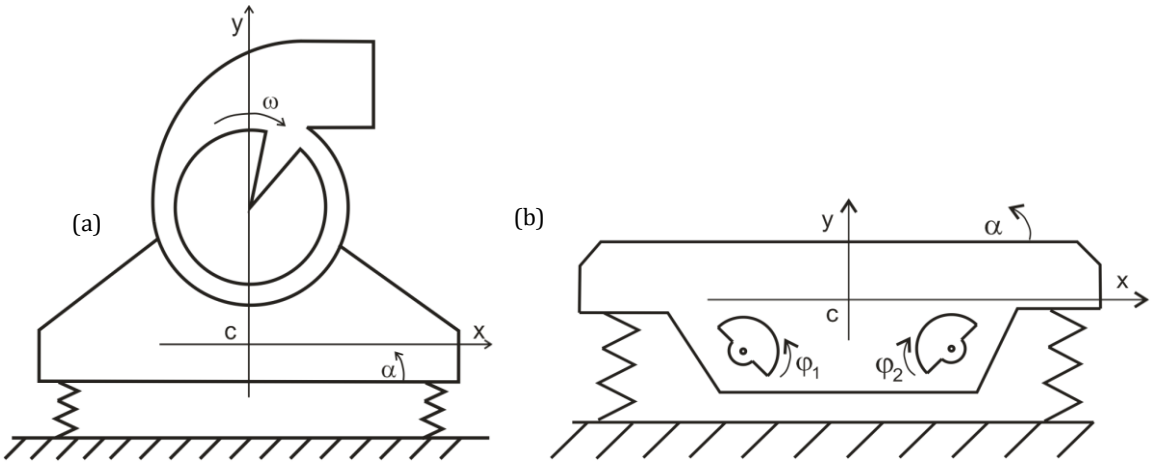

Fig. 1. Examples of technical systems, in which the transient resonance effect occurs:
a) Vibroinsulation system of an unbalanced rotor machine; b) Two-vibrator over-resonance vibratory machine.

* *Corresponding author*. Tel.: +48-12-6173673 ; Fax: +48-12-6339103 ; E-mail address: michalcz@agh.edu.pl (J. Michalczyk)
ISSN: 2149-8024 / DOI: http://dx.doi.org/10.20528/cjsmec.2016.09.020

2. Models with the Given Time-History of the Exciting Force

The first solutions were obtained for the system shown in Fig. 2(a), for which the calculation model presented in Fig. 2(b), was assumed in papers (Lewis, 1932; Kac, 1947; Markert and Seidler, 2001) and many others, (e.g. Dorning, 1959; Ferlund, 1963; Fearn and Milsaps, 1967; Hirano, 1968; Leul 1994; Cieplok, 2009a; 2009b).

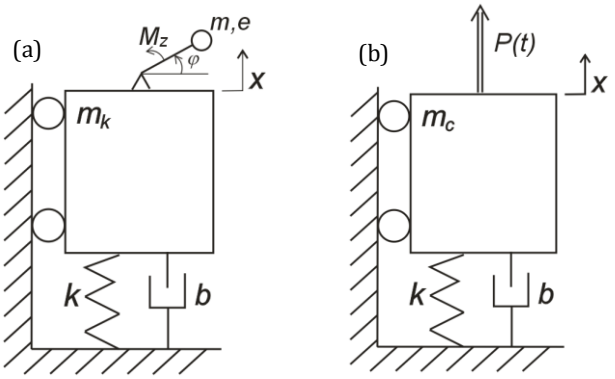

Fig. 2. Model of the vibroinsulation system of an unbalanced rotor machine of a linear vibration trajectory: a) Structural diagram; b) Calculation model.

Classic solutions of this problem and the majority of further attempts, were based on the simplified version of Eq. (1) of motion, assuming *a priori* the knowledge of the rotor angular velocity and its linear-variable over time form: $\dot{\varphi}(t) = \omega_0 \pm \varepsilon t$:

$$m_c\ddot{x} + b\dot{x} + kx = P\sin\left(\phi_0 + \omega_0 t \pm \frac{\varepsilon \cdot t^2}{2}\right), \tag{1}$$

where ε = const (+ for start-up, - for coasting).

In classic solutions described by Eq. (1) the component of the exciting force related to the rotor angular acceleration ε was neglected, since in the resonance zone it is usually much smaller than the centrifugal force.

In the first, historically speaking, solution of the transient resonance problem (Lewis, 1932), the independence of an excitation force P amplitude of a rotor angular velocity was assumed. The dependence of an excitation force amplitude on a rotor angular velocity square $P=me\omega^2$, being much closer to the reality, was introduced some years later by (Kac, 1947). In order to obtain the solution the impulse transfer function method was usually used, followed by numerical calculations of certain integrals.

Later formulations were rather similar (except for the paper of (Markert and Seidler, 2001), who wrote the transient resonance equation in a way allowing a slightly more general description of the excitation, e.g. taking into account the tangential component of an excitation force) and in a similar fashion, as the previous solutions, led to solutions in which the main component was:

$$A_{\max} \approx c\omega_n/\sqrt{\varepsilon}\,. \tag{2}$$

Solutions obtained by the analysis of the model shown in Fig. 2(b) were used for constructing nomograms (Harris, 1957), universally applied at present, for determinations of maximum amplitudes in the transient resonance.

The fundamental fault of all these elaborations is the fact, that the angular acceleration ε in the circum-resonant zone is unknown for the real systems. It cannot be determined on the basis of known driving and anti-torque moments of the rotor, since – in reality – the system being modelled (Fig. 2(a)) has two degrees of freedom and is described by the system of equations of motion:

$$m_c\ddot{x} + b\dot{x} + kx = \dot{\varphi}^2 me\sin\varphi - \ddot{\varphi}me\cos\varphi\,, \tag{3a}$$

$$J_{zr}\ddot{\varphi} = M_z - M_w\,, \tag{3b}$$

$$M_w = -\ddot{x}me\cos\varphi\,. \tag{3c}$$

Component M_w (Eq. 3c), called "the vibratory moment" (Blechman, 1971), appearing in the rotor equation of angular motion (Eq. 3b) and originated from the rotor axis vibrations (increasing in the resonance) has a decisive influence on this acceleration value. This component acts in principle as a strong braking torque and causes, that the real value of the angular acceleration at coasting is much higher than it would result from the resistance to motion alone (Fig. 3).

Thus the amplitude values, determined on the basis of nomograms (Harris, 1957), which were prepared on the grounds of the solution of Eq. (1), are several times too large for the coasting (Michalczyk, 1995) due to essential errors in ε evaluation.

3. Models Taking Into Account an Influence of Machine Vibrations on an Unbalanced Rotor Running

Some of the works taking into account the influence of the vibratory moment are based on the system energy balance directly before the resonance and in the moment when maximum vibrations occur, obtaining estimations "from the top" of the maximum amplitudes. Thus, e.g. in paper (Michalczyk, 1993), the kinetic energy of the set of vibrators in the moment of entering the resonance zone of the i^{th} form of vibrations was equated to the machine vibration energy, performing movement in accordance with this form of vibrations, at the assumption that the main vibrations occur in a plane motion along one coordinate.

This problem will be now formulated in a more general way than in the quoted paper, by allowing the resonance vibrations corresponding to the arbitrary form of natural vibrations in the general motion of the linearised system surrounding the balance point.

The energy balance for the i^{th} resonance of the machine with n drives will be written as:

$$n \cdot \tfrac{1}{2}J_{zr}\omega_{0i}^2 = \tfrac{1}{2}\dot{\mathbf{q}}_{\max i}^T \cdot \mathbf{M} \cdot \dot{\mathbf{q}}_{\max i}\,, \tag{4}$$

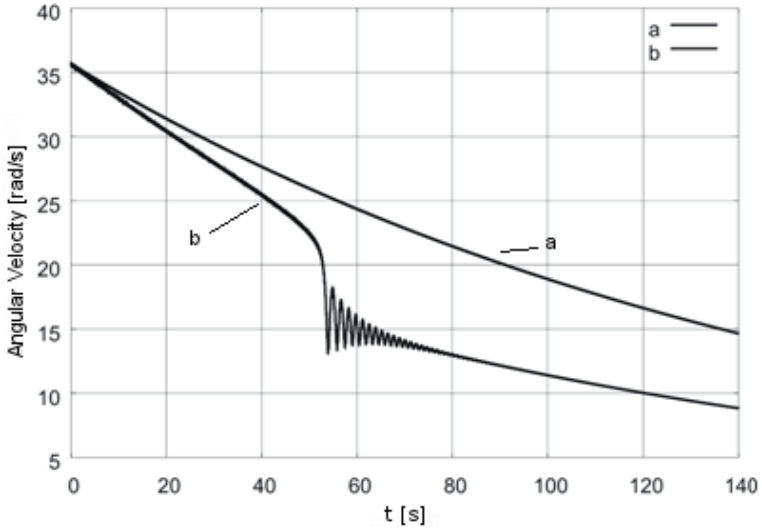

Fig. 3. Influence of the vibratory moment on the rotor angular velocity ω during the vibrator free coasting (M_z<0):
a) Coasting without taking into account the vibratory moment;
b) Coasting with taking into account the vibratory moment M_w.

where ω_{0i} is angular velocity, at which the energy exchange occurs (usually not much different from the i^{th} natural frequency of the machine body on the elastic suspension system), $\mathbf{q} = \text{col}\{x_c, y_c, z_c, \varphi_x, \varphi_y, \varphi_z\}$ – coordinates vector in the central coordinate system, describing small body vibrations versus the static balance point, J_{zr} – reduced moment of inertia of the vibrator and drive, J_{ij} – elements of the tensor of inertia – correspondingly - in the central system Cxyz, $m_c = m_k + n \cdot m$,

$$\mathbf{M} = \begin{bmatrix} m_c & 0 & 0 & 0 & 0 & 0 \\ & m_c & 0 & 0 & 0 & 0 \\ & & m_c & 0 & 0 & 0 \\ & & & J_{xx} & -J_{xy} & -J_{xz} \\ & sym. & & & J_{yy} & -J_{yz} \\ & & & & & J_{zz} \end{bmatrix}. \tag{5}$$

Maximum values of the generalised velocities $\dot{\mathbf{q}}_{\max i}$, for harmonic vibrations of ω_{0i} frequency, are related to the maximum amplitude values of the displacement vector by the dependence: $\dot{\mathbf{q}}_{\max i} = \omega_{0i} \cdot \mathbf{q}_{\max i}$, which leads to the Eq. (6):

$$n \cdot \frac{1}{2} J_{zr} \omega_{0i}^2 = \frac{1}{2} \omega_{0i}^2 \cdot \mathbf{q}_{\max i}^{\mathrm{T}} \cdot \mathbf{M} \cdot \mathbf{q}_{\max i}\,, \tag{6}$$

or, after the reduction:

$$n \cdot J_{zr} = \mathbf{q}_{\max i}^{\mathrm{T}} \cdot \mathbf{M} \cdot \mathbf{q}_{\max i}\,. \tag{6a}$$

Let the vibrating motion of the machine body placed on the elastic suspension system be described by the equation of small natural undamped vibrations:

$$\mathbf{M} \cdot \ddot{\mathbf{q}} + \mathbf{K} \cdot \mathbf{q} = 0\,, \tag{7}$$

where **K** is symmetric elasticity matrix.

For the basic – in applications - case of the machine placed on a system j=1,..,ν of parallel, identical elastic elements of constants:
- in a vertical direction, k_z,
- in horizontal directions, k_x, $k_y = k_{xy}$

and coordinates x_j, y_j, z_j of points - where the elastic elements were mounted to the body in the static equilibrium of the machine - it is easy to prove the following:

$$\mathbf{K} = \begin{bmatrix} \nu k_{xy} & 0 & 0 & 0 & k_{xy}\Sigma z_j & -k_{xy}\Sigma y_j \\ & \nu k_{xy} & 0 & -k_{xy}\Sigma z_j & 0 & k_{xy}\Sigma z_j \\ & & \nu k_{xy} & k_z \Sigma y_j & -k_z \Sigma x_j & 0 \\ & & & k_z \Sigma x_j^2 + k_{xy}\Sigma z_j^2 & -k_z \Sigma x_j y_i & -k_{xy}\Sigma x_j z_j \\ & sym. & & & k_z \Sigma x_j^2 + k_{xy}\Sigma z_j^2 & -k_{xy}\Sigma y_j z_j \\ & & & & & k_{xy}\left(\Sigma x_j^2 + \Sigma y_j^2\right) \end{bmatrix}. \tag{8}$$

For the harmonic form of solutions $\mathbf{q} = \mathbf{q}_{\max} (\sin \omega t + \gamma)$ it leads to the matrix frequency equation:

$$[\mathbf{K} - \omega^2 \mathbf{M}] = 0\,, \tag{9}$$

which allows to determine the set of natural frequencies ω_{0i}, i=1...6 and modal vectors:

$$\mathbf{\Psi}_i(\omega_i) = \text{col}\{\psi_{1i}, \psi_{2i}, \psi_{3i}, \psi_{4i}, \psi_{5i}, \psi_{6i}\}\,. \tag{10}$$

Let it be assumed for the moment, that these frequencies are different and satisfactorily distant. This allows to present the amplitude vector for vibration of the i^{th} frequency and form, as:

$$\mathbf{q}_{\max i} = \text{col}\left\{\frac{\psi_{1i}}{\psi_{ki}} \cdot q_{\max ki}, \frac{\psi_{2i}}{\psi_{ki}} \cdot q_{\max ki}, , q_{\max ki}, , \frac{\psi_{6i}}{\psi_{ki}} \cdot q_{\max ki}\right\}$$

$$= \mathbf{q}_{\max ki}\, \text{col}\left\{\frac{\psi_{1i}}{\psi_{ki}}, \frac{\psi_{2i}}{\psi_{ki}}, , 1, , \frac{\psi_{6i}}{\psi_{ki}}\right\}, \tag{11}$$

where $\mathbf{q}_{\max ki}$ means the maximum amplitude of the arbitrarily selected coordinate q_k (to represent vibrations of the i^{th} form, at the assumption: $\psi_{ki} \neq 0$). Denoting:

$$\operatorname{col}\left\{\frac{\psi_{1i}}{\psi_{ki}}, \frac{\psi_{2i}}{\psi_{ki}} \cdot, , 1, , \frac{\psi_{6i}}{\psi_{ki}}\right\} = \mathbf{a}_{ki}\,, \tag{12}$$

and substituting to Eq. (11) and Eq. (6a) the final formula for the maximum amplitude of the k^{th} coordinate during the system passage through the resonance with the i^{th} frequency of natural vibrations will be obtained:

$$\mathbf{q}_{\max ki} = \sqrt{\frac{n \cdot J_{zr}}{\mathbf{a}_{ki}^{\mathrm{T}} \cdot \mathbf{M} \cdot \mathbf{a}_{ki}}}\,. \tag{13}$$

This formula constitutes an over-estimation (usually close to the real values) of the maximum amplitude of the selected k^{th} coordinate in the i^{th} resonance, provided that the vibrator excitation force performs work at vibrations of the investigated form. This requirement is equivalent to the demand of not zeroing the respective modal force. Not satisfying this condition as a rule means that the passage through the resonance zone will be without the excitation of more intensive machine vibrations. Deviations from this rule can occur in two-vibrator system acting due to the self-synchronization principle, see (Michalczyk and Czubak, 2010).

In the case when in the spectrum of the system natural frequencies multiple frequencies occur, this procedure is usually not possible in respect of those frequencies, due to the ambiguity of the vibration form. An exception constitute symmetric systems for which forms of vibration are known, e.g. from the physical analysis of the problem (as for the machines shown in Fig. 4). An example of using this method in relation to real machines was shown in (Michalczyk, 2012a) with respect to lumped parameter systems and in (Michalczyk, 2012b) for distributed-parameter systems.

The energy balance was also applied in paper (Agranowskaja and Blechman, 1969), however, the vibrator kinetic energy was not equated to the body kinetic energy, but to the maximum potential energy of the suspension system. The difficulty of this energy method constitutes the necessity of estimation the vibrator angular velocity, at which the energy exchange occurs, while this velocity does not comply directly with the system natural vibrations frequency (Lewis, 1932) and the method does not provide the way of its determination.

4. Nomogram Method

The phenomenological model of a vibratory machine illustrated schematically in Fig. 4 is considered. A machine body, having a mass M is suspended in a flexible viscous system described by concentrated constants k and b. The system is excited to vibrations by the inertia vibrator characterized by the static unbalance me value. The vibrator moment of inertia combined with the driving system moment of inertia is reduced to the coordinate of the vibrator rotation and denoted by J_{zr}. The vibrator is exposed to the driving moment action M_{el}.

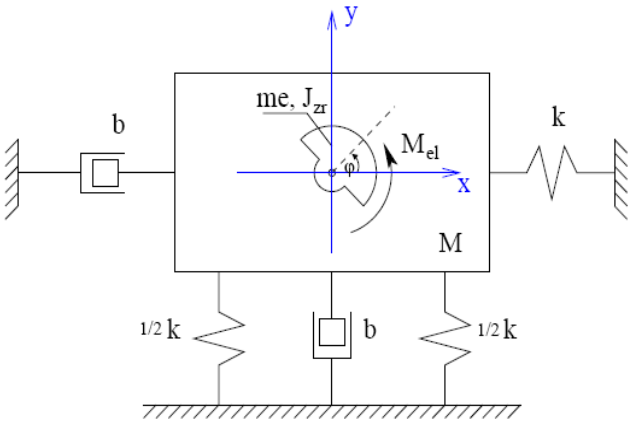

Fig. 4. Vibratory machine model.

Taking into consideration three degrees of freedom (x_s, y_s, φ) the machine equations of motion can be shown in the form of Eqs. (14) (15) and (16).

$$\begin{bmatrix} m_c & 0 \\ 0 & m_c \end{bmatrix}\begin{bmatrix} \ddot{x}_s \\ \ddot{y}_s \end{bmatrix} + \begin{bmatrix} b & 0 \\ 0 & b \end{bmatrix}\begin{bmatrix} \dot{x}_s \\ \dot{y}_s \end{bmatrix} + \begin{bmatrix} k & 0 \\ 0 & k \end{bmatrix}\begin{bmatrix} x_s \\ y_s \end{bmatrix} = \begin{bmatrix} P_x \\ P_y \end{bmatrix}, \tag{14}$$

$$\begin{bmatrix} P_x \\ P_y \end{bmatrix} = \begin{bmatrix} me \sin\varphi \\ -me \sin\varphi \end{bmatrix}\ddot{\varphi} + \begin{bmatrix} me \cos\varphi \\ me \sin\varphi \end{bmatrix}\dot{\varphi}^2\,, \tag{15}$$

$$J_{zr}\ddot{\varphi} - me(\ddot{x}\sin\varphi - \ddot{y}\cos\varphi) = M_{el}\,. \tag{16}$$

Upon transformation to the rotating with the angular velocity of the vibrator system $0\xi\eta$ (Fig. 5), these equations can take the form of Eq. (17):

$$\begin{bmatrix} m_c & 0 & m_c\eta & 0 & 0 \\ 0 & m_c & m_c\xi + me & 0 & 0 \\ 0 & me & me\xi + J_{zr} & 0 & 0 \\ 0 & 0 & 0 & 1 & 0 \\ 0 & 0 & 0 & 0 & 1 \end{bmatrix}\frac{d}{dt}\begin{bmatrix} v_\xi \\ v_n \\ \omega \\ \xi \\ \eta \end{bmatrix} =$$

$$\begin{bmatrix} 2m_c\omega v_\eta - bv_\xi - (k - \omega^2 m_c)\xi + b\omega\eta + me\omega^2 \\ -2m_c\omega v_\xi - bv_\eta - (k - \omega^2 m_c)\eta - bv\omega^2 \\ -2mev_\xi\omega + me\eta\omega^2 + M_{el} \\ v_\xi \\ v_\eta \end{bmatrix}, \tag{17}$$

where:

$$m_c = M + m\,. \tag{18}$$

This transformation enables also to create a definition of relative units and parameters for the machine. Hence substituting by the following:

$$\underline{\xi} = \frac{\xi}{A_u},\ \underline{\eta} = \frac{\eta}{A_u},\ \underline{\omega} = \frac{\omega}{\omega_0},\ \sigma = \frac{m^2e^2}{m_c J_{zr}},$$

$$q = \frac{M_{el}}{J_{zr}}\frac{1}{\omega_0^2}\,,\ \gamma = \frac{b}{2\sqrt{m_c k}}\,,\quad \tau = \frac{\omega_0}{2\pi}t\,,\ A_u = \frac{me}{m_c}. \tag{19}$$

The matrix Eq. (17) may be expressed in the following form:

$$\begin{bmatrix} \frac{1}{4\pi^2} & 0 & -\frac{1}{2\pi}\eta & 0 & 0 \\ 0 & \frac{1}{4\pi^2} & \frac{1}{2\pi}(1+\xi) & 0 & 0 \\ 0 & \frac{\sigma}{4\pi^2} & \frac{1}{2\pi}(\sigma\xi+1) & 0 & 0 \\ 0 & 0 & 0 & 1 & 0 \\ 0 & 0 & 0 & 0 & 1 \end{bmatrix} \frac{d}{d\tau} \begin{bmatrix} \underline{v_\xi} \\ \underline{v_\eta} \\ \underline{\omega} \\ \underline{\xi} \\ \underline{\eta} \end{bmatrix} =$$

$$\begin{bmatrix} \underline{\omega}^2 - (1-\underline{\omega}^2)\underline{\xi} - \frac{\gamma}{\pi}\underline{v_\xi} + \frac{1}{\pi}\underline{\omega}\,\underline{v_\eta} + 2\gamma\underline{\omega}\,\underline{\xi} \\ -(1-\underline{\omega}^2)\underline{\eta} - \frac{\gamma}{\pi}\underline{v_\eta} + \frac{1}{\pi}\underline{\omega}\,\underline{v_\xi} + 2\gamma\underline{\omega}\,\underline{\xi} \\ -\frac{\sigma}{\pi}\underline{v_\xi}\underline{\omega} + \sigma\underline{\eta}\omega^2 + q \\ \underline{v_\xi} \\ \underline{v_\eta} \end{bmatrix}. \quad (20)$$

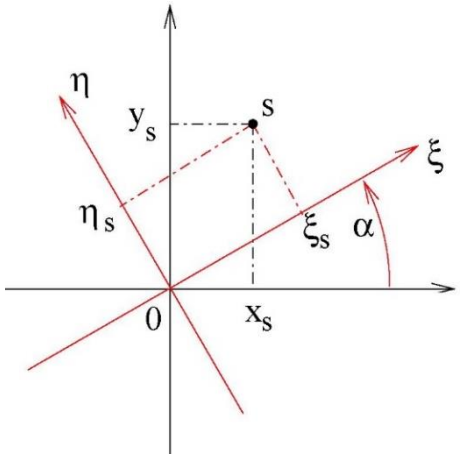

Fig. 5. Position of the machine body mass centre in the stationary coordinate systems 0*xy* and rotating system 0$\xi\eta$.

Due to an application of relative parameters the set of six physical parameters m_c, me, J_{zr}, M_{el}, k, b - needed to determinate the machine dynamics in the natural coordinate system - was reduced to three parameters σ, γ, q. Based on the system above (Eq. (20)), it is possible to develop the nomogram (Fig. 6) that enables to determine the amplitude multiplication factor α for the coast-down phase based on values of parameters σ, γ. For the free coasting the parameter q is assumed to be zero.

In the case when during a coast-down phase external moments of friction play an important role, it is possible to use the contour map presented in Fig. 7. The map was prepared for parameter γ=0.01, which can represent suspensions built of steel material properties. The friction is expressed by the relative parameter q.

The data map can be approximated by the function of the following form:

$$\alpha = (a_2 - a_3 \ln\sigma)e^{-a_1 q} + a_4\,. \quad (21)$$

where:

for	for
$\sigma \in (0.0003, 0.03)$	$\sigma \in (0.0003, 0.03)$
$q \in (0.001, 0.049)$	$q \in (0.05, 1.2)$
$a_1 = 49.51$	$a_1 = 6.75$
$a_2 = -9.51$	$a_2 = 2.57$
$a_3 = 2.68$	$a_3 = 0.31$
$a_4 = 4.42$	$a_4 = 1.33$

(22)

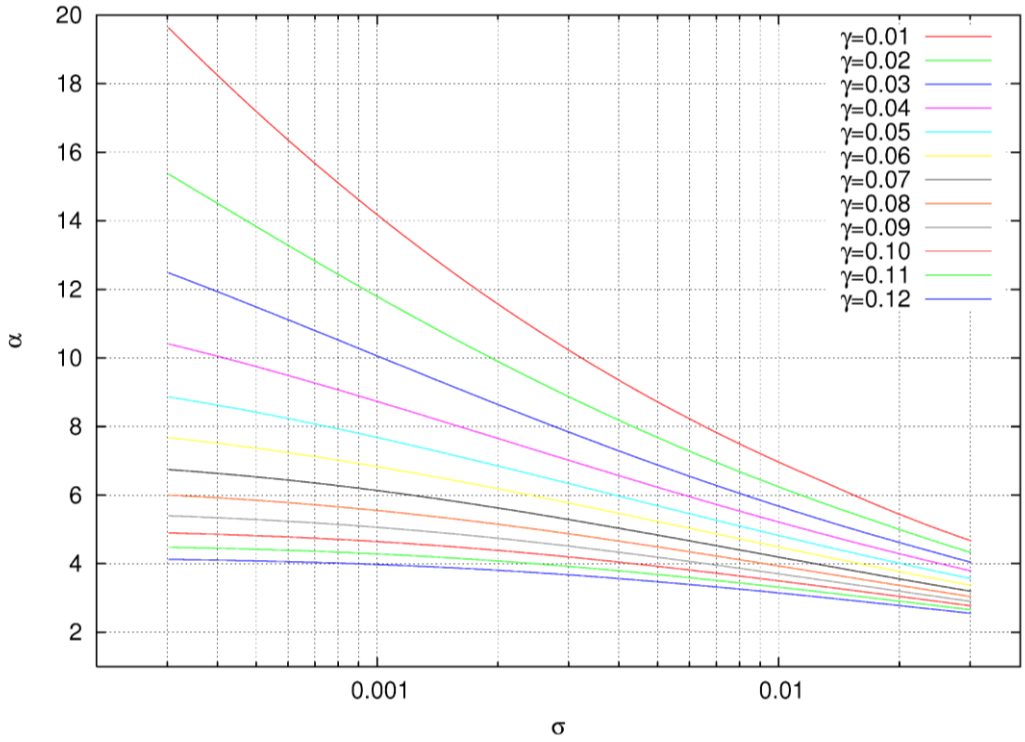

Fig. 6. Machine body vibration amplitude multiplication factor $\alpha = \frac{A_{of\ \text{resonanse}}}{A_u}$ for the coast-down phase.

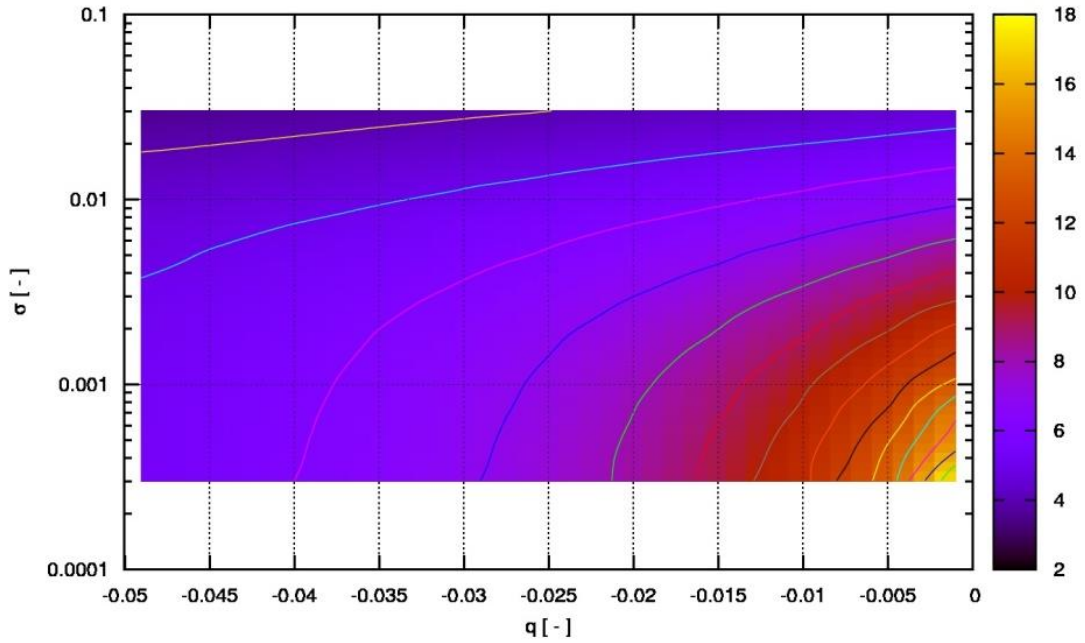

Fig. 7. Amplitude multiplication factor α taking into account friction during the coast-down phase.

5. Conclusions

The problem of the determination of the maximum amplitudes in the transient resonance during the free coasting of vibratory machines and vibroinsulating systems of rotor machines was analysed in the study. It was proved that the classic methods, based on the assumption that the time-history of the unbalanced rotor motion is known, lead to serious errors.

The reason of these errors constitutes a strong influence of the machine body vibrations on the rotor running in the resonance zone. Two methods of assessments the maximum amplitudes, in this case, were formulated:

- Method of the kinetic energy balance in the system,
- Nomogram method.

The first method has a wider range of applications encompassing general motions of elastically supported bodies and vibrations of continuous systems, while the second one is characterised by a higher accuracy and a possibility of taking into account the dissipation in the system as well as driving and anti-torque moments however, its application is limited to translatory motion of machine bodies.

References

Agranowskaja E, Blechman II (1971). Ob ocenkie rezonansnych amplitud kolebanii pri vybiegie systemy so mnogimi stepieniami svobody. *Dinamika Maszyn*, Nauka, Moscow (in Russian).

Blechman II (1971). Synchronizacja Dynamiczeskich System. Nauka, Moscow (in Russian).

Cieplok G (2009a). Stany Nieustalone Nadrezonansowych Maszyn Wibracyjnych. UWND AGH, Kraków (in Polish).

Cieplok G (2009b). Verification of the nomogram for amplitude determination of resonance vibrations in the run-down phase of a vibratory machine. *Journal of the Theoretical and Applied Mechanics, Warsaw*, 47(2), 295–306.

Harris C (1957) Handbook of Noise Control. McGraw-Hill Book Co., New York.

Kac AM (1947). Wynuzdionnyje kolebanija pri prochozdienii czerez riezonans. *Inżyniernyj Sbornik vyp*. 2/1947 t3 (in Russian).

Lewis F (1932). Vibration during acceleration through a critical speed. *Transactions of the American Society of Mechanical Engineers*, 54, 253-261.

Market R, Seidler M (2001). Analytically based estimation of the maximum amplitude during passage through resonance. *International Journal of Solids and Structures*, 38(10-13), 1975-1992.

Michalczyk J (1993). Reduction of vibrations during transient resonance of vibratory machines. *NOISE-93*, St. Petersburg, Russia.

Michalczyk J (1995). Maszyny Wibracyjne: Obliczenia Dynamiczne, Drgania, Hałas. WNT, Warszawa (in Polish).

Michalczyk J (2012a). Transient resonance of machines and devices in general motion. *Journal of Theoretical and Applied Mechanics*, 50(2), 577-587.

Michalczyk J (2012b). Maximum amplitudes in transient resonance of distributed-parameter system. *Archives of Mining Sciences*, 57(3), 657-665.

Michalczyk J, Czubak P (2010). Methods of determination of maximum amplitudes in the transient resonance of vibratory machines. *Archives of Metallurgy and Materials*, 55(3), 695-705.

Challenge Journal of Structural Mechanics

The influence of different concrete classes on the seismic response of a seismically isolated building

Savaş Erdem [a,*], Khalid Saifullah [a], Ezgi Gürbüz [a], Marva Angela Blankson [b]

[a] *Department of Civil Engineering, İstanbul University, 34320 Istanbul, Turkey*
[b] *School of Engineering, University of Technology Jamaica, Kingston 6, Jamaica*

ABSTRACT

In this study, an eight story seismically isolated building representing a mid-rise type building was employed to investigate the effect of usage of different concrete classes (C20, C25, C30, C40, and C50) on the seismic response of a seismically isolated building. The prototype fixed base buildings were converted to seismically isolated buildings by introducing rubber isolators at base level. Analyses were conducted by using two different isolation systems (QW5Tb3 and QW10Tb3).The modelling of conventional fixed base prototype seismically isolated buildings and their modal analyses were conducted on finite-element program SAP2000, whereas, modelling of seismically isolated buildings and nonlinear time-history analyses were conducted using 3D-BASIS program. Floor accelerations, Story shears and inter-story drift ratios were the key structural responses considered. The analysis results showed concrete strength have significant effects on the seismic behaviour of the structures. Seismically isolated buildings with isolation system having 5% characteristic strength, C40 and C50 concrete buildings showed less first floor accelerations as compared to the lower concrete class buildings. In addition, isolated buildings with C40 and C50 concrete showed much more inter-story drift ratio values at each floor level as compared to isolated buildings with C20, C25 and C30 concrete which showed values very close to one another.

ARTICLE INFO

Article history:
Received 14 August 2016
Accepted 16 September 2016

Keywords:
Concrete class
Seismic response
Seismic isolation
Reinforced concrete buildings

1. Introduction

Reinforced concrete structures make up most of the existing structure stock in the world because of their high rigidity, long service life and high resistance to earthquake damage. Analysis of these structures for different levels of earthquake intensity and for determination of damage levels is a matter of high priority in earthquake prone areas (Erdem, 2016). Many studies have been conducted on the dynamic behaviour and seismic vulnerability of reinforced concrete structures (Verderame et al., 2010; Rojman and Fajfar, 2009; Golghate et al., 2013; Peruš et al., 2013).

One of the important factor that affects evaluation of the seismic performance of existing building is the concrete compressive strength (Pereira and Romao, 2016a; 2016b). In the literature review, a number of research studies have been performed for investigating the influence of concrete strength on the structural performance. A recent work by Coskan et al. (2015) demonstrated performance limits, structural stiffness, deformation quantities, ultimate bearing capacity and plastic hinge processed are strongly affected by the concrete strength. In another study, Bayraktar et al. (2014) investigated 90 reinforced concrete buildings that were collapsed during 2011 Van Earthquake to determine the overall structural performance of the building. It was found that 47 % of the buildings have an average compressive strength between 8 and 12 MPa, 26% of the buildings have an average compressive strengths between 4 and 8 MPa, and 20 % of the buildings have average compressive strengths between 12 and 16 MPa. In parallel, Erberik (2008) and Kocak (2005) have made similar observations on the influence of concrete strength quality on the earthquake

* *Corresponding author*. Tel.: +90-212-4737070 ; Fax: +90-212-4737180 ; E-mail address: savas.erdem@istanbul.edu.tr (S. Erdem)
ISSN: 2149-8024 / DOI: http://dx.doi.org/10.20528/cjsmec.2016.09.022

performance after Duzce Earthquake (1999) and Marmara Earthquake (1999), respectively. The results showed that the poor compressive strength adversely affected the overall structural behaviour.

Reinforced concrete structures in many civil engineering applications can often be subjected to short duration dynamic loadings generated from earthquakes. Under such circumstance, it is obvious that structures with high ductility is much more desirable. It has been observed from previous research (Hwang and Hsu, 2000; Madden et al., 2002; Pant and Wijeyewickrema, 2012) that ideally, base-isolation is an effective technique to improve the seismic performance of buildings. Although base isolation decreases the possibility of damage (less inter-story drifts, shear forces and floor accelerations) of a building, it causes to large displacements in the structure relative to the ground. This, in turn, increases the potential of impact or pounding of a building with adjacent structures (Pant and Wijeyewickrema, 2012).

A review of the literature indicates that in contrast to seismic behaviour of seismically isolated reinforced concrete buildings, no study has been conducted so far to investigate the effect of usage of different concrete classes on the seismic response of a seismically isolated building. In this study, an eight story seismically isolated building representing a mid-rise type building was employed to investigate the effect of usage of different concrete classes (C20, C25, C30, C40, and C50) on the seismic response of a seismically isolated building. Analyses were conducted by using two different isolation systems (QW5Tb3 and QW10Tb3). Floor accelerations, story shears and inter-story drift ratios were the key structural responses considered.

2. Methodology

In this study, an eight story seismically isolated building representing a mid-rise type building was employed to investigate the effect of usage of different concrete classes on the seismic response of a seismically isolated building. The prototype building makes use of a moment resisting frame structural system. The building was symmetric in plan with dimensions of 25m x 25m and consists of 5 bays in both *X* and *Y* principal directions. The typical story height was 3m. It was assumed that the building importance factor was 1, and that the soil type according to UBC 97 was Class C. Regarding loading on the buildings, story masses were usually used which are lumped at centre of gravity (at master joint). A translational mass of 500 kNs^2/m was assumed to be lumped at the centre of mass of each floor. Typical floor plan and 3D view of the building in question are shown in Figs. 1 and 2, respectively. *X*-sectional dimensions of column and beam elements of the building changes with the concrete class used. Figure of frame sections of 8 story building using C20 concrete is shown Fig. 3. There was not a drastic or considerable variation of sizes as concrete compressive strength increases. For example, the size of square columns with C50 concrete was 52 cm while with C20 it was 60 cm. In proportioning of the load bearing structural elements i.e. beams and columns according to concrete class employed, important points of the building codes like strong column - weak beam concept and shear capacity at beam-column connection region were taken into account. The prototype fixed base buildings were converted to seismically isolated buildings by introducing rubber isolators at base level (also called base isolation).

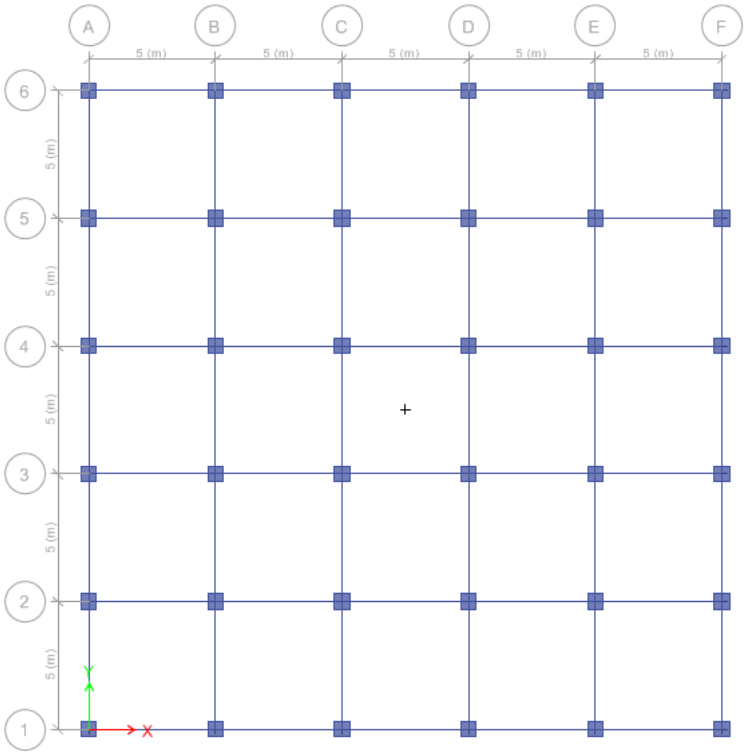

Fig. 1. Typical floor plan of prototype 8 story building.

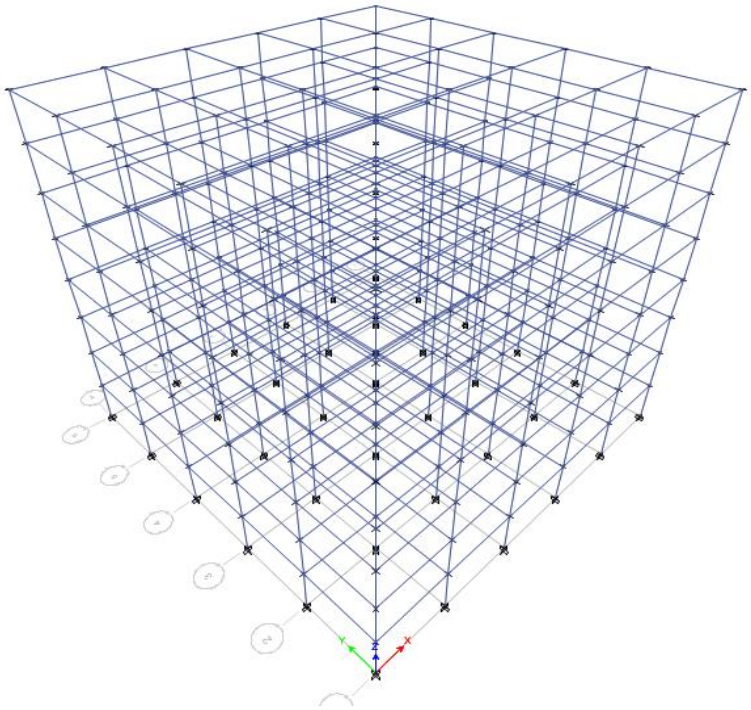

Fig. 2. 3D view of prototype 8 story building.

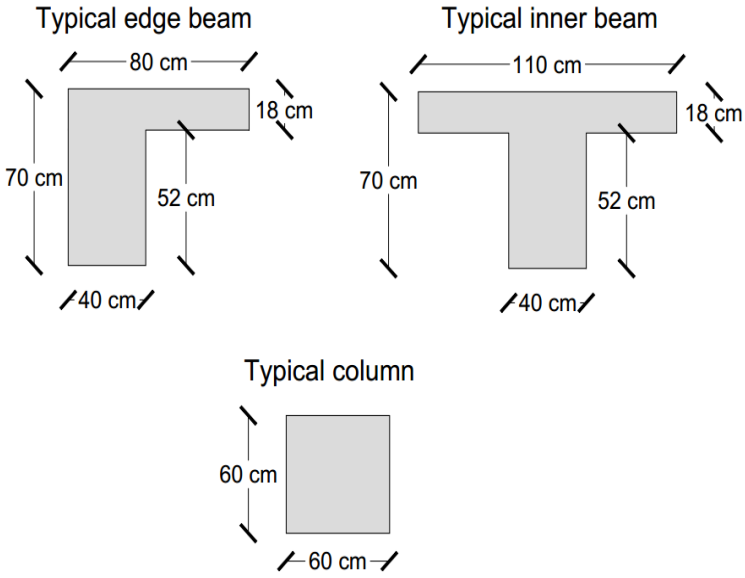

Fig. 3. Details of the frame section of the building with C20.

The modelling of conventional fixed base prototype seismically isolated buildings and their modal analyses were conducted on finite-element program SAP2000, whereas, modelling of seismically isolated buildings and nonlinear time-history analyses were conducted using 3D-BASIS program which has been particularly developed, by Nagarajaiah et al. (1991), for nonlinear dynamic analysis of three dimensional base isolated structures. The fundamental/first mode periods of 8 story fixed base buildings with different concrete classes were obtained through modal analyses and are presented in Table 1. As compressive strength increased modulus of elasticity increased but size of frame section (especially columns) decreased resulting in less moment of inertia. The increase in elasticity modulus was not so significant as compared to the decrease in section sizes resulting in decrease in stiffness and in turn resulting in increase in period. In addition to, the values of spectral acceleration (SA) was small (in the range of 0.01 -0.02 g) as the period of the buildings was about 3 s. A ground motion record from 1994 Northridge earthquake was used for nonlinear time-history analyses and was taken from NGA database which is an updated version of PEER's strong ground motion database. Analyses were done by using bidirectional earthquake input with strong component of earthquake along one main axis (*X*-axis) and weak component of earthquake along other orthogonal main axis (*Y*-axis) of the buildings.

The acceleration time history and spectrum record for acceleration used in the analysis are shown in Fig. 4. It should not be forgotten that the spectrum shows the responses of a single degree freedom system. As the building was a multi degree of freedom system, the response will vary.

Table 1. Fundamental/First mode period of prototype fixed base building.

Concrete Class	Period (s)	SA (g)
C20	0.521	0.33
C25	0.573	0.29
C30	0.638	0.24
C40	0.729	0.19
C50	0.843	0.13

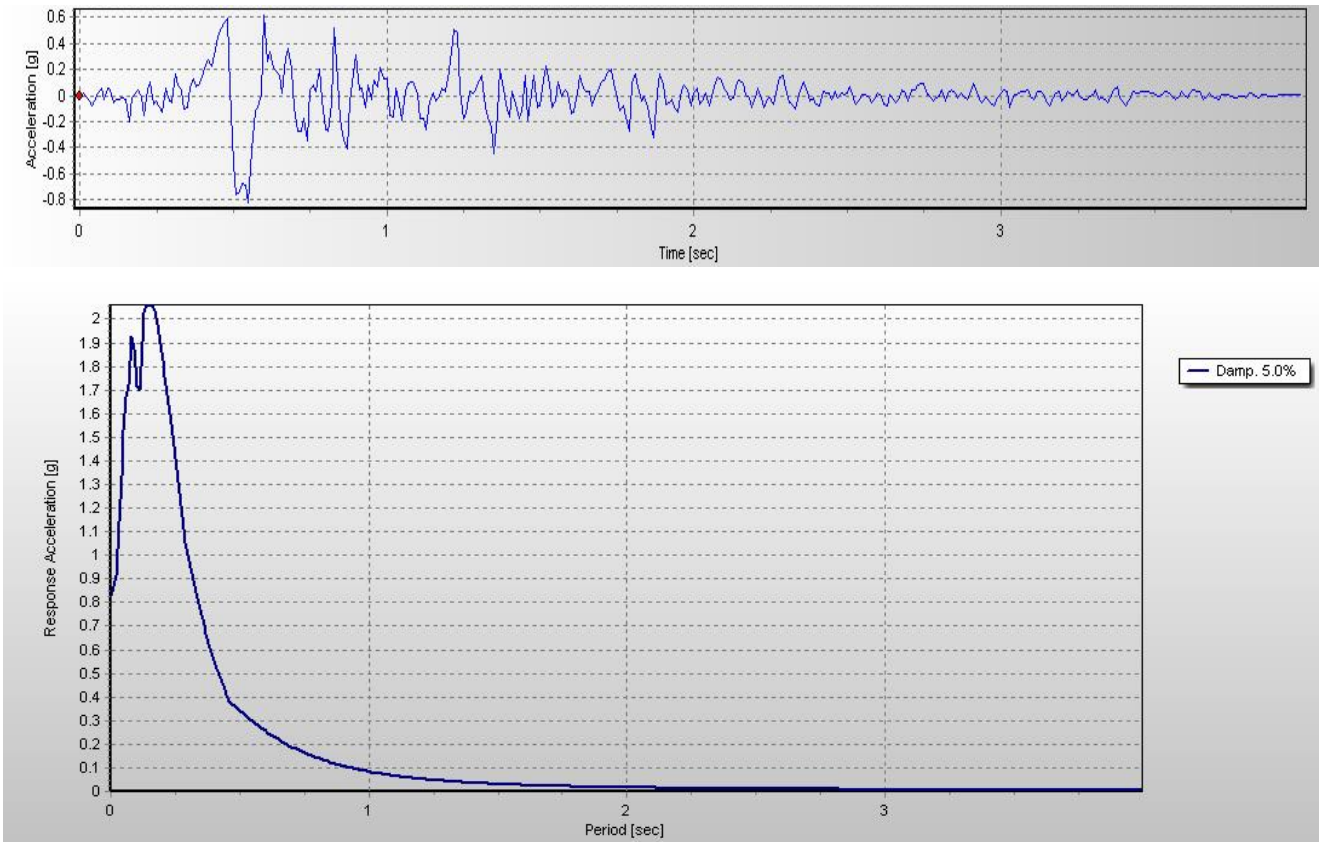

Fig. 4. Acceleration time history and spectral acceleration used.

A translational mass of 500 kNs^2/m was assumed to be lumped at the centre of mass of each floor. Each floor had 3 degrees of freedom i.e. 2 translations and 1 rotation. Rigid diaphragm was introduced at each floor level to distribute the lateral forces to structural elements of the frame. Analyses were realized by using two different isolation systems (QW5Tb3 and QW10Tb3). Here, in QW5Tb3 isolation system QW5 indicates characteristic strength of isolation system normalized with weight of the building (W) to be 5% and Tb3 indicates isolation period to be 3 seconds. It is worth-mentioning that characteristic strength of the isolation system is a measure of level of damping in the isolation system. The parameters concerning isolation systems were summarized in Table 2. To calculate parameters for each isolator, Q (characteristic strength), $K1$ (pre-yield stiffness), $K2$ (post-yield stiffness), and Fy (Yield force) should be divided by total number of isolators used in the isolation system. In Table 2, α is post-yield to pre-yield stiffness ratio and Dy is yield displacement of isolation system. A constant value of 0.015 m was adopted for both the isolation systems.

3. Results and Discussion

As the seismically isolated buildings in this study are subjected to bi-directional earthquake excitations, the structural responses in both global X and Y direction have been considered for performance comparison. It is important to mention that the building models used in this study are symmetrical so the results obtained would

be same if the axes are reversed. Moreover, the displacements at the isolation level or the base displacements obtained from the analyses of all the building models with similar isolation parameters are almost same so the main focus of attention for this study is the superstructure responses. Floor accelerations, Story shears and inter-story drift ratios are the key structural responses considered.

Table 2. Parameters related to modelling of nonlinear isolation system.

Isolation System	*Tb* (s)	*Q*/*W* (%)	*Q* (kN)	*K2* (kN/m)	*K1*(kN/m)	*α* (*K2*/*K1*)	*Dy* (m)	*Fy* (kN)
QW5Tb3	3	5	2207.3	19739.209	166889.2	0.118	0.015	2503.34
QW10Tb3	3	10	4414.5	19739.209	314039.2	0.063	0.015	4710.59

3.1. Floor accelerations

Floor accelerations in global X-direction or X-axis of the buildings, with characteristic strength level of 5% for the isolation system, are shown in Fig. 5. It was evident that as it was moved from the base towards the top floor, no particular increasing or decreasing trend (either linear or nonlinear) was observed for any concrete class. However, it was seen that variation in accelerations become more pronounced as the increased compressive strength of the concrete i.e. the building with concrete class C20 showed less variation in accelerations as it was moved from the base towards the top floor as compared to the building with concrete class C50 which showed significant changes in acceleration at each floor level. The top floor acceleration was more or less same in all the buildings. On the other hand, first floor accelerations with the buildings having C20, C25 and C30 concrete were almost same but the buildings employing C40 and C50 concrete class showed less first floor accelerations as compared to the aforementioned buildings. Moreover, in all cases top floor accelerations were more than the first floor accelerations as expected.

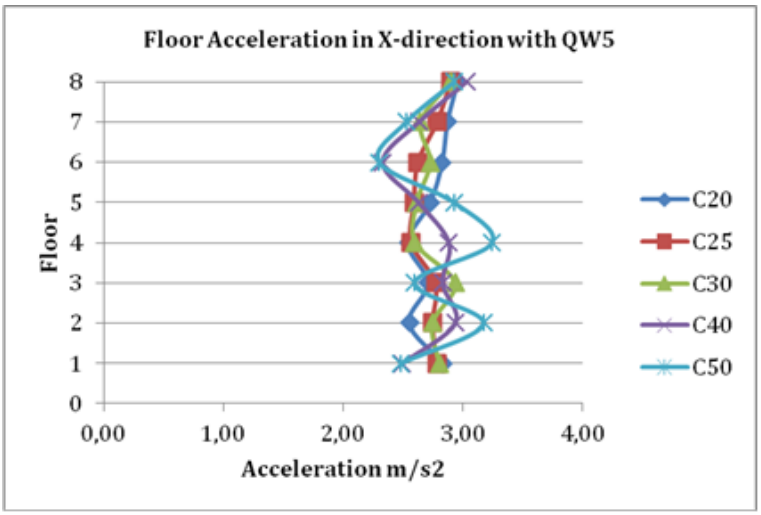

Fig. 5. Floor acceleration in *X*-direction with QW5.

Floor accelerations in global Y-direction with the isolation system having characteristic strength of 5% are shown in Fig. 6. In this case, buildings with concrete class C25 and C30 showed more and less similar trend as it was moved from first floor towards the top floor. However, all the buildings i.e. with C20, C25, C30, C40, C50 showed similar increasing acceleration trend in the upper floors. Top floor accelerations in all cases were more than the 1st floor accelerations with C40 and C50 showing more accelerations at the top floor as compared to others. C40 and C50 buildings were indeed showing more acceleration at every floor level. It was conjectured that the relatively higher top floor accelerations of the building with C40 and C50 could be attributable to the reduction in the number of plastic hinges that were occurred in the columns.

As can be seen in Fig. 7, with the increase in characteristic strength of the isolation system i.e. at 10% characteristic strength or in other words with the increase in damping of the isolation system, the variations in accelerations become much more prominent even for the lower concrete classes i.e. C20, C25, C30 etc. The top floor accelerations were not same either as shown in Fig. 4. As it was moved from 6th to 8th floor an increasing trend of accelerations is observed for all the buildings. Like seismically isolated buildings with isolation system having 5% characteristic strength, C40 and C50 concrete buildings showed less first floor accelerations as compared to the lower concrete class buildings.

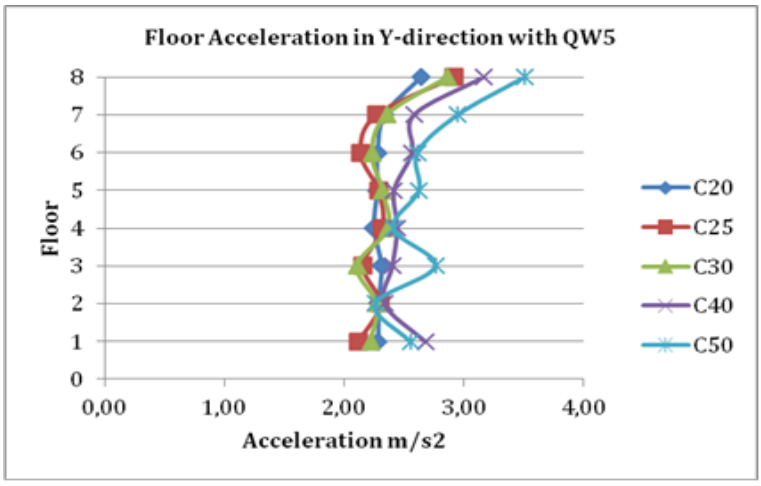

Fig. 6. Floor acceleration in *Y*-direction with QW5.

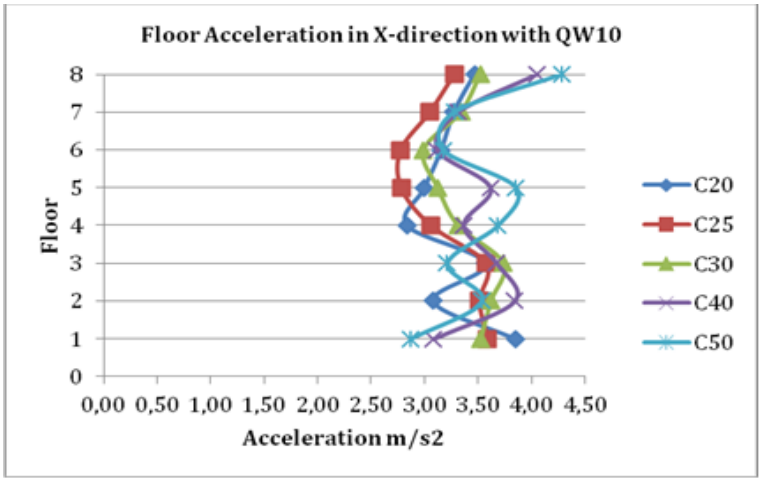

Fig. 7. Floor acceleration in *X*-direction with QW10.

With the characteristic strength of the isolation system of 10%, the floor acceleration pattern in *Y*-direction is presented in Fig. 8. A sharp increase in accelerations for upper floors i.e. 6th to 8th could be clearly seen in the figure.

For all the cases considered, in general the mid floor levels were seen to be the most suitable for housing the equipment or machinery sensitive to vibrations as these floor levels experience less accelerations compared to others. Upper floors have been found to be the least favourable choice for vibration sensitive equipments.

3.2. Story shears

Story shears in X and Y directions, for all the 8 story buildings obtained with isolation system having 5% characteristic strength, are presented in Figs. 9 and 10, respectively. For all the buildings with different concrete classes similar trend of (more or less linearly) decreasing shears has been observed (as we move from base towards top floor). Seismically isolated buildings with concrete C40 and C50, however, showed slight deviation from C20, C25, and C30 in both directions. Moreover, base shear values were almost same for all of the buildings in question.

With isolation system of characteristic strength 10%, though shear values are higher, the trend of shear in *X*-direction was approximately same as of 5% characteristic strength with very small variation observed at lower and mid floor levels (Fig. 11). At this strength level, base shear values were also almost same for all the buildings as evident in Fig. 7. However, if it was looked at the shears in *Y*-direction there was a clear difference in trend at upper floor levels as compared to *X*-direction but the trend is same for all the buildings i.e. buildings with concrete C20, C25, C30, C40, and C50 follow the same trend (Fig. 12).

3.3. Inter-story drift ratios

At characteristic strength level of 5%, all the buildings follow the same inter-story drift ratio trend in both *X* and *Y* directions as can be seen in Figs. 13 and 14, respectively. The inter-story drift ratios first increased then decreased which was again followed by an increase and a decrease in values with the lowest value observed for the top floor level (as we move from base towards top floor). Although the trend was same for all the concrete buildings, the buildings with C40 and C50 concrete showed slightly higher values at each floor level (building with C50 in particular). In fact, a sharp increase of drift ratios was seen at 2nd and 4th floor levels especially.

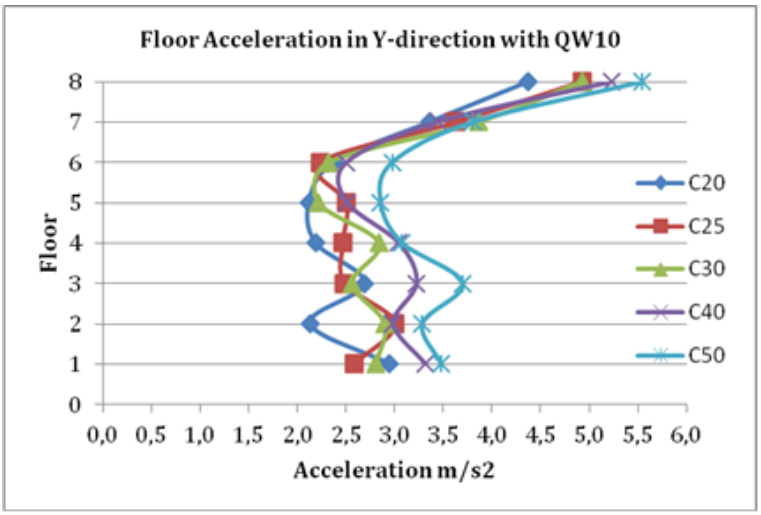

Fig. 8. Floor acceleration in *Y*-direction with QW10.

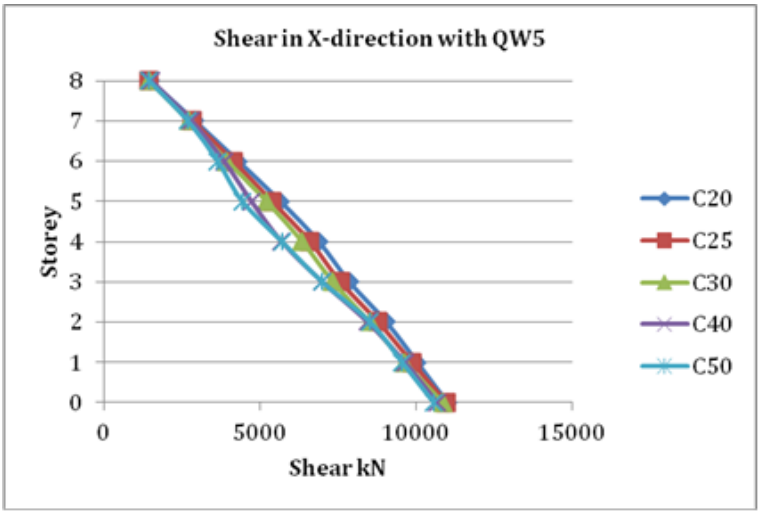

Fig. 9. Story shears in *X*-direction with QW5.

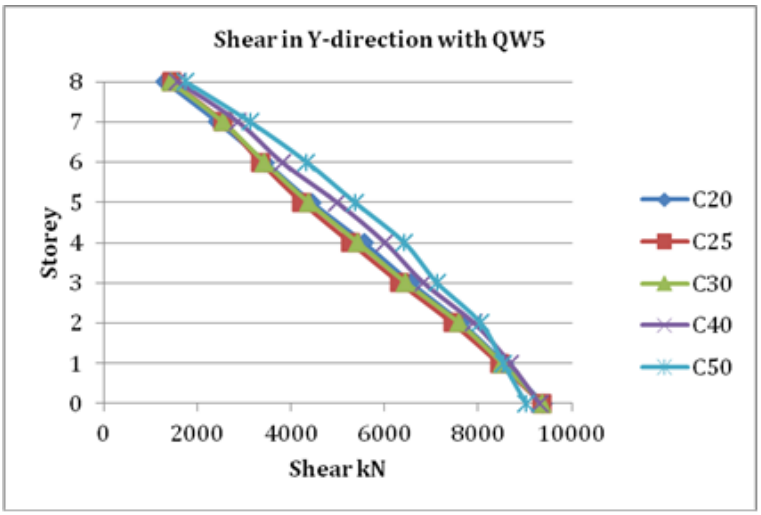

Fig. 10. Story shears in *Y*-direction with QW5.

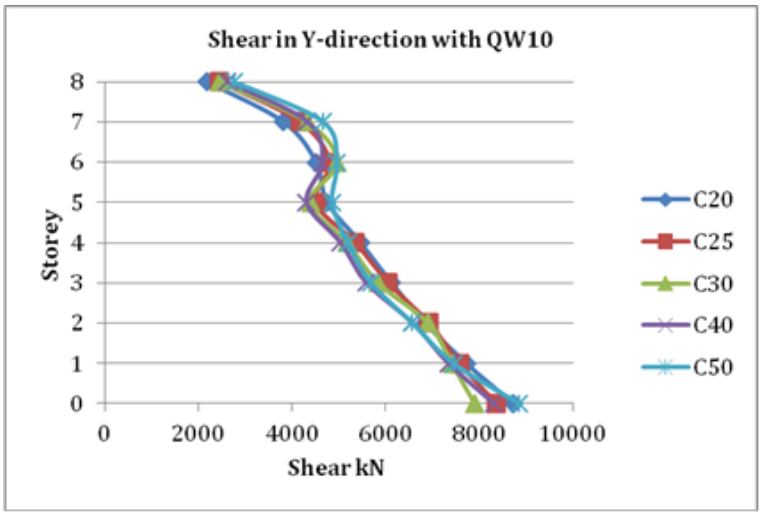

Fig. 11. Story shears in *Y*-direction with QW10.

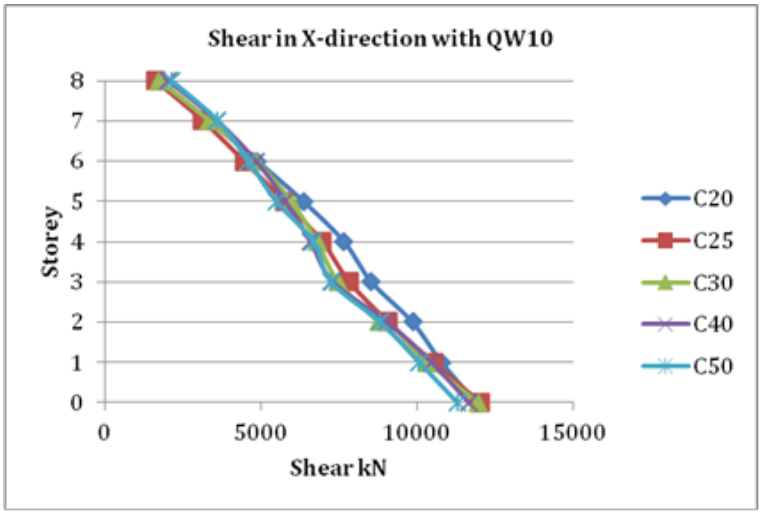

Fig. 12. Story shears in *Y*-direction with QW10.

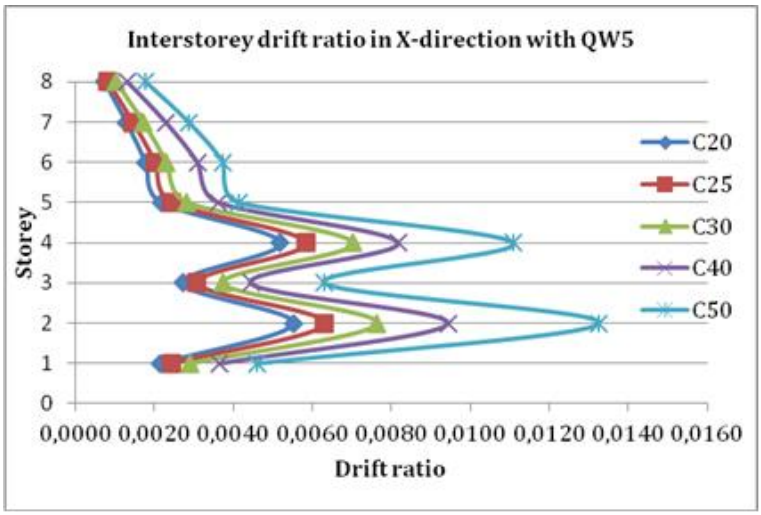

Fig. 13. Inter-story drifts in *X*-direction with QW5.

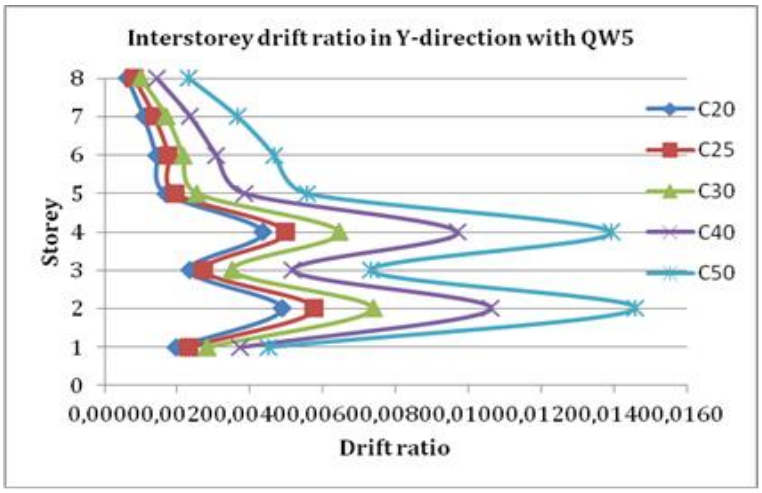

Fig. 14. Inter-story drifts in *Y*-direction with QW5.

With the characteristic strength level of 10%, the overall trend for all buildings remains the same as seen with 5% characteristic strength level. But here isolated buildings with C40 and C50 concrete showed much more inter-story drift ratio values at each floor level as compared to isolated buildings with C20, C25 and C30 concrete which showed values very close to one another. A sharp increase in inter-story drift ratios at 2nd and 4th floor levels for buildings with C40 and C50 was clearly evident in Figs. 15 and 16. This probably reflects the fact that there was more deformation on local vertical members accompanied with destructive tensile strains during the dynamic loading.

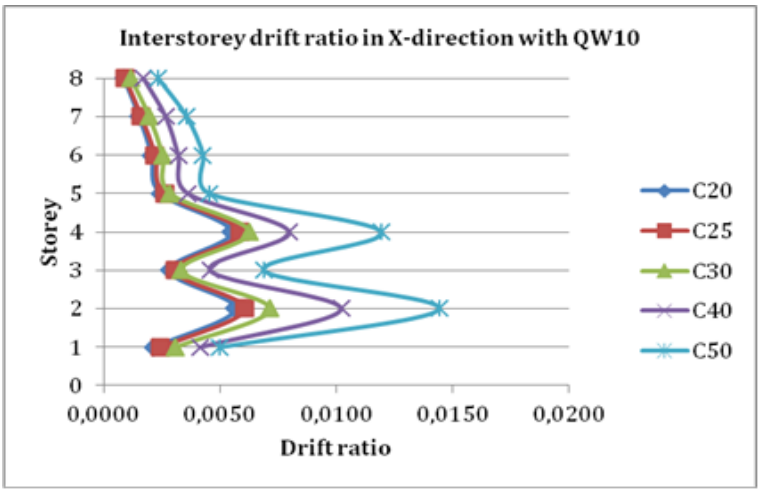

Fig. 15. Inter-story drifts in *X*-direction with QW10.

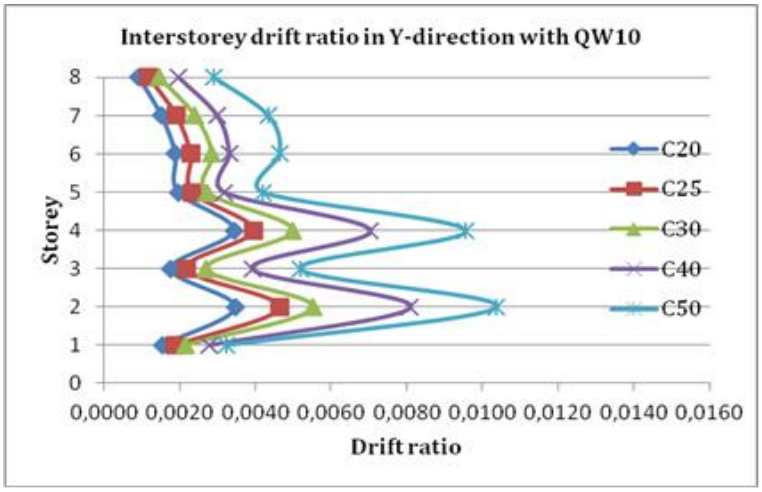

Fig. 16. Inter-story drifts in *Y*-direction with QW10.

4. Conclusions

Concrete strength have considerable effects on the earthquake behaviour of the seismically isolated structures. Floor accelerations, story shears and inter-story drift ratios were significantly affected by the concrete strength class. In general for all the cases considered, buildings with C50 concrete exceeds the maximum inter-story drift ratio limit imposed by UBC at 2nd and 4th floor (with R=1). In fact, buildings with C40 concrete also exceeds the inter-story drift ratio limit in some cases. Inter-story drifts beyond a certain level may be dangerous for the integrity of the building. For all the cases considered, in general the mid floor levels are seen to be the most suitable for housing the equipment or machinery sensitive to vibrations as these floor levels experience less accelerations compared to others. Upper floors have been found to be the least favourable choice for vibration sensitive equipments. With isolation system of characteristic strength 10%, there is a clear difference in trend at upper floor levels for the shear values in Y-direction as compared to X-direction but the trend is same for all the buildings with concrete C20, C25, C30, C40, and C50 follow the same trend. In a future research study, effects of concrete strength on the seismic response of seismically isolated RC buildings which has irregular geometrical configurations should be investigated.

References

Bayraktar A, Altunisik AC, Turker T, Karadeniz H, Erdogdu S, Angin Z, Ozsahin TS (2014). Structural performance evaluation of 90 rc buildings collapsed during the 2011 Van-Turkey earthquakes. *Journal of Performance of Construction Facilities*, 6, 410-440.

Coskan S, Kartal ME, Bilir T (2015). The effect of concrete strengths obtained from 2011 Van Earthquake on the structural performance of RC Buildings. *Arabian Journal for Science and Engineering*, 41(10), 3817-3825.

Erberik MA (2008). Fragility-based assessment of typical mid-rise and low-rise RC buildings in Turkey. *Engineering Structures*. 30, 1360-1374.

Erdem TR (2016). Performance evaluation of reinforced concrete buildings with softer ground floors. *Gradevinar*, 68, 39-49.

Golghate K, Vijay B, Amit S (2013). Pushover analysis of 4 storey's reinforced concrete building. *International Journal of Latest Trends in Engineering and Technology*, 2, 80-84.

Hwang J, Hsu T (2000). Experimental study of isolated building under trixial ground excitations. *Journal of Structural Engineering*, 126, 879-886.

Kocak A (2005). Detailed examination of some existing buildings located at different districts of Istanbul and earthquake risk analysis of these existing buildings. *In: The Earthquake Symposium*, Kocaeli, 700-702.

Madden G, Symans M, Wongpraset N (2002). Experimental verification of seismic response of building frame with adaptive sliding base-isolation system. *Journal of Structural Engineering*, 128(8), 1037-1045,

Pant DR, Wijeyewickrema AC (2012). Structural performance of a base-isolated reinforced concrete building subjected to seismic pounding. *Earthquake Engineering and Structural Dynamics*, 41(12), 1709-1716.

Pereira N, Romao X (2016a). Material strength safety factors for the seismic safety assessment of existing RC buildings. *Construction and Building Materials*, 119, 319-328.

Pereira N, Romao X (2016b). Assessment of the concrete strength in existing buildings using a finite population approach. *Construction and Building Materials*, 110, 106-110.

Peruš I, Klinc P, Dolenc M, Dolšek M (2013). A web-based methodology for the prediction of approximate IDA curves. *Earthquake Engineering & Structural Dynamics*, 42, 43-60.

Rozman M, Fajfar P (2009). Seismic Response of a RC frame building designed according to old and modern practices. *Bulletin of Earthquake Engineering*, 7(3), 779-799.

Verderame GM, Polese M, Mariniello C, Manfredi G (2010). A simulated design procedure for the assessment of seismic capacity of existing reinforced concrete buildings. *Advances in Engineering Software*, 14, 323-335.

Challenge Journal of Structural Mechanics

Optimal strain gage location for determination of mode I stress intensity factor for orthotropic laminates using a single strain gage

Debabrata Chakraborty *, Debaleena Chakraborty, K. S. R. Krishna Murthy

Department of Mechanical Engineering, Indian Institute of Technology Guwahati, Guwahati 781039, India

ABSTRACT

The present work discusses a robust method developed for determination of mode I stress intensity factor (K_I) of orthotropic laminates using a single strain gage and based on a three parameter strain series representation ahead of the crack tip. Appropriate radial location of the strain gage ahead of the crack tip is important in the sense that strain gages placed either very near or very far from the crack tip might lead to inaccuracies in the estimated SIFs due to 3D effects near the crack tip or inaccurate strain field representation at farther distances. The theoretical formulation has been presented for determination of angular location, orientation and the upper bound on the radial location (r_{max}) for pasting the strain gage which could be subsequently used for accurate determination of K_I. Numerical simulations have been presented considering edge cracked $[90_2/0]_{10S}$ carbon-epoxy orthotropic laminates to illustrate the determination of r_{max} and K_I of such laminates.

ARTICLE INFO

Article history:
Received 21 August 2016
Accepted 24 September 2016

Keywords:
Orthotropic
Stress intensity factor
Strain gage
Gage location
Radial location

1. Introduction

Fracture mechanics analyses of composite materials is essential due to the increasing use of these materials in many engineering applications. The concepts of linear elastic fracture mechanics (LEFM) of relevance to isotropic materials have also been employed to composite materials after incorporating suitable provision to take care of the directional properties of such materials, the pioneering works towards which was started off by Irwin (1962) and Wu (1963). The effective application of LEFM in predicting and preventing fracture lies in the availability of accurate values of SIF, which is n LEFM parameter that decides whether an existing crack in a component grows or not. Experimental determination of SIFs of cracked composite panels has raised substantial interest not only in complex situations but also to validate the numerical and analytical results. Among the experimental techniques, the simplest and least expensive is the method of SIF determination using strain gages.

In case of isotropic materials, a single strain gage technique proposed by Dally and Sanford (1987) was the first practical and feasible approach towards determination of mode I SIF (K_I) of plane problems. The Dally and Sanford technique or popularly the DS technique is based on a three parameter representation of the strain field around the crack tip and necessitates a single strain gage oriented along a certain angle, ϕ and placed at a location decided by the angle, θ as shown in Fig. 1. The radial distance of the strain gage with respect to the crack tip also plays a very crucial role in ensuring the accuracy of the SIFs estimated using strain gages. Strain gages placed either very near or very far from the crack tip might lead to inaccuracies in the estimated SIFs due to 3D effects, strain gradients near the crack tip or inaccurate strain field representation at farther distances. This issue was addressed for the first time by Sarangi and co-workers for isotropic materials (2010). They proposed a methodology to estimate the optimal location of a strain gage in association with the DS technique.

For orthotropic materials, only recently Chakraborty et al. (2014) presented an extension of the DS technique in entirety for determination of K_I. Suggestions for optimal gage locations were also proposed employing a finite element based approach supported with proper theoretical formulations. Using the same technique, an

* *Corresponding author*. Tel.: +91-361-2582666 ; Fax: +91-361-2582699 ; E-mail address: chakra@iitg.ernet.in (D. Chakraborty)
ISSN: 2149-8024 / DOI: http://dx.doi.org/10.20528/cjsmec.2016.09.024

attempt has been made in the present work to determine (K_I) of $[90_2/0]_{10S}$ Carbon-epoxy laminates having an edge-cracked configuration using numerical simulations. In addition, the influence of optimal gage locations on the accuracy of the estimated SIFs has also been studied using numerical analysis.

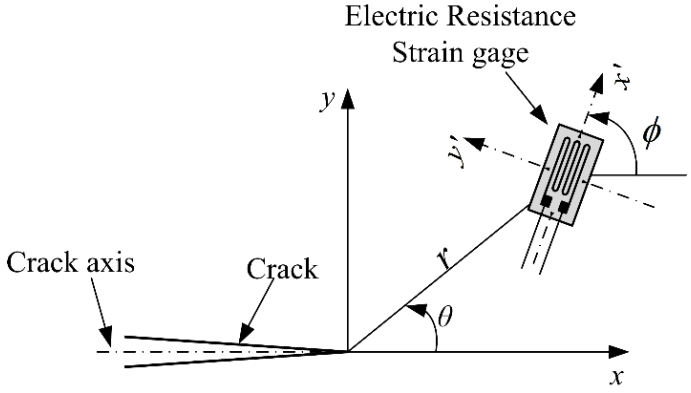

Fig. 1. Location of a strain gage.

2. Theoretical Background

The single strain gage technique that has been developed for the determination of K_I of orthotropic materials as an extension of the DS technique is presented here. Furthermore, the theoretical framework for estimating the optimal gage location has also been shown. For orthotropic materials, the normal strain component at a point $P(r,\theta)$ along ϕ (refer Fig. 1) for plane stress conditions, taking into account a three parameter strain series representation can be written as

$$\varepsilon_{x'x'} = A_0\left\{\begin{array}{l}\left[\frac{1}{\sqrt{r_1}}\left(\left(\cos\frac{\theta_1}{2}\frac{\alpha-\beta}{2\alpha}\begin{pmatrix}\cos^2\phi(-\alpha_{11}(\alpha+\beta)^2+\alpha_{12})\\+\sin^2(-\alpha_{12}(\alpha+\beta)^2+\alpha_{22})\end{pmatrix}\right)-\left(\sin\frac{\theta_1}{2}a_{66}\sin\phi\cos\phi\left(\frac{\alpha^2-\beta^2}{2\alpha}\right)\right)\right)\right]\\+\left[\frac{1}{\sqrt{r_2}}\left(\left(\cos\frac{\theta_2}{2}\frac{\alpha-\beta}{2\alpha}\begin{pmatrix}\cos^2\phi(-\alpha_{11}(\alpha+\beta)^2+\alpha_{12})\\+\sin^2(-\alpha_{12}(\alpha+\beta)^2+\alpha_{22})\end{pmatrix}\right)+\left(\sin\frac{\theta_2}{2}a_{66}\sin\phi\cos\phi\left(\frac{\alpha^2-\beta^2}{2\alpha}\right)\right)\right)\right]\end{array}\right\}$$

$$+A_1\left\{\begin{array}{l}\left[\sqrt{r_1}\left(\left(\cos\frac{\theta_1}{2}\frac{\alpha-\beta}{2\alpha}\begin{pmatrix}\cos^2\phi(-\alpha_{11}(\alpha+\beta)^2+\alpha_{12})\\+\sin^2(-\alpha_{12}(\alpha+\beta)^2+\alpha_{22})\end{pmatrix}\right)+\left(\sin\frac{\theta_1}{2}a_{66}\sin\phi\cos\phi\left(\frac{\alpha^2-\beta^2}{2\alpha}\right)\right)\right)\right]\\+\left[\sqrt{r_2}\left(\left(\cos\frac{\theta_2}{2}\frac{\alpha-\beta}{2\alpha}\begin{pmatrix}\cos^2\phi(-\alpha_{11}(\alpha+\beta)^2+\alpha_{12})\\+\sin^2(-\alpha_{12}(\alpha+\beta)^2+\alpha_{22})\end{pmatrix}\right)-\left(\sin\frac{\theta_2}{2}a_{66}\sin\phi\cos\phi\left(\frac{\alpha^2-\beta^2}{2\alpha}\right)\right)\right)\right]\end{array}\right\}$$

$$+B_0\left\{\frac{\beta}{2\alpha}[(\alpha+\beta)^2-(\beta-\alpha)^2](a_{11}\cos^2\phi+a_{12}\sin^2\phi)\right\}, \quad (1)$$

where,

$$a_{11}=1/E_L \;,\; a_{12}=-v_{LT}/E_L=-v_{TL}/E_T \;,\; a_{66}=1/G_{LT} \;,\; 2\beta^2=\frac{a_{66}+2a_{12}}{2a_{11}}+\sqrt{\frac{a_{22}}{a_{11}}} \;,\; 2\alpha^2=\frac{a_{66}+2a_{12}}{2a_{11}}-\sqrt{\frac{a_{22}}{a_{11}}}, \quad (2)$$

and

$$\tan\theta_1=(\beta+\alpha)\tan\theta \quad , \quad \tan\theta_2=(\beta-\alpha)\tan\theta \;,$$

$$r_1^2=r^2(\cos^2\theta+(\beta+\alpha)^2\sin^2\theta) \quad , \quad r_2^2=r^2(\cos^2\theta+(\beta-\alpha)^2\sin^2\theta). \quad (3)$$

L and T represent the longitudinal and transverse direction of the laminate (Fig. 1) and E, v and G represent Young's modulus, Poisson's ratio and shear modulus respectively. The specific values of ϕ and θ for which the coefficients of the terms containing A_1 and B_0 become zero are obtained as

$$\tan^2\phi = -a_{11}/a_{12} = 1/v_{LT}\,, \tag{4}$$

and

$$\sqrt[4]{(\cos^2\theta + (\beta+\alpha)^2\sin^2\theta)}\left\{\begin{array}{l}\left[\frac{1}{E_T}\left(\frac{1-v_{LT}v_{TL}}{1+v_{LT}}\right)\frac{\alpha-\beta}{2\alpha}\cos\left(\frac{1}{2}\left(\tan^{-1}\left((\beta+\alpha)\tan\theta\right)\right)\right)\right] \\ -\left[\frac{1}{G_{LT}}\left(\frac{v_{LT}}{(1+v_{LT})\sqrt{v_{LT}}}\right)\frac{1}{2\alpha}\sin\left(\frac{1}{2}\left(\tan^{-1}\left((\beta+\alpha)\tan\theta\right)\right)\right)\right]\end{array}\right\} +$$

$$\sqrt[4]{(\cos^2\theta + (\beta-\alpha)^2\sin^2\theta)}\left\{\begin{array}{l}\left[\frac{1}{E_T}\left(\frac{1-v_{LT}v_{TL}}{1+v_{LT}}\right)\frac{\alpha-\beta}{2\alpha}\cos\left(\frac{1}{2}\left(\tan^{-1}\left((\beta-\alpha)\tan\theta\right)\right)\right)\right] \\ +\left[\frac{1}{G_{LT}}\left(\frac{v_{LT}}{(1+v_{LT})\sqrt{v_{LT}}}\right)\frac{1}{2\alpha}\sin\left(\frac{1}{2}\left(\tan^{-1}\left((\beta-\alpha)\tan\theta\right)\right)\right)\right]\end{array}\right\} = 0\,, \tag{5}$$

respectively. Therefore, Eq. (1) may be rewritten using these values of θ and ϕ as

$$\varepsilon_{x'x'} = \frac{1}{\sqrt{r}}\times A_0\left\{\begin{array}{c}\frac{1}{E_T}\left(\frac{1-v_{LT}v_{TL}}{1+v_{LT}}\right)\frac{1}{2\alpha}\left[\frac{\cos\left(\frac{1}{2}\tan^{-1}\left((\beta+\alpha)\tan\theta\right)\right)}{\sqrt[4]{(\cos^2\theta+(\beta+\alpha)^2\sin^2\theta)}}(\alpha-\beta)+\frac{\cos\left(\frac{1}{2}\tan^{-1}\left((\beta-\alpha)\tan\theta\right)\right)}{\sqrt[4]{(\cos^2\theta+(\beta-\alpha)^2\sin^2\theta)}}(\alpha+\beta)\right] \\ +\frac{1}{G_{LT}}\left\{\frac{v_{LT}}{(1+v_{LT})\sqrt{v_{LT}}}\right\}\frac{1}{2\alpha}\left[\frac{\sin\left[\frac{1}{2}\tan^{-1}\{(\beta+\alpha)\tan\theta\}\right]}{\sqrt[4]{(\cos^2\theta+(\beta+\alpha)^2\sin^2\theta)}}-\frac{\sin\left[\frac{1}{2}\tan^{-1}\{(\beta-\alpha)\tan\theta\}\right]}{\sqrt[4]{(cos^2\theta+(\beta-\alpha)^2\sin^2\theta)}}\right]\end{array}\right\} = \frac{A_0}{\sqrt{r}}\times C = \frac{C'}{\sqrt{r}}\,, \tag{6}$$

where C is a constant for a given value of θ, ϕ and material properties. From standard definition, the mode I SIF, (K_I) can be obtained from the coefficient A_0 as

$$K_I = \sqrt{2\pi}A_0\,. \tag{7}$$

Now, taking logarithm on both sides of Eq. (6) we get

$$\ln(\varepsilon_{x'x'}) = -\frac{1}{2}\ln(r) + \ln(C')\,. \tag{8}$$

Eq. (8) represents a straight line between $\ln(\varepsilon_{x'x'})$ and $\ln(r)$ with a slope of -0.5 and an intercept of $\ln(C')$. The straight line property remains up to a certain radial location from the crack tip ($r_{\max}$) and deviates beyond that as more than three parameters would be needed in Eq. (1) to estimate the $\varepsilon_{x'x'}$. It has been reported earlier by Shukla et al. (1989) that for orthotropic materials 3D effects prevailed up to a radial distance equal the thickness of the plate from the crack tip. Therefore, the minimum radial distance ($r_{\min}$) for strain measurements on the free surface which are under plane stress conditions should be greater than the thickness of the plate. As a consequence, the optimal gage location for pasting a strain gage can be given as

$$r_{\min}(=\text{thickness of plate}, t) \le r \le r_{\max}\,. \tag{9}$$

Thus, by placing a single strain gage as shown in Fig. 1 oriented at an angle of ϕ at a radial distance r within $r_{\max}$ from the crack tip along the gage line at an angle of θ, the measured strain $\varepsilon_{x'x'}$ can be used to obtain (K_I) using Eqs. (6) and (7).

3. Numerical Simulations

An edge cracked $[90_2/0]_{10S}$ carbon-epoxy laminate with b=100 mm, a/b=0.4, h/b=2 and material properties as E_L= 67.77 GPa, E_T=142.7 GPA, v_{LT}=0.01, G_{LT}=4.304 GPa subjected to uniform tensile stress (σ=100 MPa) is considered (Fig. 2(a)). Following the procedure described in Section 2, the values of ϕ and θ for which the coefficients B_0 and A_1 become zero are found to be 84^0 and 61^0 respectively. Fig. 2(b) shows the analysis domain with boundary conditions used for the numerical analysis.

Finite element analysis is carried out using ANSYS 14 where, eight noded isoparametric elements (PLANE 183) have been used for finite element discretization of the plate and quarter point elements (QPE) have been used around the crack-tip to model the $\sqrt{r}$ singularity. Fig. 3(a) shows the typical finite element mesh considered after proper convergence study. The mesh has been designed such that the nodes of several elements are made to lie along the gage line which starts at the crack tip and terminates at the outer boundaries. According to the present technique, a single strain gage is to be placed at an appropriate location along the gage line and oriented along ϕ within the estimated $r_{\max}$ for the configuration in order to measure the linear strain $\varepsilon_{x'x'}$.

From the finite element results, the linear strain $\varepsilon_{x'x'}$ and radial distance (r) are computed for all the nodes along the gage line. Fig. 3(b) gives the plot of $\ln(\varepsilon_{x'x'})$ versus $\ln(r)$ for all the nodal values along the gage line. Crack tip point is not plotted as the radius of this point is zero. It can be seen that the plot consists of a linear plot followed by a non-linear one as predicted by the theory.

The radial distance at which the plot changes from a linear to a non-linear one gives the value of r_{max} or the extent of the three parameter zone or the optimal radial location for the particular configuration for pasting the strain gage. A line of slope -0.5 is superposed on the plot of $\ln(\varepsilon_{x'x'})$ versus $\ln(r)$ and considering this line to be the exact solution, absolute percentage relative error at all values of radius of this plot is calculated. Finally, r_{max} is estimated as the radius at which the error is less than 1% (as one goes from right to left in Fig. 3(b)). The r_{max} for the configuration corresponding to the present problem is found to be 34 mm.

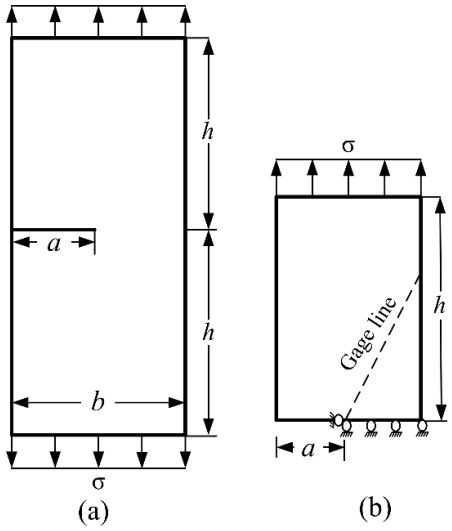

Fig. 2. (a) Orthotropic edge-cracked laminate; (b) Analysis domain for FEA.

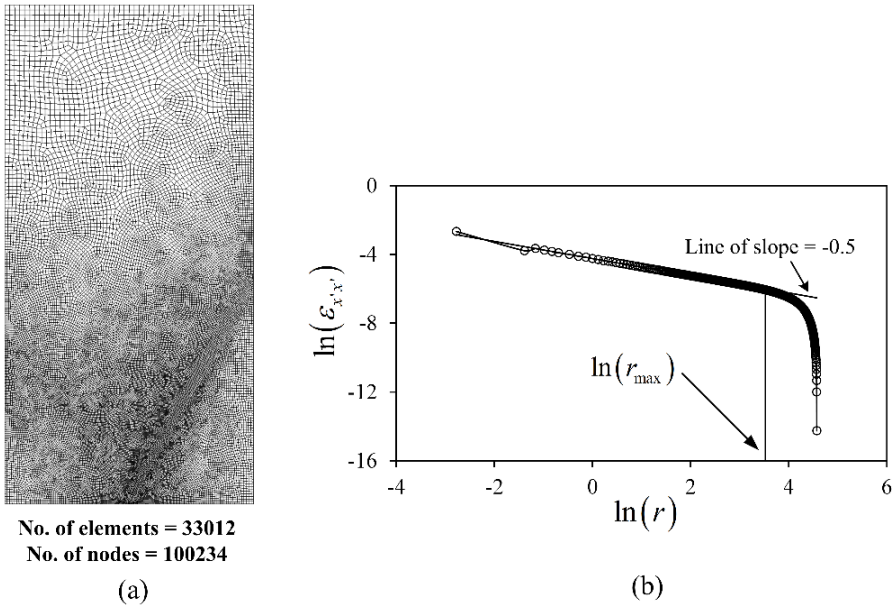

Fig. 3. (a) FE mesh of the laminate with a/b=0.5; (b) Plot of $\ln(\varepsilon_{x'x'})$ vs. $\ln(r)$ along the gage line.

The analytical value of mode I SIF of this configuration which will act as reference solution as per Tada et al. (2000) handbook is given by

$$K_I = Y_I(a/b)\sigma\sqrt{a}\,, \tag{10}$$

where σ is the applied stress, a is the crack length and Y_I is the specimen geometric factor given by

$$Y_I = 1.99 - 0.41(a/b)1.87(a/b)^2 - 38.48(a/b)^3 + 53.85(a/b)^4\,. \tag{11}$$

For this configuration with a/b of 0.5 and loaded at σ=100 MPa the reference value of K_I is 52.8 MPa$\sqrt{m}$. Radial locations are selected within the optimal locations and outside the simulated r_{max} (non-optimal locations) to establish the importance of radial positioning of the strain gage. Measured K_I using Eqs. (6) and (7) from the strain readings at the selected radial locations are shown in Table 1. The percentage relative error in K_I measured at those locations is computed as

$$\%\ \text{Rel. error} = \frac{K_{\text{reference solution}} - K_{\text{measured or simulated}}}{K_{\text{reference solution}}} \times 100\,. \tag{12}$$

Table 1 also enlists the computed relative error at the select radial locations. Results in Table 1 clearly show that it is possible to accurately determine K_I (error less than 2%) for an edge-cracked orthotropic laminate using a single strain gage if the gage is placed within r_{max}. On the other hand placing a strain gage outside r_{max} leads to highly inaccurate values of K_I. These results substantiate that the present technique of determination of K_I. Using a single strain gage can be used for accurate determination of K_I for single ended cracked $[90_2/0]_{10S}$ carbon-epoxy composite specimens if the gages are placed within the optimal locations.

Table 1. K_I of the edge cracked $[90_2/0]_{10S}$ carbon-epoxy laminate at optimal and non-optimal positions.

r (mm)	$r_{max} = 34$ mm	$\varepsilon_{x'x'}$	$K_I(\text{MPa}\sqrt{m})$	% Relative error
20.08	optimal	1.57E-03	53.04	0.45
25.18	optimal	1.38E-03	52.21	1.17
42.53	non-optimal	9.13E-04	44.89	14.98
50.19	non-optimal	7.11E-04	37.97	28.09

3.1. *Influence of a/b on r_{max}*

In order to study the effect of a/b on r_{max}, edge cracked $[90_2/0]_{10S}$ carbon-epoxy laminates with a/b ranging from 0.1 to 0.8 are considered, the other specifications of which including the material properties are same as that have been used in the previous example. The plots of $\ln(\varepsilon_{x'x'})$ vs. $\ln(r)$ for the nodes along the gage line for all the edge-cracked laminates are shown in Fig. 4(a). Following the procedure used in the previous example, the r_{max} value estimated for all the configurations is shown in Table 2.

Table 2. Variation of r_{max} with a/b.

a/b	r_{max}	r_{max}/b
0.1	4.5	0.045
0.2	7.8	0.078
0.3	15.5	0.155
0.4	34	0.34
0.5	67	0.67
0.6	19	0.19
0.7	10.9	0.109

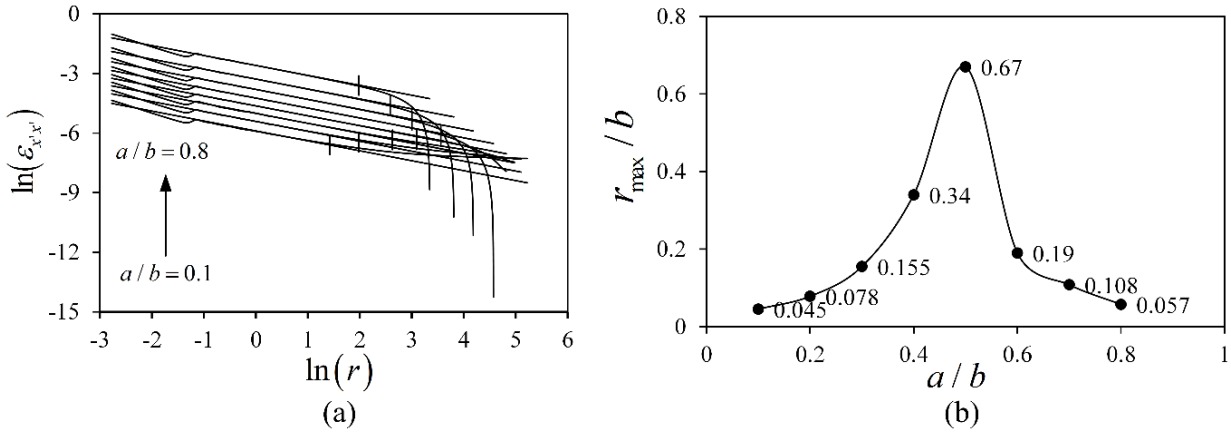

Fig. 4. (a) $\ln(\varepsilon_{x'x'})$ vs. $\ln(r)$ with a/b =0.1 to 0.8; (b) Variation of r_{max}/b as a function of a/b.

Variation of non-dimensional r_{max}/b as a function of a/b is shown in Fig. 4(b). It may be observed that the r_{max} increases initially with increase in a/b, with a gradual decrease at higher values of a/b. This may be due to the fact that at low values of a/b, crack length in the controlling parameter for changes in r_{max}. However, as the crack length increases, beyond a certain point, the boundary effects start having an impact on the r_{max} as the gage line proceeds very near to the gage line.

4. Conclusions

The single strain gage technique for the determination of mode I SIF of orthotropic laminates stands verified for the selected $[90_2/0]_{10S}$ carbon-epoxy edge cracked laminates. Numerical simulations show that accurate values of K_I can be obtained only for strain gage readings within the optimal gage locations and K_I estimated for the numerically estimated strains at the non-optimal radial locations are erroneous. Furthermore, the optimal gage locations or r_{max} is found to be dependent on both the crack length and the nearness to the boundary (boundary effects).

References

Chakraborty D, Murthy KSRK, Chakraborty D (2014). A new single strain gage technique for determination of mode I stress intensity factor in orthotropic composite materials. *Engineering Fracture Mechanics*, 124-125, 142-54.

Dally JW, Sanford RJ (1987). Strain gage methods for measuring the opening mode stress intensity factor. *Experimental Mechanics*, 27, 381-388.

Irwin GR (1962). Analytical aspects of crack stress field problems. T&AM Report No. 213, University of Illinois, Urbana.

Sarangi H, Murthy KSRK, Chakraborty D (2010). Radial locations of strain gages for accurate measurement of mode I stress intensity factor. *Materials and Design*, 31, 2840–2850.

Shukla A, Agarwal BD, Bhusan B (1989). Determination of stress intensity factor in orthotropic composite materials using strain gages. *Engineering Fracture Mechanics*, 32, 469-77.6.

Tada H, Paris PC, Irwin GR (2000). The stress analysis of cracks handbook. ASME, New York.

Wu EM (1963). On the application of fracture mechanics to orthotropic plates. T&AM Report No. 248, University of Illinois, Urbana.

Challenge Journal of Structural Mechanics

Case Study

Girkmann problem with a Discrete Element Method

Christian Mariotti *

CEA, DAM, DIF, F.91297 Arpajon, France

ABSTRACT

Cells of Voronoï are used as particles in the Discrete Element code CeaMka3D. This type of meshing does not leave geometrical space like that can be the case with spherical particles. This method has already been used successfully to simulate the propagation of seismic waves in a linear elastic medium in 2D or in 3D. In this paper, a specific axisymmetric formulation is presented. In a first part, the calculation of the volumetric deformation of a particle and the forces between particles are described. In a second part, the specific forces for the axisymmetric formulation are described. At last, this formulation is tested for the Girkmann problem. This axisymmetric benchmark has been presented in January 2008 by the International Association of Computational Mechanics (IACM) in order to test the singularity at the junction between shell and beam. The accuracy of the axisymmetric formulation for this Discrete Element Method is evaluated by this benchmark. The results of this Discrete Element Method are compared with others numerical methods.

ARTICLE INFO

Article history:
Received 24 June 2016
Accepted 3 August 2016

Keywords:
Elasticity
Meshless
Axisymmetric
Discrete Element Method

1. Introduction

Particle methods are meshless simulation techniques in which a continuum medium is approximated through the dynamics of a set of interacting solids. These include the Discrete Element Methods (DEM) first developed by Hoover and al. (1974) in models for crystalline materials. They were applied to geotechnical problems by Cundall and Strack (1979).

A Discrete Element code CeaMka3D has been developed by Mariotti and Monasse (2012). This method has been used successfully to simulate, for example, the propagation of seismic waves in a linear elastic medium by Mariotti (2007). This code has also been coupled with a finite element code by Mariotti et al. (2015) and a new symplectic leapfrog scheme has been developed in order to integrate 3D rigid-body rotation with external torque by Mariotti (2015).

After a determination of the volumetric strain in 3D, the axisymmetric forces are described in order to recover Hooke's law. In the last part, the simulation with CeaMka3D of the Girkmann problem is presented. This problem has been described by Girkmann (1956) and studied by Timoshenko and Woinowsky-Krieger (1959). This axisymmetric benchmark has been presented in January 2008 by the International Associadtion of Computational Mechanics (IACM) in order to test the singularity at the junction between shell and beam. It has been studied as a benchmark problem by Pitkäranta et al. (2008) and Devloo et al. (2013).

2. The Volumetric Strain in 3D

The initial choice was to take a Voronoï mesh which allows, from a field of points, to bound polyhedrons. This type of meshing does not leave geometrical space like that can be the case with spherical particles. By geometrical construction, the plan of contact between two particles is perpendicular to the line connecting the centers of particles.

For example; let n be the normal direction between particles A and B as shown in Fig. 1.

$$n = \frac{AB}{\|AB\|} \ . \tag{1}$$

* *Corresponding author*. Tel.: +33-169-264000 ; Fax: +33-169-267130 ; E-mail address: christian.mariotti@cea.fr (C. Mariotti)
ISSN: 2149-8024 / DOI: http://dx.doi.org/10.20528/cjsmec.2016.08.017

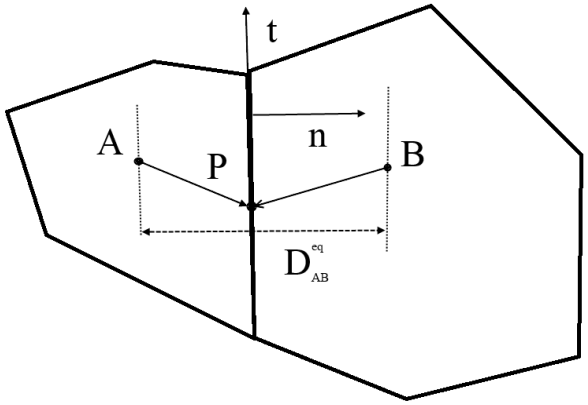

Fig. 1. Initial contact between two particles.

The initial distance between particles A and B at time t=0 is defined by:

$$D_{AB}^{eq} = \|AB\|_{t=0} . \quad (2)$$

The relative movement of both particles A and B according to the normal is defined by:

$$D_{AB}^{n} = D_{AB}^{eq} - \|AB\| . \quad (3)$$

It is necessary to choose the method of calculation of the elastic volumetric strain of a particle A surrounded by other particles B during their movements.

A particle A has only a part of its surface in touch with the other particles B. A volume of contact is defined by the following relation:

$$V_A^c = \frac{1}{3}\sum_{links\ B}\frac{1}{2}D_{AB}^{eq}S_{AB} , \quad (4)$$

where S_{AB} is the contact area between particles A and B.

The variation of this volume of contact is given by the following equation:

$$\Delta V_A^c = \sum_{links\ B}\frac{1}{2}D_{AB}^{n}S_{AB} . \quad (5)$$

To transform this variation of elastic volume of contact to the elastic volumetric strain, it is necessary to integrate free surfaces of the particle which can also have an elastic strain.

The complementary volume, called free volume, is then defined by:

$$V_A^F = V_A - V_A^c . \quad (6)$$

The variation of elastic volume of the particle A is given by the relation:

$$\varepsilon_A^V = \varepsilon_A^{VC} + \varepsilon_A^{VF} = \frac{\Delta V_A^C + \Delta V_A^F}{V_A} . \quad (7)$$

To define the variation of free volume, it is necessary to return to the Hooke's law. On the free surface and according to the normal for this free surface, the normal constraint is nil, so:

$$\varepsilon_A^{nn} = \frac{-\vartheta}{1-2\vartheta}\varepsilon_A^V \quad (8)$$

where ϑ is Poisson's ratio.

On the other hand, the normal elastic strain of the free surface is connected with the variation of the free volume

$$\varepsilon_A^{nn} = \frac{1}{3}\frac{\Delta V_A^F}{V_A^F} . \quad (9)$$

So:

$$\varepsilon_A^{VF} = \frac{\Delta V_A^F}{V_A} = -3\frac{\vartheta}{1-2\vartheta}\left(\frac{V_A^F}{V_A}\right)\varepsilon_A^V = -3\frac{\vartheta}{1-2\vartheta}\left(1-\frac{V_A^C}{V_A}\right)\varepsilon_A^V , \quad (10)$$

and

$$\varepsilon_A^{VC} = \frac{\Delta V_A^C}{V_A} . \quad (11)$$

So:

$$\varepsilon_A^V = \varepsilon_A^{VC} + \varepsilon_A^{VF} = \frac{\Delta V_A^C}{V_A} - 3\frac{\vartheta}{1-2\vartheta}\left(1-\frac{V_A^C}{V_A}\right)\varepsilon_A^V$$

$$= \frac{\Delta V_A^C}{V_A}\frac{1}{1+3\frac{\vartheta}{1-2\vartheta}\left(1-\frac{V_A^C}{V_A}\right)} . \quad (12)$$

At the end,

$$\varepsilon_A^V = \frac{1}{V_A}\frac{1}{1+3\frac{\vartheta}{1-2\vartheta}\left(1-\frac{V_A^C}{V_A}\right)}\sum_{links\ B}\frac{1}{2}S_{AB}D_{AB}^{n} . \quad (13)$$

An expression for the calculation of the elastic volumetric strain of a particle A has been determined. In the expression of the normal force between particles A and B, the following volumetric strain will be used.

$$\varepsilon_{AB}^V = \frac{1}{2}(\varepsilon_A^V + \varepsilon_B^V) . \quad (14)$$

The normal force between both particles A and B is then given by:

$$F_{AB}^{n} = \left(K_S\frac{D_{AB}^{n}}{D_{AB}^{eq}} + K_V\varepsilon_{AB}^V\right)S_{AB} , \quad (15)$$

with

$$K_S = \frac{E}{1+\vartheta} , \quad (16)$$

$$K_V = \frac{E\vartheta}{(1+\vartheta)(1-2\vartheta)} , \quad (17)$$

where E and ϑ are respectively Young's modulus and Poisson's ratio.

The axisymmetric formulation is examined in the next part.

3. 2D Axisymmetric Formulation

In a cylindrical coordinate system (r, θ, z), some problems are independent with respect to coordinate θ. This symmetry enables reduction to a 2D axisymmetric problem. The expression of Hooke's law gives:

$$\sigma_{rr} = \frac{E}{1+\vartheta}\frac{\partial u_r}{\partial r} + \frac{E\vartheta}{(1+\vartheta)(1-2\vartheta)}\left(\frac{\partial u_r}{\partial r} + \frac{u_r}{r} + \frac{\partial u_z}{\partial z}\right),$$

$$\sigma_{\theta\theta} = \frac{E}{1+\vartheta}\frac{u_r}{r} + \frac{E\vartheta}{(1+\vartheta)(1-2\vartheta)}\left(\frac{\partial u_r}{\partial r} + \frac{u_r}{r} + \frac{\partial u_z}{\partial z}\right),$$

$$\sigma_{zz} = \frac{E}{1+\vartheta}\frac{\partial u_z}{\partial z} + \frac{E\vartheta}{(1+\vartheta)(1-2\vartheta)}\left(\frac{\partial u_r}{\partial r} + \frac{u_r}{r} + \frac{\partial u_z}{\partial z}\right),$$

$$\sigma_{rz} = \frac{E}{2(1+\vartheta)}\left(\frac{\partial u_r}{\partial z} + \frac{\partial u_z}{\partial r}\right),$$

$$\sigma_{r\theta} = 0,$$

$$\sigma_{z\theta} = 0. \qquad (18)$$

The kinematic of the particles is reduced to three degrees of freedom (u_r, u_z, θ). The geometry of the particle A is defined by a thickness equal to the value of its coordinate r at the initial time r_A^0. The particle is defined by an angle portion of 1 radian. The volumetric strain of a particle can be separated into two terms. The first term corresponds to the volumetric strain in plane (r, z), which is used to define a volume change ε_{AB}^V of particle A with its neighbours B in plane (r, z) like in the previous part. The second term in u_r/r corresponds to the displacement of a particle A along the radial direction r.

The stress term $\sigma_{\theta\theta}$ introduces an additional force along axis r. This force is calculated assuming that particle A has two neighbouring particles in the orthoradial direction θ. Stress $\sigma_{\theta\theta}$ can be rewritten in the form below:

$$\sigma_{\theta\theta} = \frac{E(1-\vartheta)}{(1+\vartheta)(1-2\vartheta)}\frac{u_r}{r} + \frac{E\vartheta}{(1+\vartheta)(1-2\vartheta)}\left(\frac{\partial u_r}{\partial r} + \frac{\partial u_z}{\partial z}\right). \qquad (19)$$

The corresponding force $F_{\theta\theta}^A$ is orientated along the radial direction r of the plane, surface S_A corresponds to the surface of particle A in plane (r, z), the equilibrium distance with the two orthoradial virtual particles corresponds to the initial value r_A^0 of r for particle A, and the volumetric strain of particle A with its neighbours, ε_{AB}^V, is calculated in plane (r, z) only.

$$F_{\theta\theta}^A = \frac{E(1-\vartheta)S_A}{(1+\vartheta)(1-2\vartheta)}\frac{r_A^0 - r_A}{r_A^0} + \frac{E\vartheta S_A}{(1+\vartheta)(1-2\vartheta)}\,\varepsilon_{AB}^V. \qquad (20)$$

This formulation has already been verified for various value of the Poisson's ratio by Mariotti and Monasse (2012), but this formulation for the Girkmann problem was verified in this study.

4. Girkmann Problem

The Girkmann problem is a benchmark for an axisymmetric shell supported on a stiffening ring. The junction between the shell and the beam is a singularity which may output some deficiencies for a numerical method. This test was first described by Girkmann (1956) and later by Timoshenko and Woinowsky-Krieger (1959). A Benchmark was proposed in January 2008 by the International Association of Computation Mechanics (IACM).

This benchmark has been described in a paper from Szabo et al. (2010) and a paper from Devloo et al. (2013). A spherical shell of thickness h = 0.06 m and crown radius R_c = 15 m is connected to a stiffening ring at the meridional angle α = 40°. The middle radius of the spherical shell is $R_m = R_c/\sin\alpha$. The dimension of the section of the ring are horizontally a = 0.6 m and vertically b = 0.5 m (Fig. 2).

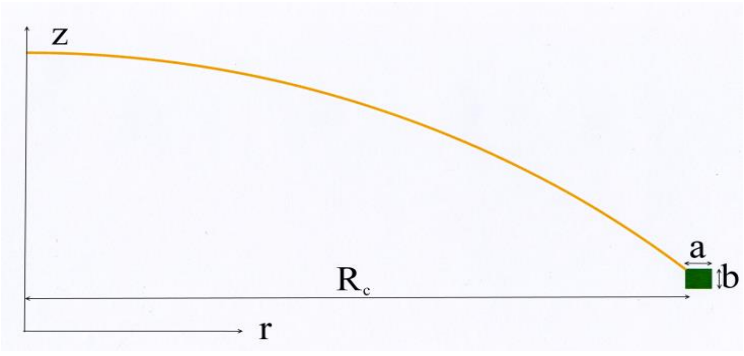

Fig. 2. Geometry of the Girkmann problem (Shell in yellow, Ring in green).

The shell is elastic with a Young modulus E = 20.59 10^9 Pa and a Poisson's ratio ϑ = 0. The density of the material is 3,269 kg/m^3. A gravity force of 10 m/s^2 is applied on the shell only and not on the ring. A uniform vertical pressure is acting on the base of the stiffening ring in order to equilibrate the gravity force. The values expected in this benchmark are the shearing force Q in N/m and the bending moment M in Nm/m acting at the junction between the spherical shell and the stiffening ring.

Classical continuous Finite Element Method may encounter difficulties at the singularity between the beam and the shell. For example, several results of axisymmetric Finite Element Method are presented in the paper of Szabo et al. (2010), the values of Q are varying between 940.9 N/m and 989.1 N/m and the values of M are varying between -36.62 and -89.11 Nm/m.

According to Devloo et al. (2013), the Discontinuous Galerkin method has been shown more accurate in

solving this type of singularity. So, the values of Q and M given by Devloo et al. (2013) for the high order DG formulation are taken as reference results for this benchmark (Table 1).

In this simulation with the Discrete Element Method, the shell and the ring are meshed with particles of about 0.005 m as shown in Fig. 3. The CeaMka3D simulation gives comparable results with the results of Devloo et al. (2013) (Table 1), the relative error is less than 0.35 %. So, the Discrete Element Method gives accurate results for this benchmark.

Table 1. Results for the Girkmann problem.

Numerical Method	Q (N/m)	M (Nm/m)
Pitkäranta Classical M-B-R model	942.5	-37.45
Devloo DG-FEM	943.65	-36.79
CeaMka3D DEM	946.4	-36.66

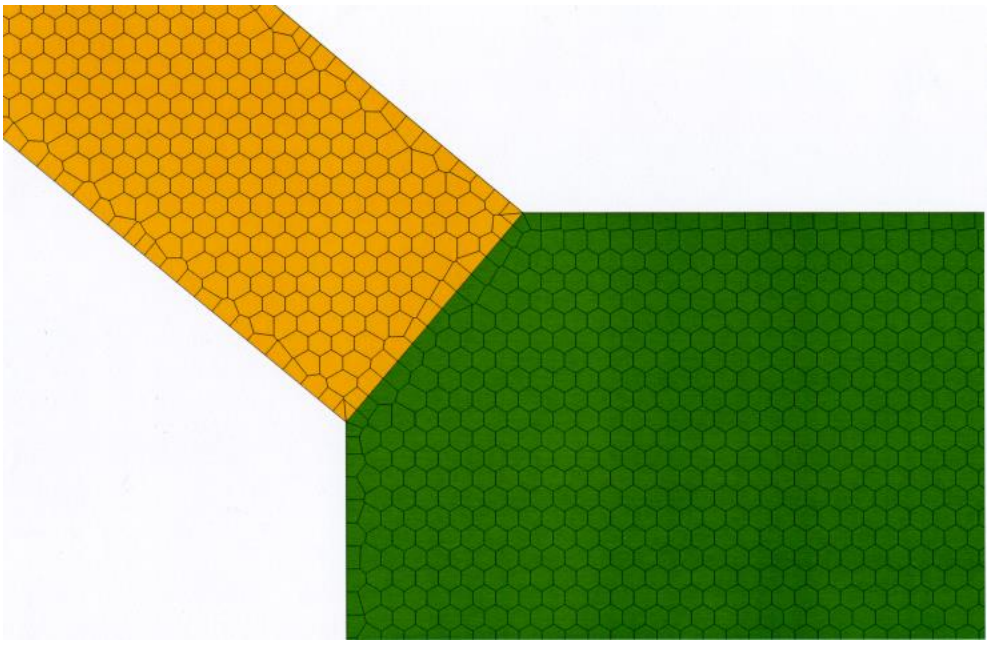

Fig. 3. Zoom of the mesh at the junction between the shell and the stiffening ring for CeaMka3D (Shell in yellow, Ring in green).

5. Conclusions

In the first part, the calculation of the volumetric deformation of a particle and the definition of forces and torques between particles has been described.

In the second part, an axisymmetric formulation for the Discrete Element code CeaMka3D has been presented. This formulation is applied to verify the robustness of the Discrete Element Method to the singularity of the Girkmann problem. This benchmark has been chosen because it may be quite difficult for classical continuous Finite Element Method.

The results given by the Discrete Element Method are closed to the reference results given by a High Order Discontinuous Galerkin Method. So this Discrete Element Method seems accurate for this kind of benchmark with a strong gradient. The axisymmetric formulation for this Discrete Element Method is also verified by this benchmark. It is an encouraging result for the development of this kind of method.

The Voronoï mesh has been chosen initially because this type of meshing does not leave geometrical space like that can be the case with spherical particles and the normal direction is linked directly to the positions of particles. In fact, the volume of contact of each particle is very important in order to define the volumetric strain.

But at present, one limitation of this Discrete Element formulation is the Voronoï mesh. In fact, a special treatment is necessary to create a Voronoï mesh along interfaces. It has been necessary to create a specific mesh generator in 2D and 3D in order to respect some geometrical interfaces with Voronoï mesh. In the future, it will be easier to use classical mesh generator with triangles particles in 2D or tetrahedrons particles in 3D. So, one direction for the development of this Discrete Element Method will be to define the forces and torques for two triangles or two tetrahedrons in contact.

References

Cundall PA, Strack ODL (1979). A discrete numerical model for granular assemblies. *Geotechnique*, 29(1), 47-65.

Devloo PRB, Farias AM, Gomes SM, Gonçalves JL (2013). Application of a combined continuous-discontinuous Galerkin finite element method for the solution of the Girkmann problem. *Computers and Mathematics with Applications*, 65, 1786-1794.

Girkmann K (1956). Flächentragwerke. 4th ed. Springer-Verlag, Wien.

Hoover WG, Arhurst WT, Olness RJ (1974). Two-dimensional studies of crystal stability and fluid viscosity. *Journal of Chemical Physics*, 60, 4043-4047.

Mariotti C (2007). Lamb's problem with the lattice model Mka3D. *Geophysical Journal International*, 171, 857-864.

Mariotti C (2015). A new Leapfrog scheme for rotational motion in 3D. *International Journal for Numerical Methods in Engineering*, 107, 273-289.

Mariotti C, Monasse L (2012). From General Mechanics to Discontinuity, Unified Approach to Elasticity. Presses des Ponts, France.

Mariotti C, Le Piver F, Aubry L (2015). A least-squares coupling method between a finite element code and a discrete element code. *International Journal for Numerical Methods in Engineering*, 101(10), 731-743.

Monasse L, Mariotti C (2012). An energy-preserving Discrete Element Method for elastodynamics. *ESAIM: Mathematical Modelling and Numerical Analysis*, 46(6), 1527-1553.

Pitkäranta J, Babuska I, Szabo B (2008). The Girkmann problem. *IACM Expression*, January 2008, 22-28.

Szabo B, Babuska I, Pitkäranta J, Nervi S (2010). The problem of verification with reference to the Girkmann problem. *Engineering with Computers*, 26, 171-183.

Timoshenko SP, Woinowsky-Krieger S (1959). Theory of Plates and Shells. McGraw-Hill, New York.

Challenge Journal of Structural Mechanics

Short Communication

Experimental verification of blade elongation and axial rotor shift in steam turbines

Pavel Procházka *

Institute of Thermomechanics, Academy of Sciences of the Czech Republic, 182 00 Prague, Czech Republic

ABSTRACT

The experimental research of static and dynamic characteristics of rotating parts of turbomachines is a very important part of the design and verification of the machine parameters as well as optimization of their operational regimes. The described method of measuring dynamic and static characteristics, especially blade elongation and rotor axial shift, are based on the utilization of the non-contact magnetoresistive sensors developed in the Institute of Thermomechanics AS CR. These sensors exhibit positive properties for this purpose.

ARTICLE INFO

Article history:
Received 9 August 2016
Accepted 16 September 2016

Keywords:
Blade elongation
Axial rotor shift
Steam turbines
Magnetoresistive sensors

1. Introduction

Long blades of steam turbines are exposed to extreme stress caused by centrifugal forces. Variable aerodynamic and many other excitation forces, e.g. bending and torsion vibrations of the shaft, cause vibration of the turbine blades especially in the low-pressure stages. Dynamic stress components are superimposed on the static stress component and may cause a fatigue failure of the blades with consequent large economic losses. Therefore, it seems most appropriate to investigate experimentally the status and behavior of the long turbine blades using non-contact diagnostic measurement systems (Procházka, and Vaněk, 2014). It was concluded in the study (Procházka, and Vaněk, 2012) that the most suitable electromagnetic sensors for the harsh environment of steam turbines are the magnetoresistive (MR) sensors. These sensors feature high sensitivity, directional sensitivity, low noise and wide frequency range from 0 to 300 kHz. Therefore, they can be used for static measurements and also statically calibrated (Procházka, and Vaněk, 2015).

2. Results of the Experimental Research

Blade elongation is an important stationary characteristic for the assessment of blade straining and efficiency of the turbine stage. The value of the clearance (distance between the blade tip and the stator) and subsequently blade elongation may be evaluated from the magnitude of the output signal of the MR sensor. It is necessary to measure the maximum or minimum voltage of the impulse generated by the blade passage, or to use the peak-to-peak value for the evaluation. The output voltage of the MR sensor depends on the distance between the blade and the active element of the sensor hyperbolically. The real value of the clearance has to be determined on the basis of a laboratory calibration. First it is necessary to determine the appropriate value of the axial displacement of the rotor. This value is then used for the correction of the constant by the calculation of the clearance. The axial displacement of the rotor can be estimated by measuring the signal amplitudes of the axial sensor at the blade root.

An example of real signals from the stator and axial non-contact MR sensor is shown in Fig. 1. These signals were recorded at the steam turbine 280 MW at the operational speed 3000 rpm. The upper signal is the signal of the stator sensor. The course of the function expressing the dependence on the axial position of the rotor must be determined experimentally. The advantage of the MR sensors is that they can be calibrated statically in laboratory using a micrometric traverser. Fig. 2 shows compressed signals of the stator and axial sensors. Individual

* *Corresponding author*. Tel.: +420-266-053171 ; Fax: +420-286-584695 ; E-mail address: proch@it.cas.cz (P. Procházka)
ISSN: 2149-8024 / DOI: http://dx.doi.org/10.20528/cjsmec.2016.09.021

sections correspond to different regimes of the turbine: 1-2 standby revolutions 40 rpm, 2-3 warming revolutions 400 rpm, 3-4 warming revolutions 1500 rpm with turbine startup, 4-A 3000 rpm, A-B connected to network, B-C disconnected from network, C power 22 MW connected to network, D 130 MW, E 170 MW. The measured axial displacement of the rotor when changing speed from 40 rpm to 3000 rpm was 4.75 mm. The blade elongation due to the centrifugal force by this speed change was 4.1 mm.

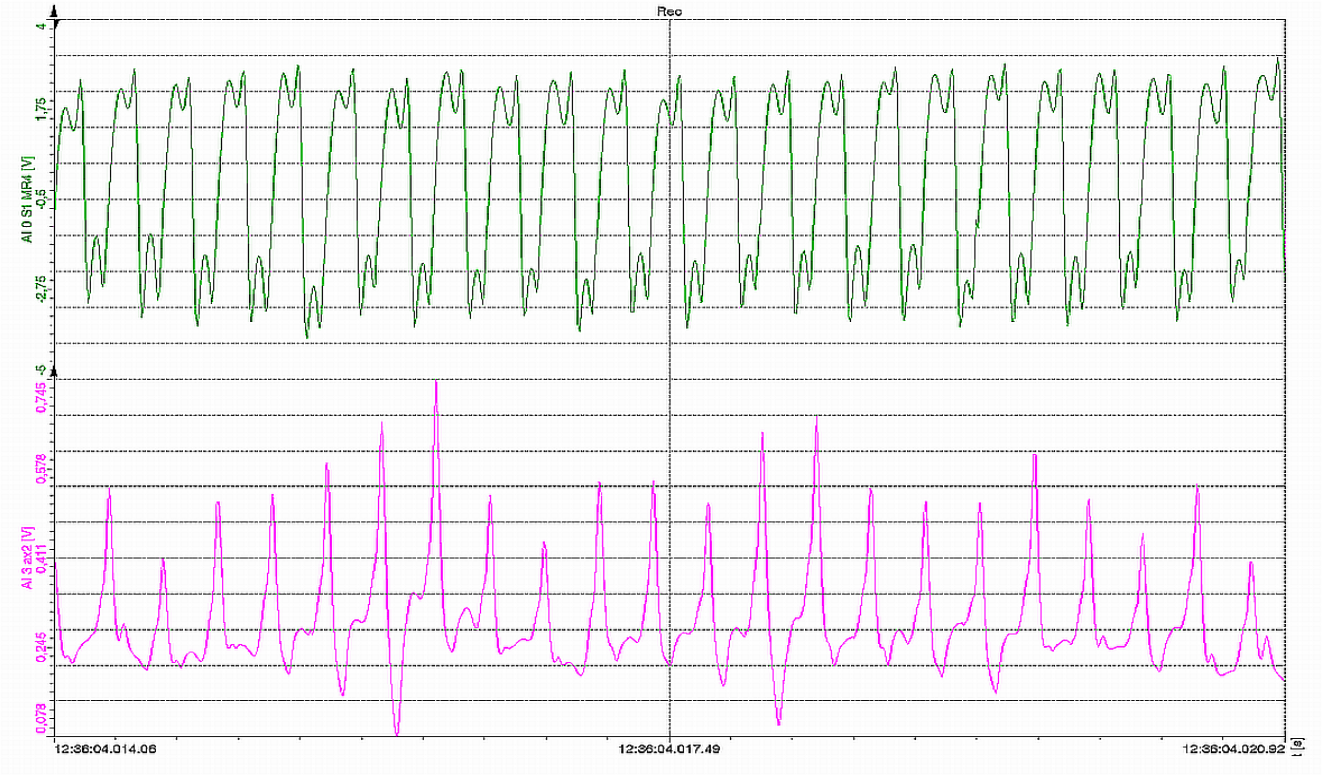

Fig. 1. Blade signals of the stator sensor (green) and the axial sensor (magenta).

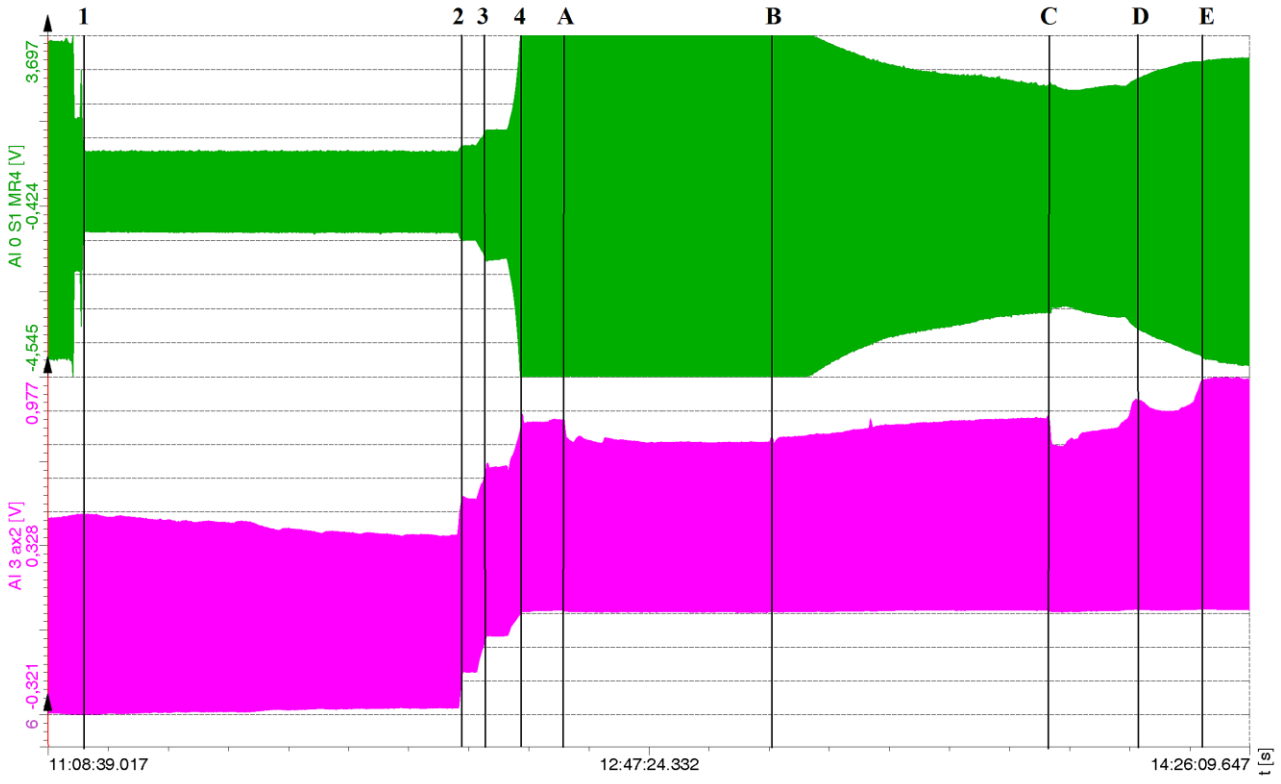

Fig. 2. Compressed signals of the stator sensor (green) and the axial sensor (magenta).

3. Conclusions

Magnetoresistive sensors proved to be a suitable mean for the experimental research of blade elongation and turbine rotor axial shift. These sensors feature high sensitivity and wide frequency range from DC values. This enables to calibrate them statically at lab using a positional traverser, which is a very important fact for improving accuracy and credibility of the measurements in harsh environment of the steam turbines.

Acknowledgements

The author would like to acknowledge the financial support of the Institute of Thermomechanics AS CR, v.v.i and the Project CZ.2. 16/3.1.00/21539 of the Operational Program EU Prague Competitiveness.

References

Procházka P, Vaněk F (2012). Non-contact methods of sensing vibrations of turbine blades. *10th International Conference on Vibrations in Rotating Machinery*, Woodhead Publishing, 221-231.

Procházka P, Vaněk F (2014). New methods of non-contact sensing of blade vibrations and deflections in turbomachinery. *IEEE Transactions on Instrumentation and Measurement,* 63(6), 1583-1592.

Procházka P, Vaněk F (2015). Non-contact measurement of stationary characteristics of shrouded steam turbine blades under rotation. *In: Proceedings of IEEE I2MTC*, Pisa, 2084-2088.

Challenge Journal of Structural Mechanics

Short Communication

Research of the non-uniform strain and displacement fields in solids with concentrators with the use of the DIC technique

Elena M. Spaskova *

Center of Experimental Mechanics, Perm National Research Polytechnic University, 614990 Perm, Russia

ABSTRACT

This work focuses on analyzes the non-uniform strain fields in the area of stress concentration and study the limiting stress-strain state of the material in the test samples with different geometry concentrators with the use of the measuring system non-contact three-dimensional digital optical system Vic-3D. The research included tensile mechanical tests on flat samples with a hole research of the damage and failure processes of materials.

ARTICLE INFO

Article history:
Received 19 August 2016
Accepted 21 September 2016

Keywords:
Digital image correlation
Limiting stress-strain state
Digital optical systems
Non-uniform strain fields

1. Introduction

In the field of solid mechanics one of the important tasks is to study the effect of different types of stress concentrators on the behavior of structural elements. The aim of the work is an experimental study of the stress-strain states in the hubs using the method of digital image correlation. In this work we consider the use of three-dimensional digital optical system, Vic-3D, the mathematical apparatus which is based on the method of digital image correlation (Schreier et al., 2009).

2. Results

The video system is designed for the analysis of displacement fields and strain on the sample surface. The technique of the experiment using a digital optical system, described its structure and working principle. The mathematical foundations of computing device system tested on uniaxial compression "Brazilian test" in order to develop the methodology of the experiment using a digital optical system.

The results of the uniaxial tensile tests on plates made of plexiglass with concentrators of different geometries are also presented the results of tests on a uniaxial tensile carbon plate with a circular hole using a digital optical system. Mechanical uniaxial tensile test were performed on the test system Instron 5882 and Instron 5989, together with the use of digital optical system Vic-3D. In Fig. 1, a result of the tensile test plates are constructed field transverse, longitudinal, shear deformations (ε_{xx}, ε_{yy}, ε_{xy}), as well as the intensity deformation (Tretyakova and Spaskova, 2013).

In some cases destruction of plates happened in two stages, at first on the one hand the concentrator that about 50% were accompanied by sharp recession of level of loading, at further loading there was an insignificant increase in value of loading and final fracture of a plate (Fig. 2).

For the analysis of the sample damage mechanisms, the strain intensity fields for different values of load (points *g*, *e*) are shown in (Fig. 3). The *g*-point corresponds to the ultimate strain-stress state of the specimen. This point clearly shows the place of defect localization.

* *Corresponding author*. E-mail address: cem.spaskova@mail.ru (E. M. Spaskova)
ISSN: 2149-8024 / DOI: http://dx.doi.org/10.20528/cjsmec.2016.09.023

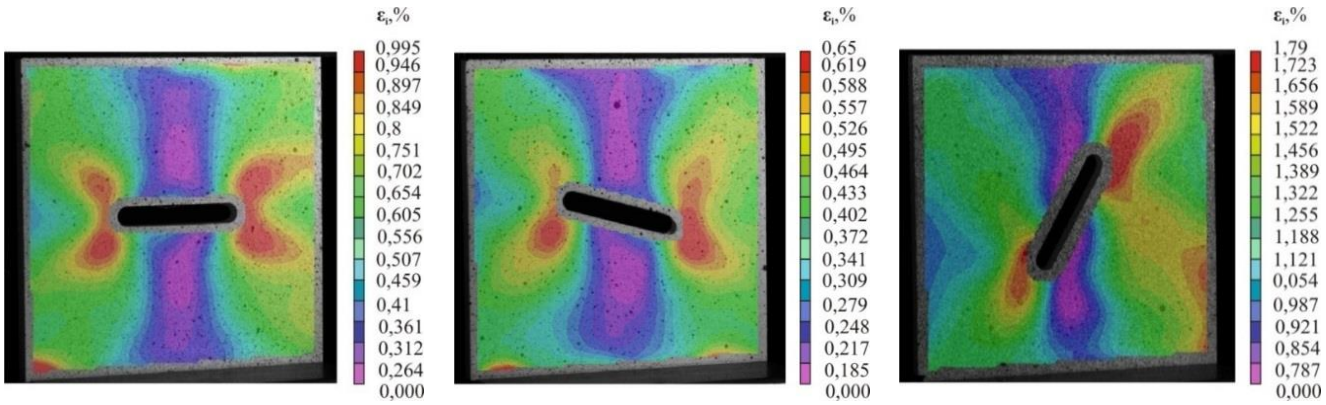

Fig. 1. Fields of strain intensity ε_i on a plate surface, an axis of cut with fields of plate.

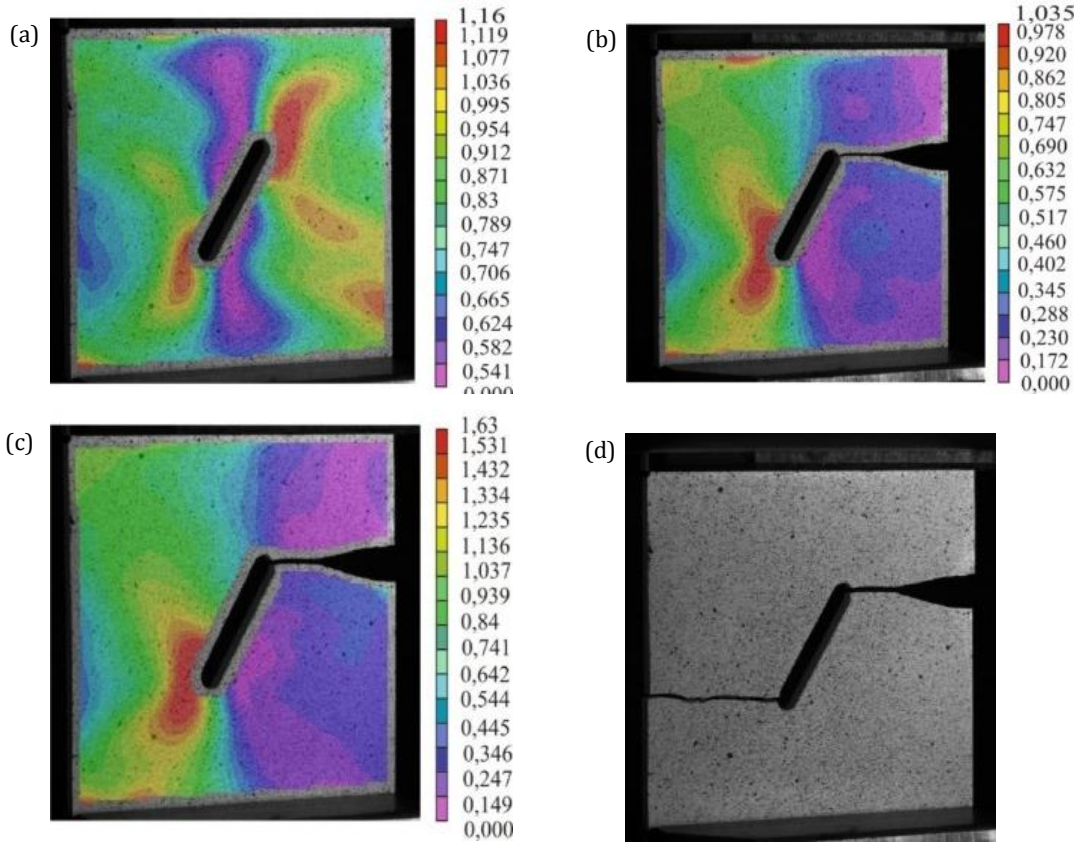

Fig. 2. Fields of strain intensity ε_i for a sample where the axis of cut made with the part of a plate is 60°, by load: (a) *P1*=2.837 kN; (b) *P2* = 1.243 kN; (c) *P3* = 1.713 kN; (d) photo of the destroyed sample.

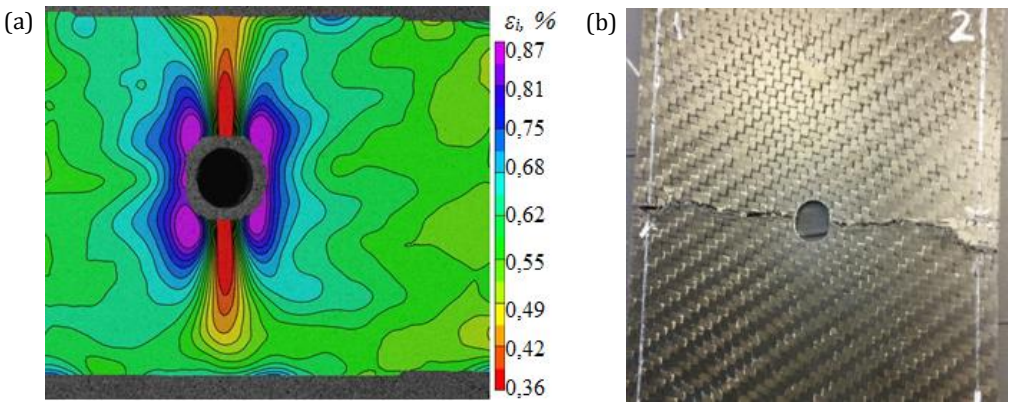

Fig. 3. Fields of strain intensity for different values of load: (a) isolines P_{max} = 104.74 kN; (b) broken specimen.

3. Conclusions

The system allowed to fix the evolution of the fields of displacements and strains to evaluate the nature of heterogeneity of fields to keep track of the material deformation processes occurring on the surface of the sample, and the add-on software video "virtual extensometer" was used in determining the mechanical properties of the material.

The high efficiency of the method of correlation of digital images to study the behavior of the material in the event of non-uniform strain fields (Tretyakova and Wildemann, 2014).

Acknowledgements

This study was carried out at the Perm National Polytechnic University with support of the Government of Russian Federation (Decree No. 220, April 9, 2010) under Contract No. 14. B25.310006, June 24, 2013.

References

Schreier H, Orteu JJ, Sutton MA (2009). Image Correlation for Shape, Motion and Deformation measurements. Basic Concepts, Theory and Applications, Springer.

Tretyakova TV, Spaskova EM (2013). Experimental study of limit stress-strain state quasi-brittle material using correlation techniques digital images. *PNRPU Mechanics Bulletin*, 2, 186-198.

Tretyakova TV, Wildemann VE (2014). Study of spatial-time inhomogeneity of serrated plastic flow Al-Mg alloy: using DIC technique. *Fracture and Structural Integrity*, 27, 83-97.